

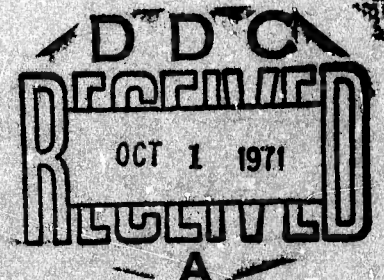
AD730449

SECOND SEMI-ANNUAL TECHNICAL REPORT

Contract DAHC15-70-C-0187

RESEARCH ON THE PROPERTIES OF AMORPHOUS SEMICONDUCTORS  
AT HIGH TEMPERATURES

Sponsored by:  
Advanced Research Projects Agency  
Program Manager  
Order No. 1570  
Program Code AD10

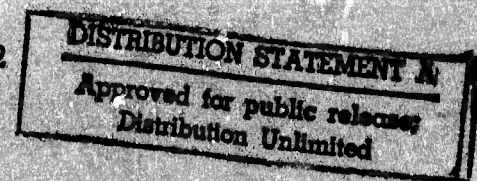


Prepared by:

Energy Conversion Devices, Inc.  
Dr. J. deNeufville  
Technical Manager  
313-549-7300

Contract period 18 May 1970 to 18 May 1972

Reproduced by  
NATIONAL TECHNICAL  
INFORMATION SERVICE  
Springfield, Va. 22151



COPY NO. 7

**BEST  
AVAILABLE COPY**

## Unclassified

## Security Classification

## DOCUMENT CONTROL DATA - R&amp;D

(Security classification of title, body of abstract and indexing annotation must be entered when the overall report is classified)

1. ORIGINATING ACTIVITY (Corporate author) Energy Conversion Devices, Inc. 1675 W. Maple Road, Troy, Michigan 48084		2a. REPORT SECURITY CLASSIFICATION Unclassified 2b. GROUP N/A
3. REPORT TITLE RESEARCH ON THE PROPERTIES OF AMORPHOUS SEMICONDUCTORS AT HIGH TEMPERATURES		
4. DESCRIPTIVE NOTES (Type of report and inclusive dates) Semi-Annual Technical Report - 18 November 1970 through 18 May 1971		
5. AUTHOR(S) (Last name, first name, initial) John P. deNeufville		
6. REPORT DATE 18 July 1971	7a. TOTAL NO. OF PAGES 178	7b. NO. OF REFS 29
8a. CONTRACT OR GRANT NO. DAHC15-70-C-0187 b. PROJECT NO. 1001/36 c. d.	9a. ORIGINATOR'S REPORT NUMBER(S) 516-2	
	9b. OTHER REPORT NO(S) (Any other numbers that may be assigned this report) None	
	10. AVAILABILITY/LIMITATION NOTICES The distribution of this report is unlimited	
	11. SUPPLEMENTARY NOTES	
12. SPONSORING MILITARY ACTIVITY Advanced Research Projects Agency Arlington, Virginia 22209		
13. ABSTRACT This report describes the work performed during the second six-month period of Contract DAHC15-70-C-0187. Emphasis on the compositional dependence of electrical and optical gaps and glass transition temperatures has been retained. In addition, detailed studies of thermoelectric power, switching behavior, thermal stability of thin films, crystallization kinetics, and electromigration have been initiated and extensive results of these studies are presented herein. These measurements have been obtained primarily on thin film samples produced by R.F. sputtering using an Argon plasma. The effects of thermal history in determining the physical properties of these thin amorphous films at 25°C and as a function of temperature have been studied extensively. In addition the liquid heat capacity results report previously for liquid Ge <sub>17</sub> Te <sub>83</sub> have been extended to include six other tellurium rich alloys including pure tellurium. Three contributed papers and one invited paper describing work performed under this contract were presented at the Fourth International Conference on Amorphous and Liquid Semiconductors in Ann Arbor Michigan on August 9-13, 1971.		

## Unclassified

## Security Classification

14. KEY WORDS	LINK A		LINK B		LINK C	
	ROLE	WT	ROLE	WT	ROLE	WT
Amorphous Semiconductors Amorphous Materials Chalcogenide Materials High temperature device materials						
INSTRUCTIONS						
1. ORIGINATING ACTIVITY: Enter the name and address of the contractor, subcontractor, grantee, Department of Defense activity or other organization (corporate author) issuing the report.	10. AVAILABILITY/LIMITATION NOTICES: Enter any limitations on further dissemination of the report, other than those imposed by security classification, using standard statements such as:					
2a. REPORT SECURITY CLASSIFICATION: Enter the overall security classification of the report. Indicate whether "Restricted Data" is included. Marking is to be in accordance with appropriate security regulations.	<ul style="list-style-type: none"> <li>(1) "Qualified requesters may obtain copies of this report from DDC."</li> <li>(2) "Foreign announcement and dissemination of this report by DDC is not authorized."</li> <li>(3) "U. S. Government agencies may obtain copies of this report directly from DDC. Other qualified DDC users shall request through _____."</li> <li>(4) "U. S. military agencies may obtain copies of this report directly from DDC. Other qualified users shall request through _____."</li> <li>(5) "All distribution of this report is controlled. Qualified DDC users shall request through _____."</li> </ul>					
2b. GROUP: Automatic downgrading is specified in DoD Directive 5200.10 and Armed Forces Industrial Manual. Enter the group number. Also, when applicable, show that optional markings have been used for Group 3 and Group 4 as authorized.						
3. REPORT TITLE: Enter the complete report title in all capital letters. Titles in all cases should be unclassified. If a meaningful title cannot be selected without classification, show title classification in all capitals in parenthesis immediately following the title.						
4. DESCRIPTIVE NOTES: If appropriate, enter the type of report, e.g., interim, progress, summary, annual, or final. Give the inclusive dates when a specific reporting period is covered.						
5. AUTHOR(S): Enter the name(s) of author(s) as shown on or in the report. Enter last name, first name, middle initial. If military, show rank and branch of service. The name of the principal author is an absolute minimum requirement.						
6. REPORT DATE: Enter the date of the report as day, month, year; or month, year. If more than one date appears on the report, use date of publication.						
7a. TOTAL NUMBER OF PAGES: The total page count should follow normal pagination procedures, i.e., enter the number of pages containing information.						
7b. NUMBER OF REFERENCES: Enter the total number of references cited in the report.						
8a. CONTRACT OR GRANT NUMBER: If appropriate, enter the applicable number of the contract or grant under which the report was written.						
8b, 8c, & 8d. PROJECT NUMBER: Enter the appropriate military department identification, such as project number, subproject number, system numbers, task number, etc.						
9a. ORIGINATOR'S REPORT NUMBER(S): Enter the official report number by which the document will be identified and controlled by the originating activity. This number must be unique to this report.						
9b. OTHER REPORT NUMBER(S): If the report has been assigned any other report numbers (either by the originator or by the sponsor), also enter this number(s).						
If the report has been furnished to the Office of Technical Services, Department of Commerce, for sale to the public, indicate this fact and enter the price, if known.						
11. SUPPLEMENTARY NOTES: Use for additional explanatory notes.						
12. SPONSORING MILITARY ACTIVITY: Enter the name of the departmental project office or laboratory sponsoring (paying for) the research and development. Include address.						
13. ABSTRACT: Enter an abstract giving a brief and factual summary of the document indicative of the report, even though it may also appear elsewhere in the body of the technical report. If additional space is required, a continuation sheet shall be attached.						
It is highly desirable that the abstract of classified reports be unclassified. Each paragraph of the abstract shall end with an indication of the military security classification of the information in the paragraph, represented as (TS), (S), (C), or (U).						
There is no limitation on the length of the abstract. However, the suggested length is from 150 to 225 words.						
14. KEY WORDS: Key words are technically meaningful terms or short phrases that characterize a report and may be used as index entries for cataloging the report. Key words must be selected so that no security classification is required. Identifiers, such as equipment model designation, trade name, military project code name, geographic location, may be used as key words but will be followed by an indication of technical context. The assignment of links, rules, and weights is optional.						

**SECOND SEMI-ANNUAL TECHNICAL REPORT**

**Contract DAHC15-70-C-0187**

**RESEARCH ON THE PROPERTIES OF AMORPHOUS SEMICONDUCTORS  
AT HIGH TEMPERATURES**

**Sponsored by:  
Advanced Research Projects Agency  
Program Manager  
Order No. 1570  
Program Code 0D10**

**Prepared by:**

**Energy Conversion Devices, Inc.  
Dr. J. deNeufville  
Technical Manager  
313-549-7300**

**Contract period 18 May 1970 to 18 May 1972**

## SUMMARY OF MAJOR ACCOMPLISHMENTS

The survey of the whole spectrum of chalcogenide glasses for a broad array of possible applications at high temperatures requires an understanding of those fundamental properties which determine the range of attainable behavior. In this regard we continue to consider glass transition temperatures and the electrical and optical "band gaps" as most indicative of thermal stability and transport properties, and have emphasized these properties in our survey work.

We have found that for a multi-valent ternary glass-forming system (Si-Te-As) the  $T_g$  maxima lie nearly along the line connecting SiTe to As, i.e. along the line of average coordination number 3. We conclude that network stability varies as a function of the degree of connectedness, and that an average connectedness of 3 per atom produces the strongest network. In addition, among the glasses which meet this coordination requirement, those which contain mostly bonds between unlike atoms have the highest  $T_g$ 's.

Our attention has been increasingly focused on the properties of thin amorphous films because many of the potential applications of these materials lie in the realm of thin film technology. Many new problems are encountered in the study of films which are neither noticeable nor important in the study of bulk materials. Most significant of these "thin film effects" are the property changes induced by annealing films above their deposition temperature and below their glass transition temperature. These changes generally

do not relate to crystallization effects but rather appear to be characteristic of defects in the freshly deposited films (broken bonds, strain). In general, these annealing effects lead to higher resistivity films with lower optical absorption. The annealing studies yielded the following results.

1. Annealing effects observed for the optical and electrical properties appear to become fully saturated below the glass transition temperature  $T_g$ .
2. The annealing process is a bulk effect in that the kinetics are not affected by sample thickness.
3. The magnitude of the observed property changes produced by annealing appears to scale with the difference between the deposition temperature and  $T_g$ , i.e. the effects are especially pronounced in films of high  $T_g$ .
4. The thermoelectric power is more sensitive to annealing and perhaps to impurities than is the conductivity.

In addition to these annealing effects below  $T_g$ , we have been concerned with stability of films above  $T_g$  in the range of temperatures where crystallization, phase separation and selective volatilization become important. These effects have been studied via transmission electron microscopy, X-ray diffraction, and mass spectrometry. These techniques have also proved useful for characterizing in greater detail the crystallization and thermal decomposition behavior of the films in the Te-GeTe eutectic family of memory switching compositions. While these compositions have

relatively low glass transition temperatures, (~ 120-150° C), they constitute a rather remarkable class of materials in terms of their reversible crystallization and vitrification kinetics and reproducibility, properties which have not been encountered in our systematic surveys of new high temperature chalcogenide glasses. Therefore, there is an even greater necessity to characterize these materials in complete detail to guide the search for higher temperature analogues. The major results are the following:

1. The crystallization of Te dominates the thermal crystallization of the memory glass  $Ge_{15}Te_{81}Sb_2S_2$ . (In fact, from what we can determine, Te crystallization is the dominant factor in the memory setting of the majority of thin film Te based chalcogenides). The influence of impurities is yet to be discussed, but it seems apparent that they must be important in determining the rate and scale of Te crystallization and the ease of GeTe formation.
2. The particle size of the Te increases monotonically with annealing temperature but is not so sensitive a function of time at any temperature. At 275° C, the Te crystallite size has reached the limiting observable value of  $\geq 1,000 \text{ \AA}$ .
3. The Te appears to come out with a slight to strong (00.1) or C-axis texture normal to the film. In other words, the C axis tends to grow and/or nucleate more easily normal to the plane of the film. This tendency increases with increasing temperature

and then falls off as the ease and rate of crystallization enhances the tendency toward randomness.

4. The eutectic Ge-Te glass (with or without Sb, S) does not homogeneously phase separate prior to crystallization. The very earliest detectable crystallization above  $T_g$  is invariably heterogeneous.
5. These glasses tend to yield a very large volume fraction of crystalline Te (and no GeTe) when annealed for a long time just above  $T_g$ .
6. The  $Ge_{15}Te_{81}Sb_2S_2$  seems to show a lower volume fraction Te at  $275^\circ C$  than at  $140^\circ C$ . At  $275^\circ C$ , a very rough estimate yields 50% Te. This indicates an increased tendency to develop more Te at lower temperatures.

We have continued to focus considerable attention on electrical transport measurements, including probe switching studies of thin films at high fields, thermoelectric power measurements, and photoconductivity. The switching measurements have revealed broad regularities among classes of materials which should lead to improved threshold switching materials with high thermal stability. In addition, new switching measurements at elevated temperatures are here reported which indicate that improved threshold stability can generally be expected in a high temperature operating mode. In particular, a memory switching composition has been found to switch consistently and reliably for long periods of time in the vicinity of its glass transition temperature.

The thermoelectric power of amorphous semiconductor materials is of fundamental physical interest as well as being potentially useful, so we have undertaken an extensive survey of this property, primarily in thin film configurations. This survey has initially catalogued the effects of compositional variation as well as the subtle effects of thermal history. While the thermoelectric power figure of merit for these materials is relatively low below their glass transition temperature, we have been able to extend these measurements well above  $T_g$  for some materials, depending upon their ability to withstand crystallization under these conditions.

At higher temperatures, most chalcogenide glasses with reasonably high electrical conductivities ( $> 10^{-8} \Omega^{-1} \text{cm}^{-1}$  at  $25^\circ \text{C}$ ) tend to become essentially metallic liquids in terms of their electrical conductivity and viscosity. The transition from semiconducting to metallic behavior in the liquid state is of great interest especially in view of the discovery of a large excess heat capacity for  $\text{Te}_{83}\text{Ge}_{17}$  liquid in this temperature range reported in the first Semi-Annual Technical Report for this contract.

We have found such a large anomalous heat capacity maximum near  $420^\circ \text{C}$  in several chalcogenide glasses containing Ge. We tentatively relate its occurrence to an order-disorder transition of the following kind. In  $\text{GeTe}_2$ , for example, the glassy structure contains essentially only Ge-Te covalent bonds. The bond ordering disappears upon heating and the mixed bond structure is favored in the liquid because of its higher entropy. The disordering process yields the excess enthalpy which gives rise to the

maximum in heat capacity. The maximum is found to scale with the Ge-Te bond concentration. A bond fraction model is developed which is expected to yield further insight into the structure of chalcogenide glasses. We have examined the properties of liquids in this range via continued heat capacity measurements. The latter property is of crucial interest in analyzing the behavior of any amorphous chalcogenide device operated at a high electric field in this temperature range.

## TABLE OF CONTENTS

	Page
<b>SUMMARY OF MAJOR ACCOMPLISHMENTS</b>	<b>1</b>
<b>1. INTRODUCTION</b>	<b>1</b>
<b>2. SURVEY OF GLASS TRANSITION TEMPERATURE FOR HIGH TEMPERATURE CHALCOGENIDE ALLOYS</b>	<b>3</b>
<b>2.1 Introduction</b>	<b>3</b>
<b>2.2 Experimental Results and Discussion</b>	<b>3</b>
<b>3. SURVEY OF ELECTRICAL AND OPTICAL PROPERTIES OF SPUTTERED AMORPHOUS SEMICONDUCTOR FILMS: EFFECTS OF ANNEALING</b>	<b>17</b>
<b>4. TRANSPORT MEASUREMENTS</b>	<b>30</b>
<b>4.1 Thermoelectric Measurements</b>	<b>30</b>
<b>4.1.1 Introduction</b>	<b>30</b>
<b>4.1.2 Experimental Procedure</b>	<b>32</b>
<b>4.1.3 Results</b>	<b>34</b>
<b>4.1.4 Structure</b>	<b>47</b>
<b>4.1.5 Theory of Thermoelectric Effects in Amorphous Semiconductors</b>	<b>49</b>
<b>4.1.6 Discussion of Thermopower Results</b>	<b>52</b>
<b>4.1.7 Thermoconductivity</b>	<b>58</b>
<b>4.1.8 Thermoelectric Figure of Merit</b>	<b>58</b>
<b>4.1.9 Further Experimentation</b>	<b>62</b>
<b>4.2 Photoconductivity</b>	<b>63</b>
<b>4.3 Switching Measurements</b>	<b>68</b>
<b>4.3.1 Introduction</b>	<b>68</b>
<b>4.3.2 Experimental Methods</b>	<b>68</b>

**Table of Contents (Cont'd.)**

<b>4.3.3</b>	<b>Results</b>	<b>73</b>
<b>4.3.3.1</b>	<b>Switching at 298° K</b>	<b>73</b>
<b>4.3.3.2</b>	<b>Switching Characteristics at Elevated Temperatures</b>	<b>86</b>
<b>4.3.4</b>	<b>Discussion of Switching Materials Survey</b>	<b>86</b>
<b>5.</b>	<b>EFFECTS OF SUBSTRATE TEMPERATURE ON THE PROPERTIES OF RF SPUTTERED OMS MATERIAL</b>	<b>92</b>
<b>5.1</b>	<b>Detailed Description of Each Experiment</b>	<b>95</b>
<b>5.2</b>	<b>Summary of Experimental Results</b>	<b>99</b>
<b>6.</b>	<b>THERMAL CRYSTALLIZATION OF SELECTED Te-BASED CHALCOGENIDES</b>	<b>109</b>
<b>6.1</b>	<b>Thermodynamics and Metastability in the Partial System Te-GeTe</b>	<b>110</b>
<b>6.2</b>	<b>X-Ray Diffraction</b>	<b>115</b>
<b>6.2.1</b>	<b>Experiment</b>	<b>115</b>
<b>6.2.2</b>	<b>Results</b>	<b>117</b>
<b>6.2.3</b>	<b>Conclusions</b>	<b>122</b>
<b>6.3</b>	<b>Transmission Electron Microscopy</b>	<b>123</b>
<b>6.3.1</b>	<b>Experiment</b>	<b>123</b>
<b>6.3.2</b>	<b>Results and Discussion</b>	<b>125</b>
<b>6.3.3</b>	<b>Electron-Beam <math>\mu</math>-probe Results</b>	<b>138</b>
<b>6.3.4</b>	<b>Summary and Conclusions</b>	<b>140</b>
<b>7.</b>	<b>PROPERTIES OF CHALCOGENIDE LIQUIDS</b>	<b>144</b>
<b>7.1</b>	<b>Liquid Conductivity and Heat Capacity</b>	<b>144</b>
<b>7.2</b>	<b>Electromigration in Liquid <math>Te_{85}Ge_{15}</math> at 550° C</b>	<b>154</b>

**Table of Contents (Cont'd.)**

<b>7.2.1</b>	<b>Introduction</b>	<b>154</b>
<b>7.2.2</b>	<b>Determination of Atomic Density and Composition</b>	<b>155</b>
<b>7.2.3</b>	<b>Electromigration - Experimental Considerations</b>	<b>159</b>
<b>7.2.4</b>	<b>Experimental Results</b>	<b>164</b>
<b>7.2.5</b>	<b>Discussion</b>	<b>173</b>
<b>8.</b>	<b>REFERENCES</b>	<b>176</b>
<b>9.</b>	<b>CONTRIBUTORS TO THIS PROGRAM</b>	<b>178</b>

## I. INTRODUCTION

This report describes the work performed during the second six-month period of Contract DAHC15-70-C-0187. Emphasis on the compositional dependence of electrical and optical gaps and glass transition temperatures has been retained. In addition, detailed studies of thermoelectric power, switching behavior, thermal stability of thin films, crystallization kinetics, and electromigration have been initiated and extensive results of these studies are presented herein. These measurements have been obtained primarily on thin film samples produced by R.F. sputtering using an Argon plasma. The effects of thermal history in determining the physical properties of these thin amorphous films at 25° C and as a function of temperature have been studied extensively. In addition the liquid heat capacity results reported previously for liquid  $Ge_{17}Te_{83}$  have been extended to include six other tellurium rich alloys including pure tellurium. Three contributed papers and one invited paper describing work performed under this contract were presented at the Fourth International Conference on Amorphous and Liquid Semiconductors in Ann Arbor, Michigan on August 9-13, 1971.

These studies are continuing, with current emphasis being placed on the detailed examination of a few prototypical materials selected on the basis of their structural simplicity and their stability at elevated temperatures. In addition, we will continue to search for new families of high temperature chalcogenide materials and to characterize the thermal, electrical and optical properties of these materials as they are synthesized.

The present report is organized like its predecessor in that each class of measurement is presented in a separate chapter. Chapter 2 presents the continuing survey work and comments further on classes of chalcogenide glasses which appear to be suitable for high temperature applications. Chapter 3 presents a continuation of the electrical and optical survey work reported earlier, with a current emphasis on the effects of thermal history upon the electrical conductivity and optical absorption. Chapter 4 reviews our progress on transport measurements, thermoelectric power, photoconductivity, and high field (switching) measurements. Chapter 5 is a detailed property study of a single OMS material,  $\text{Te}_{81}\text{Ge}_{15}\text{Sb}_2\text{S}_2$  deposited by R.F. sputtering at a variety of substrate temperatures. This study contains in addition to electrical and optical characterization data, a detailed study of the thermal decomposition of the sputtered films in a mass spectrometer. Chapter 6 emphasizes our structural studies of  $\text{Te}_{85}\text{Ge}_{15}$  based OMS materials, involving extensive X-ray diffraction and transmission electron microscopic examination of thermally annealed and partially crystallized thin films. Chapter 7 describes the liquid state property measurements in the vicinity of the gradual semiconductor-metal transformation observed for the Te based liquids in the vicinity of  $350 - 550^{\circ}\text{C}$ . Measurements of electrical conductivity, heat capacity and electromigration are presented.

## 2. SURVEY OF GLASS TRANSITION TEMPERATURE FOR HIGH TEMPERATURE CHALCOGENIDE ALLOYS

### 2.1 Introduction

The survey of thermal stability of chalcogenide glasses reported in the first semiannual technical report of this contract pointed to several compositions with critical chalcogen saturation (i.e. with the minimum concentration of cross linking additive to completely cross link all chalcogen atoms) which display high thermal stability. These relatively high glass transition critical chalcogen saturated compositions include  $\text{GeTe}_2$ ,  $\text{GeSe}_2$ ,  $\text{SiTe}_2$ ,  $\text{Ga}_2\text{Te}_3$  and  $\text{In}_2\text{Te}_3$ . Consistent with our overall goal of evaluating the properties of thermally stable chalcogenide glasses we have selected the  $\text{GeSe}_2$  -  $\text{GeTe}_2$  system for detailed study. In this chapter, the composition dependence of the glass transition temperature and the density are presented, and in Chapter 3 we present results of optical absorption and electrical conductivity experiments. In addition, we have extended our survey of the  $\text{As}_2\text{Te}_3$  -  $\text{GeSe}_2$  pseudobinary system towards higher  $\text{GeSe}_2$  compositions. Our studies of glass formation in the  $\text{SiTeAs}$  ternary system which yielded glasses with extreme thermal stability ( $T_g > 430^\circ \text{C}$ ) have been extended to better delineate the  $T_g$  isotherms in the vicinity of the  $T_g$  maximum.

### 2.2 Experimental Results and Discussion

The compositional dependence of the glass transition temperature and the density are plotted as a function of composition for the  $\text{GeTe}_2$  -  $\text{GeSe}_2$  pseudobinary system in Figure 2.1. This is a chemically and structurally simple system in the sense that

**Fig. 2.1**

**Composition Dependence of Glass Transition Temperature and Density  
for Glasses in the  $\text{GeTe}_2$  -  $\text{GeSe}_2$   
System**

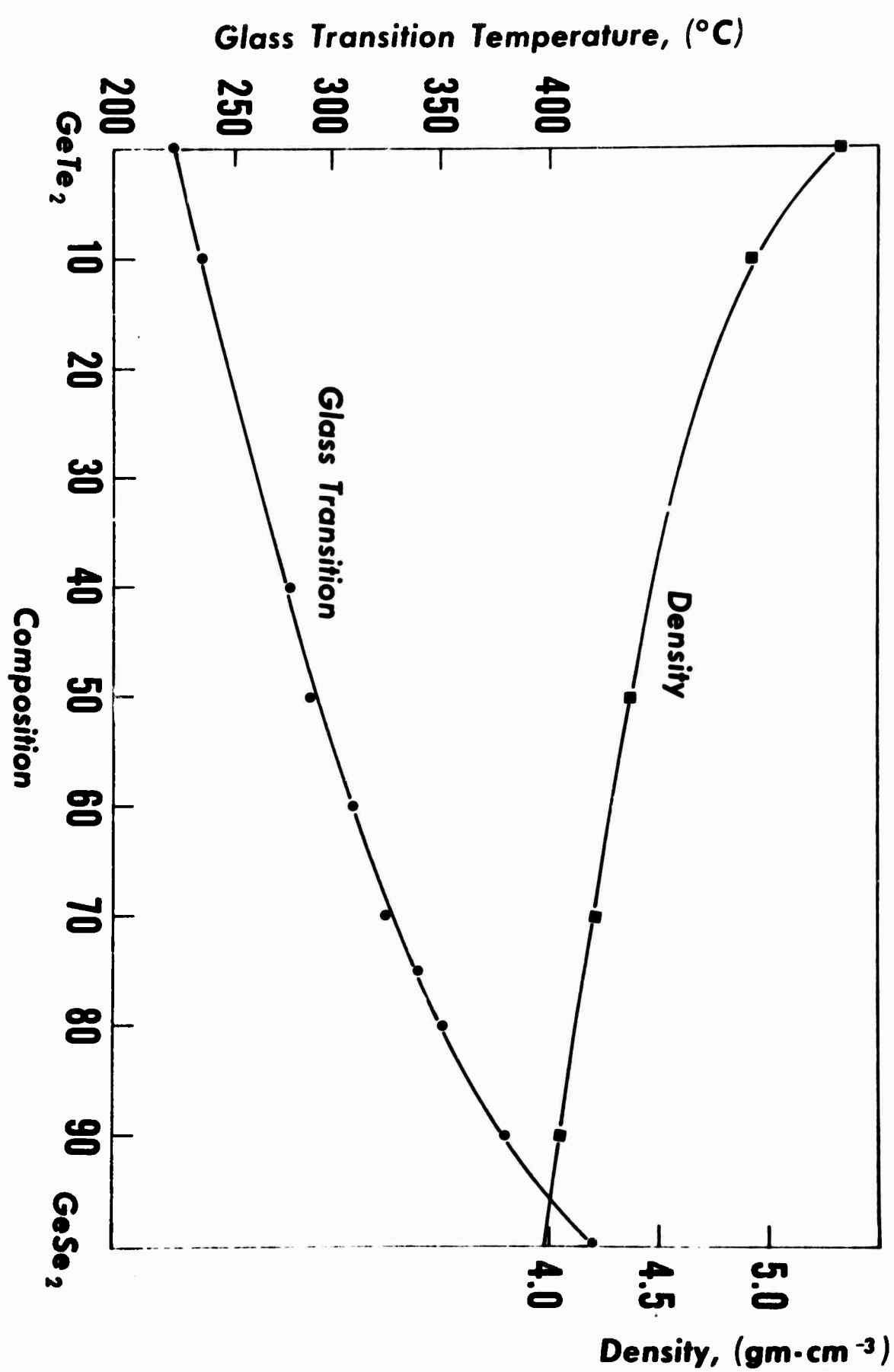


Fig. 2.1

both end members presumably share the fully cross-linked random network structure observed for  $\text{SiO}_2$ ,<sup>1</sup>  $\text{GeO}_2$ <sup>2</sup> and similar glasses. In addition, the smooth monotonic increase of  $T_g$  with the addition of  $\text{GeSe}_2$  provides convincing evidence that these glasses do not phase separate. Therefore the structures of the pseudobinary glasses can be considered as composed of  $\text{Ge}(\text{Se}, \text{Te})_4$  tetrahedra connected together by the shared chalcogen atoms of their vertices. Clearly the Ge-Te bond is weaker than the Ge-Se bond as predicted chemically and as indicated (Figure 3.3, page 24, this report) by the variation of electrical and optical gap in this system. It is therefore of interest to observe the nonlinearity of  $T_g$  with composition in the vicinity of pure  $\text{GeSe}_2$ ; the addition of a few Ge-Te bonds sharply lowers the glass transition temperature. An analogous lowering of the glass transition temperature of  $\text{SiO}_2$  occurs in the  $\text{SiO}_2$  -  $\text{GeO}_2$  system<sup>3</sup> and the observed nonlinear dependence of  $T_g$  upon composition can be simply related to the weakening of the  $\text{SiO}_2$  glassy network by the addition of a small concentration of weaker Ge-O bonds.

Also plotted in Figure 2.1 is the compositional dependence of density in this pseudobinary system. Note that all the  $\rho$  points and the  $T_g$  points obtained on the pure  $\text{GeTe}_2$  and  $\text{GeTe}_{1.8}\text{Se}_{0.2}$  compositions were measured on thick sputtered films. The densities of several of these compositions have also been measured on bulk samples ( $\text{GeTeSe}$ ,  $\text{GeTe}_{0.4}\text{Se}_{1.6}$ ), yielding values about 8% higher than on the unannealed sputtered films. This density deficit in the sputtered films agrees closely

with our results reported<sup>15</sup> for the  $\text{As}_2\text{Te}_3$  -  $\text{GeSe}_2$  system. We did not observe any annealing effects in measuring the  $T_g$  of these sputtered films. Presumably the annealing effects observed for the optical and electrical properties of these films reported in Chapter 3 have become fully saturated below  $T_g$ . The  $T_g$  data from both film and bulk samples appear to be well fitted by a single curve. We have confirmed the validity of the bulk vs. sputtered glass comparison by  $T_g$  measurements on compositions which can be prepared using either technique and are reasonably confident that the method is generally valid, i.e., that  $T_g$  of the sputtered films closely approximate the bulk glass value. Clearly, however, this method will be invalid when the bulk glass is phase separated, since the sputtering process would force such a composition to come down as a homogeneous glass, so that an independent confirmation of homogeneity of the sputtered glass after heating above  $T_g$  is required. For example, if no exotherm or shift in  $T_g$  accompanies annealment just above  $T_g$  then it may be reasonably assumed that the composition in question has little tendency to phase separate.

In order to verify the mixed network model for the pseudobinary  $\text{GeTe}_2$  -  $\text{GeSe}_2$  join in the ternary Ge-Te-Se system, we have taken a pseudobinary slice at right angles to this join, i.e., we have measured the compositional dependence of  $T_g$  in a portion of the pseudobinary system Ge-SeTe. These data are plotted in Fig. 2.2

**Fig. 2.2**

**Composition Dependence of Glass Transition Temperature in a  
Portion of the Ge-SeTe System.**

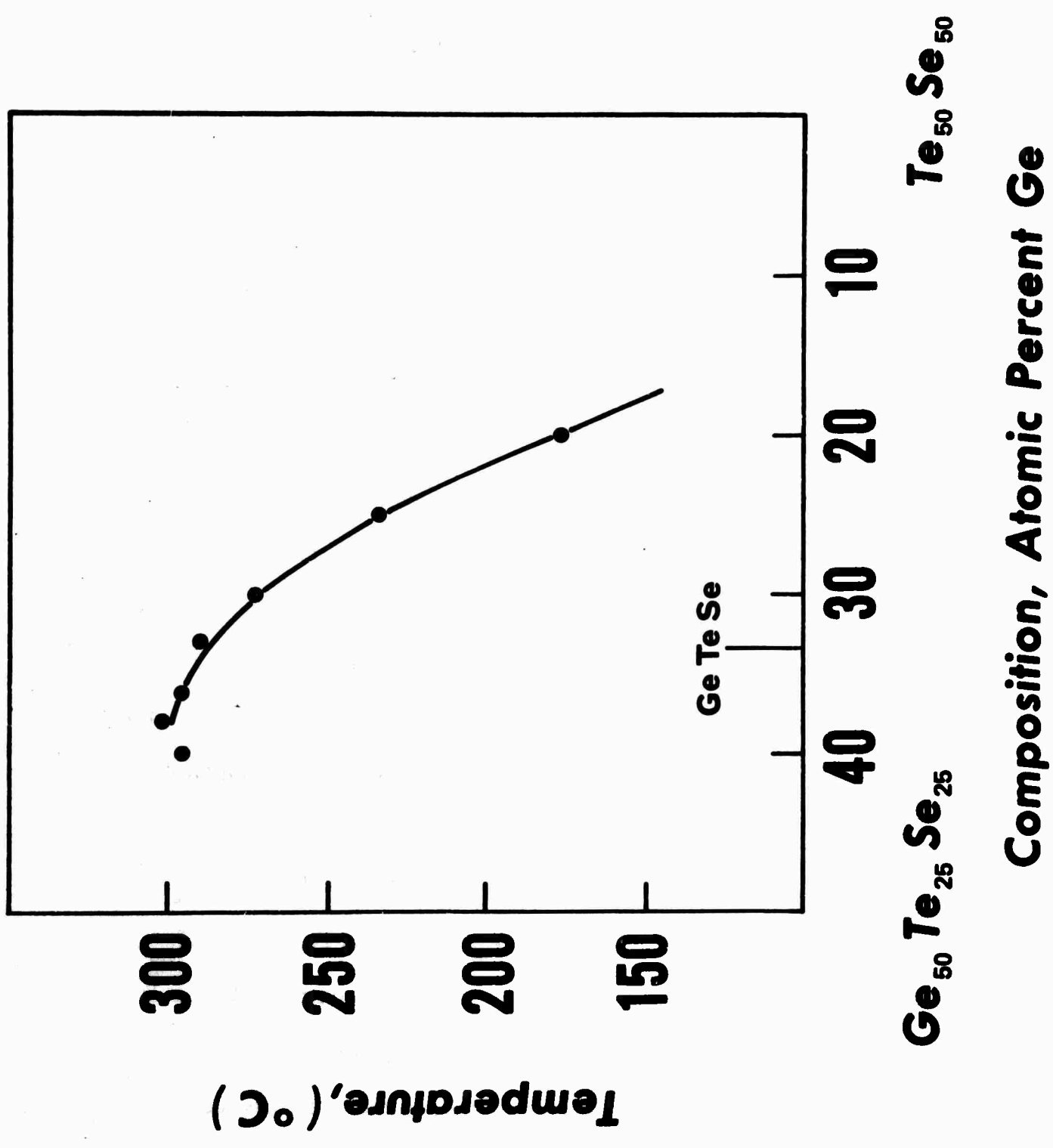


Fig. 2.2

and indicate a steep increase in  $T_g$  up to the GeTeSe cross-linked composition, rising toward a broad plateau with the addition of further Ge. In the steeply varying regime between TeSe and GeTeSe, the addition of Ge increases the degree of cross-linking and thereby drastically raises the glass transition temperature. In this excess chalcogen regime, some of the free volume produced at the glass transition temperature is obtained by breaking weak interchain van der Waals bonds rather than strong intrachain covalent bonds. On the other hand, adding Ge to GeTeSe retains the interconnected cross-linked network structure, and at the same time increases the average coordination above the 2.67 value at GeTeSe. At present we interpret the observed tendency toward a  $T_g$  plateau in this range (in contrast to the sharp maximum observed in  $T_g$  for the Ge-Te system at the composition  $\text{GeTe}_2$ ) in terms of increased covalency of the ternary glasses relative to the binary glasses between  $\text{GeTe}_2$  and GeTe.

The compositional dependence of  $T_g$  in the  $\text{As}_2\text{Te}_3 - \text{GeSe}_2$  pseudobinary system, part of which was plotted in Figure 2.3 of the previous semiannual technical report of this contract, is shown in its entirety in Figure 2.3. Note that the curvature observed in Figure 2.1 is here enhanced due, perhaps, to the even greater disparity of  $T_g$  between the two end members. All of these glasses

Fig. 2.3

**Composition Dependence of Glass Transition Temperature  
in the  $\text{GeSe}_2 - \text{As}_2\text{Te}_3$  System**

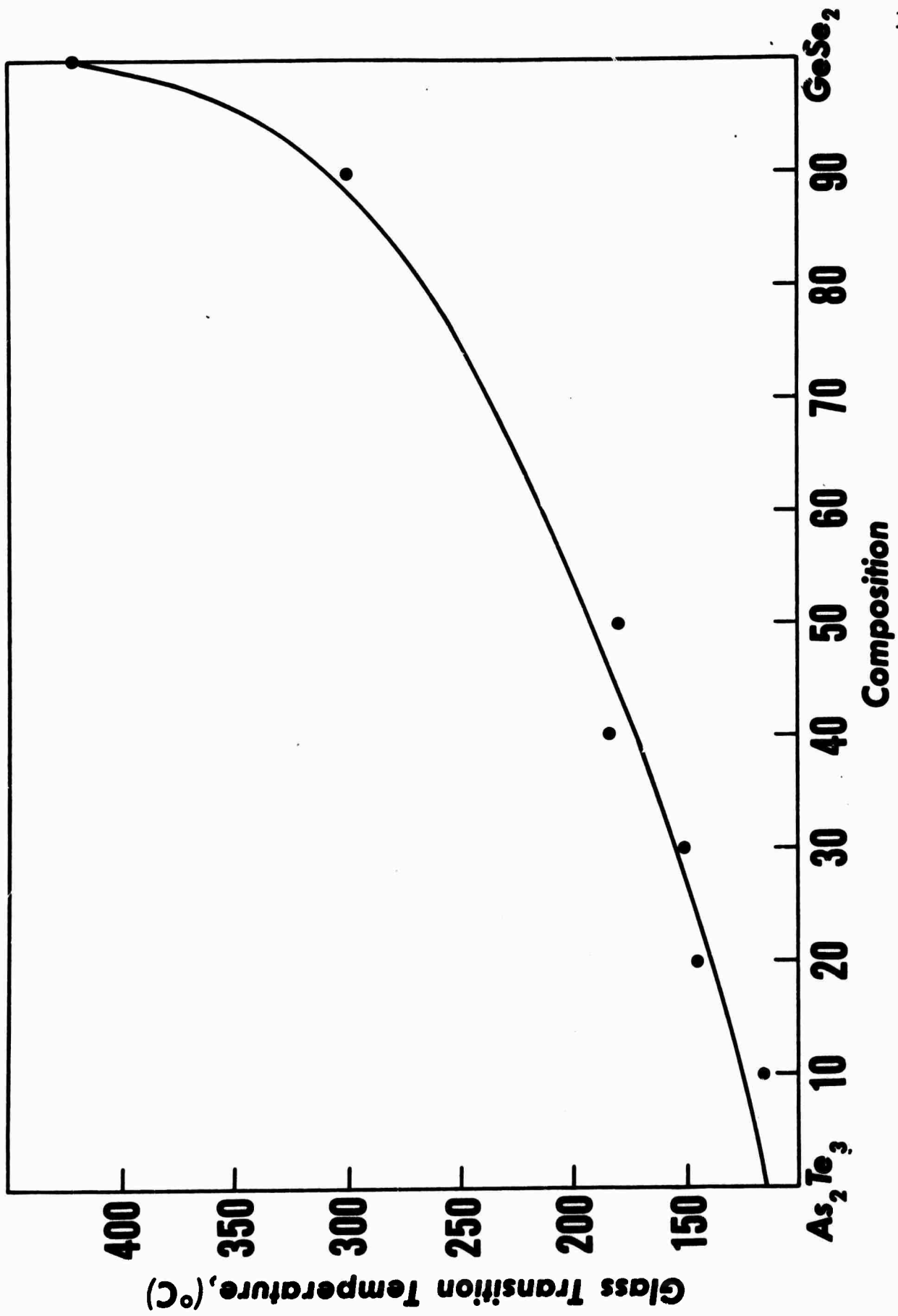


Fig. 2.3

**Fig. 2.4**

**Composition Dependence of Glass Transition Temperature  
in the Si - Te - As System**

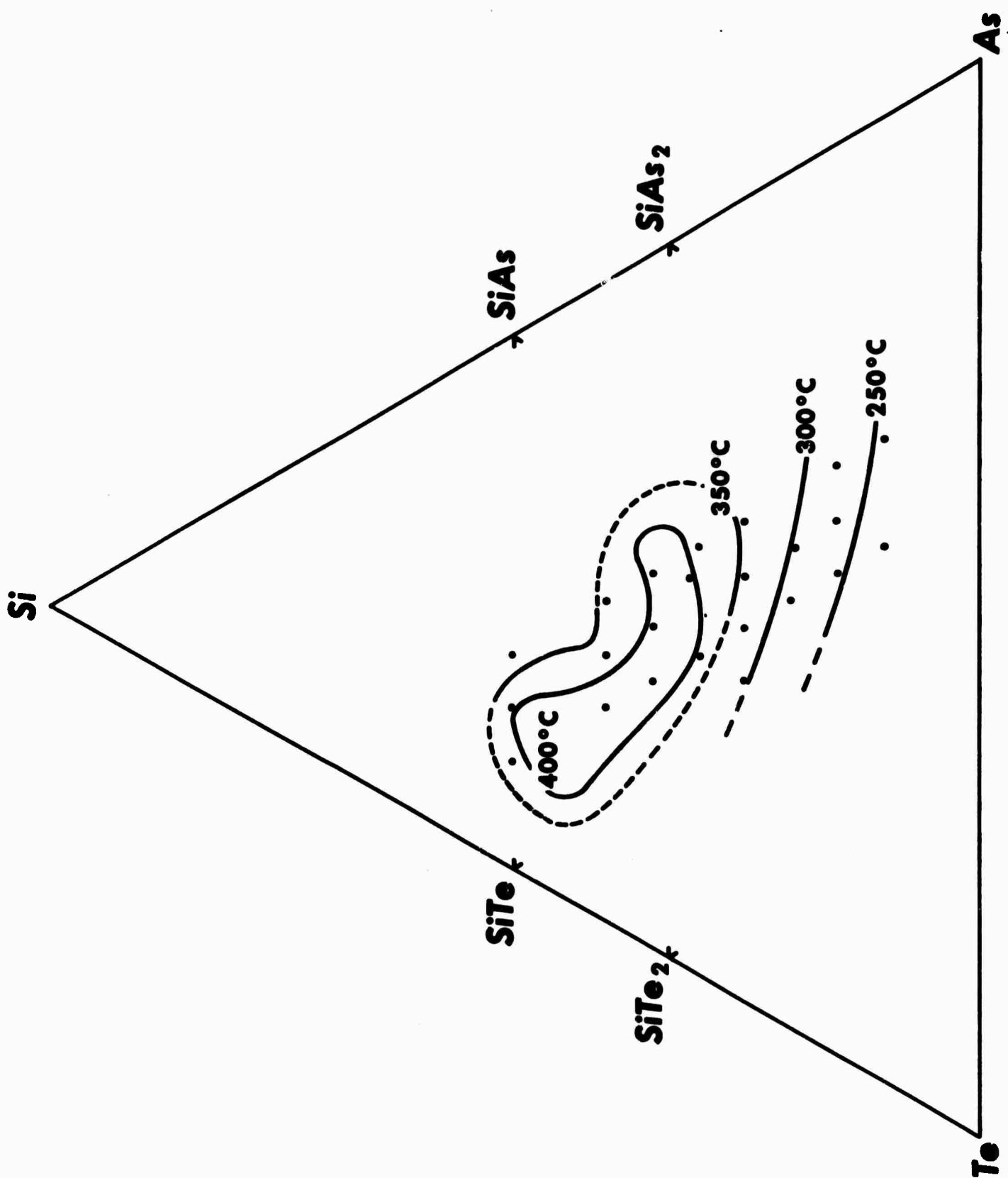


Fig. 2.4

are relatively easy glass formers and all the reported data were obtained on bulk glass samples.

Figure 2.4 reviews our present status on glass transition temperature measurements in the Te-As-Si ternary system. It supercedes Figure 2.4 in the previous semiannual technical report of this contract, which was incorrectly plotted in some copies of that report. The data were all obtained in the chalcogen unsaturated region of the system, i.e., in the region where Si-Si and As-As covalent bonds are anticipated in addition to Si-Te, As-Te and Si-As bonds. With five possible bond types, it becomes overwhelmingly difficult to determine the relative concentrations of these bonds, much less to speculate regarding bond topology once the bond concentrations have been determined. Chemical intuition suggests that the four strongest of the five probable and six possible covalent bonds are Si-Si, Si-As and Si-Te and As-As, in order of decreasing strength. Te-Te bonds are apparently the weakest.

Indeed some of the very highest  $T_g$  glasses lie entirely within the subsystem  $\text{Si-SiTe}_2 - \text{Si}_3\text{As}_4$ , i.e., they can be constructed entirely with Si-Si, Si-Te and Si-As covalent bonds. If we restrict ourselves to this subsystem and assume that only these three strongest covalent bonds are present, then every composition within this subsystem corresponds to a unique distribution of bond types. Further,

if bond strength alone determined  $T_g$ , the  $T_g$  data would plot along a smooth surface rising toward the component having the strongest bonds. However, Figure 2.4 shows that this is not the case, i.e., that  $T_g$  has a well defined maximum within this subsystem. Apparently "bond topology", most simply described in terms of the average number of bonds per atom, plays an important role in determining  $T_g$ . Specifically, the  $T_g$  maxima lie nearly along the line connecting SiTe to As, i.e., along the line of average coordination number 3. To our knowledge there currently exist no theoretical models which treat the question of network stability for three dimensional random networks as a function of the degree of connectedness (i.e., coordination number). These data represent the first indication that an average connectedness of three per atom produces the strongest network, all other factors being held constant. Indeed, such a result might be anticipated on topological grounds in considering the bond distortions encountered in constructing a structural model of a 4-connected random network.<sup>4</sup>

### 3. SURVEY OF ELECTRICAL AND OPTICAL PROPERTIES OF SPUTTERED AMORPHOUS SEMICONDUCTOR FILMS: EFFECTS OF ANNEALING

The electrical and optical properties of elemental amorphous semiconductor films have been extensively studied as a function of subsequent annealing treatment<sup>5</sup> and striking changes have been shown to occur. Therefore, a survey of amorphous semiconductor materials in sputtered film form must inevitably consider the effects of annealing in order to sample the entire spectrum of properties attainable by these materials. In the first semi-annual report of this contract we reported some observations on electrical conductivity and optical absorption of sputtered  $As_{35}Te_{28}S_{21}Ge_{16}$ , showing that a relatively large increase in the effective electrical and optical gaps occurs during annealing on the order of 1/2 hour at 150°C, and that the properties of annealed films show little hysteresis over the range 25 - 200°C. The plot of  $\log \alpha$  vs. photon energy,  $\hbar\omega$ , where  $\alpha$  is the optical absorption coefficient, showed a lateral blue shift of ~ 0.15 eV on annealing but did not show any significant change in slope. Recently, Theye<sup>5</sup> has published a careful study of the effects of annealing on the optical properties of very thin (~500 Å) evaporated amorphous Ge films showing large shifts of optical absorption and a progressive steepening of the  $\log \alpha$  vs.  $\hbar\omega$  plots as a function of annealing. We have, therefore, examined a variety of sputtered amorphous semiconductor materials of various thicknesses to see whether our previously reported annealing studies are typical of amorphous chalcogenide films and whether thick (~1 - 10  $\mu$ )

sputtered amorphous Ge films anneal like thin evaporated amorphous Ge films.

Figure 3.1 shows the temperature dependence of the electrical conductivity of a series of  $\text{GeTe}_2$  sputtered films varying from 0.6 to  $45 \mu$  in thickness measured at a scanning rate of  $\sim 3 \text{ deg min}$ . Note that all films show essentially similar features, in terms of initial activation energy ( $\sim 0.5 \text{ eV}$ ), initial conductivity, temperature of annealment ( $100 - 150^\circ\text{C}$ ), final activation energy ( $\sim 0.6 \text{ eV}$ ) and final conductivity. These curves are qualitatively similar to the conductivity data presented in Figure 4.7 of the first semi-annual technical report. We can draw the following conclusions from these results:

1. The measured conductivity is a bulk effect, in that it remains essentially constant while the sample thickness is varied over roughly two decades.
2. The annealing process appears also to be a bulk effect in that the annealing kinetics are not affected by sample thickness.
3. The annealing process does not involve atomic rearrangements (i.e., ordering, phase separation, etc.) in that the annealing temperature is  $\sim 90$  degrees below the glass transition temperature ( $\sim 230^\circ\text{C}$  measured on sputtered films), and thus atomic diffusion coefficients are essentially zero. Healing of broken bonds and release of residual stress are possible annealing mechanisms which are in accord with this requirement and with conclusion #2.

Fig. 3.1

Electrical Conductivity of Sputtered Films of  $\text{GeTe}_2$ ;  $45.5 \mu (\bullet)$ ,  
 $5.9 \mu (\Delta)$ ,  $1.10 \mu (\circ)$ ,  $1.03 \mu (\Delta)$ , and  $0.59 \mu (\blacksquare)$ .

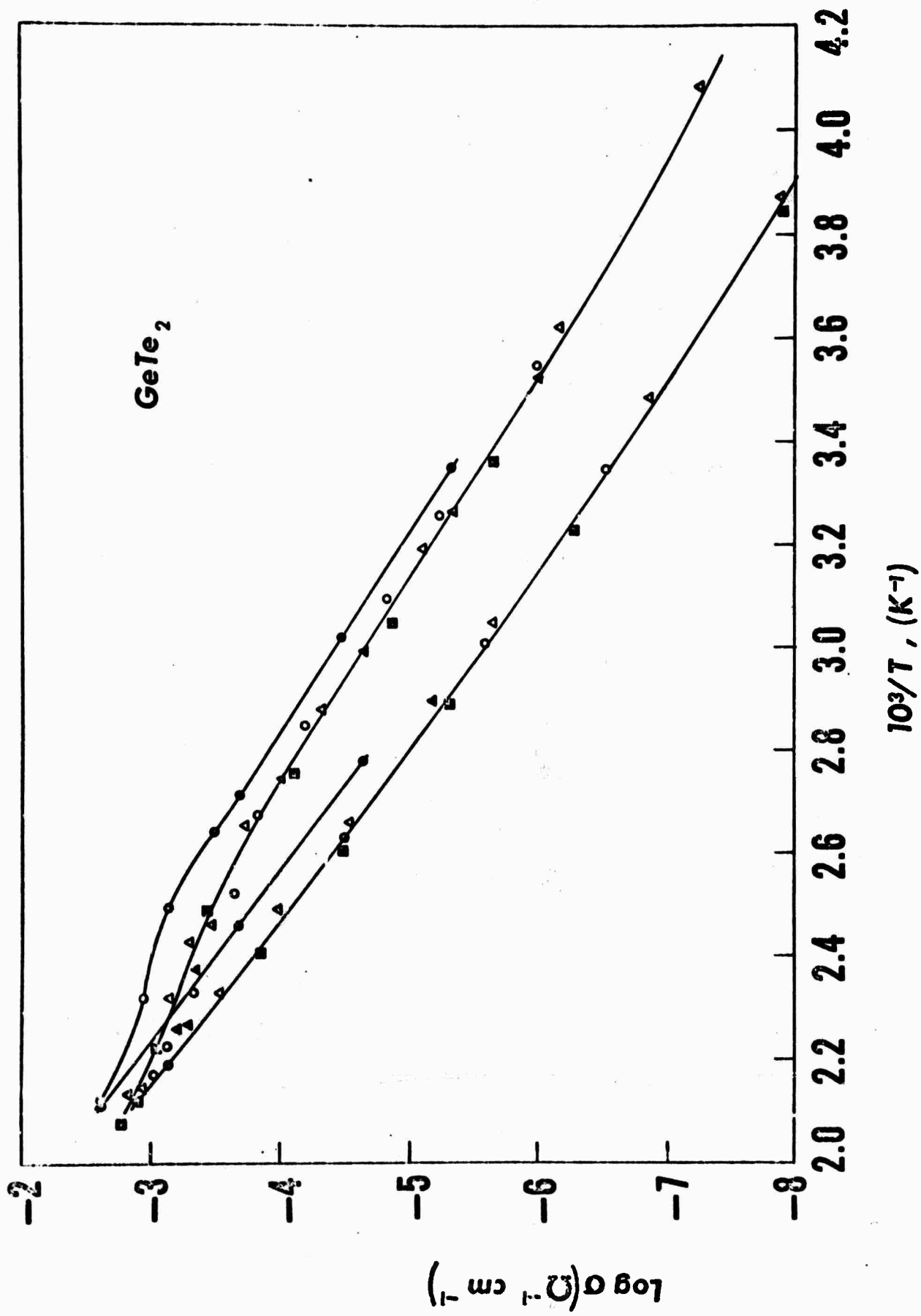


Fig. 3.1

Optical absorption data for these films were obtained before and after annealing and are plotted in Figure 3.2. Note the parallel shift to higher energies, analogous to that reported for  $As_{35}Te_{28}S_{21}Ge_{16}$  in Figure 4.8 of the first semiannual technical report. The shift of the optical absorption to higher energy is in qualitative agreement with the increase in electrical gap obtained during annealing, although the percentage of lateral blue-shift in optical absorption is smaller than the percentage increase in the slope of  $\log \sigma$  vs.  $1/T$  (7% vs. 14%).

It is interesting to note the qualitative similarity of these optical and electrical annealing effects to those previously reported for  $Te_{28}As_{35}S_{21}Ge_{16}$ .  $GeTe_2$  is considered to have a highly regular structure analogous to the  $SiO_2$  and  $GeO_2$  "random network" structures, i.e., containing essentially only Ge-Te covalent bonds, while the quaternary alloy is considered to be prototypical of a multi-component multi-bond type chalcogenide alloy. Apparently the similarity of electrical gap and glass transition temperature for these two alloys is more indicative of their relative behavior than are details of their electronic structure.

To ascertain the generality of these annealing effects for chalcogenide films we undertook to measure the electrical conductivity annealing behavior in the  $GeTe_2$  -  $GeSe_2$  system. The electrical gap before and after annealment is plotted in Figure 3.3 as a function of composition in this system. The annealment treatment consisted of heating the samples to  $225^\circ C$  in  $N_2$  gas for 1 hour, which was sufficient to saturate the annealment process without permitting any crystallization. In spite of the relatively large variation of  $T_g$

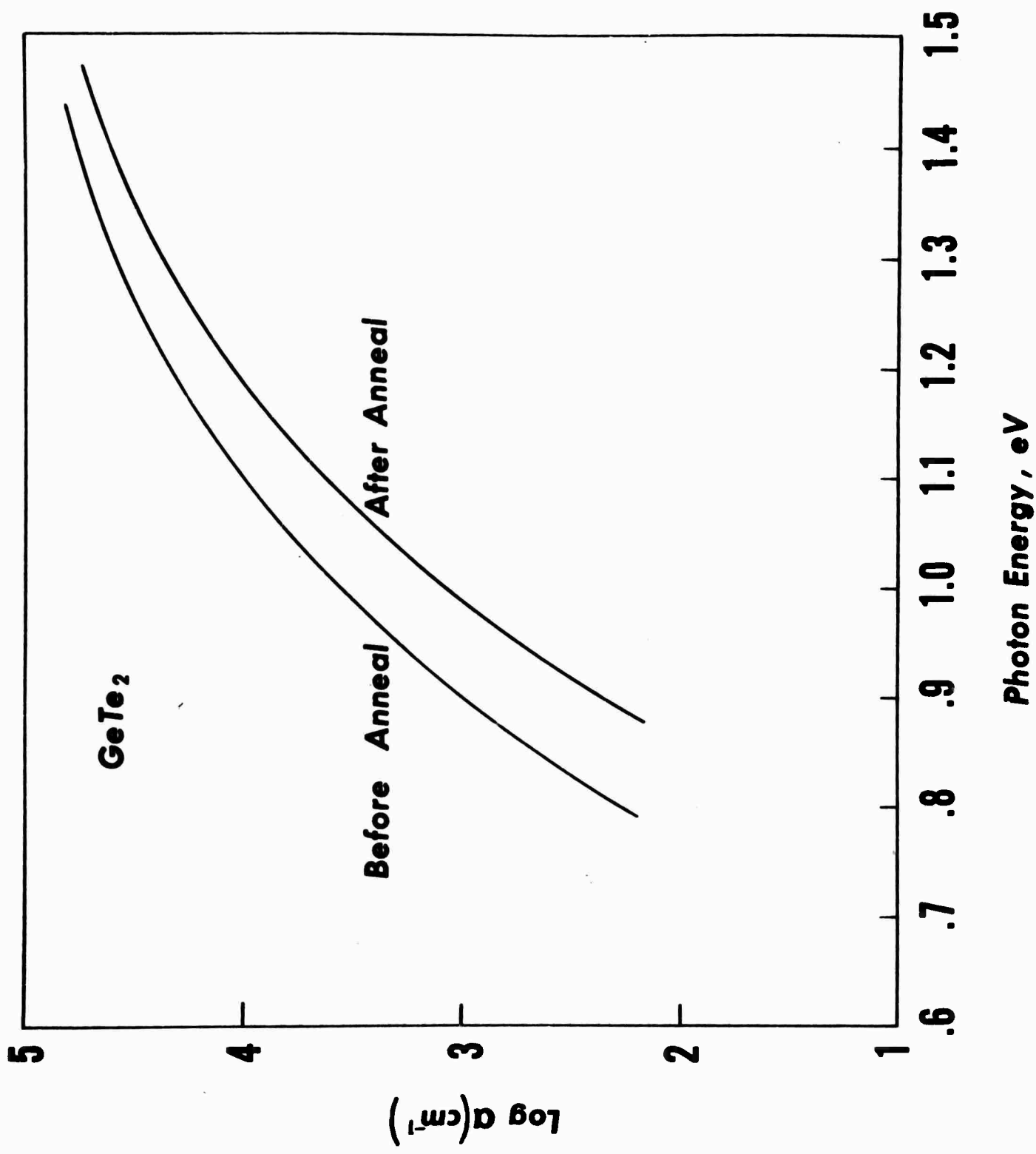


Fig. 3.2

**Fig. 3.3**

**Electrical and Optical Gap (see text) for Glasses in the  
 $\text{GeTe}_2 - \text{GeSe}_2$  System**

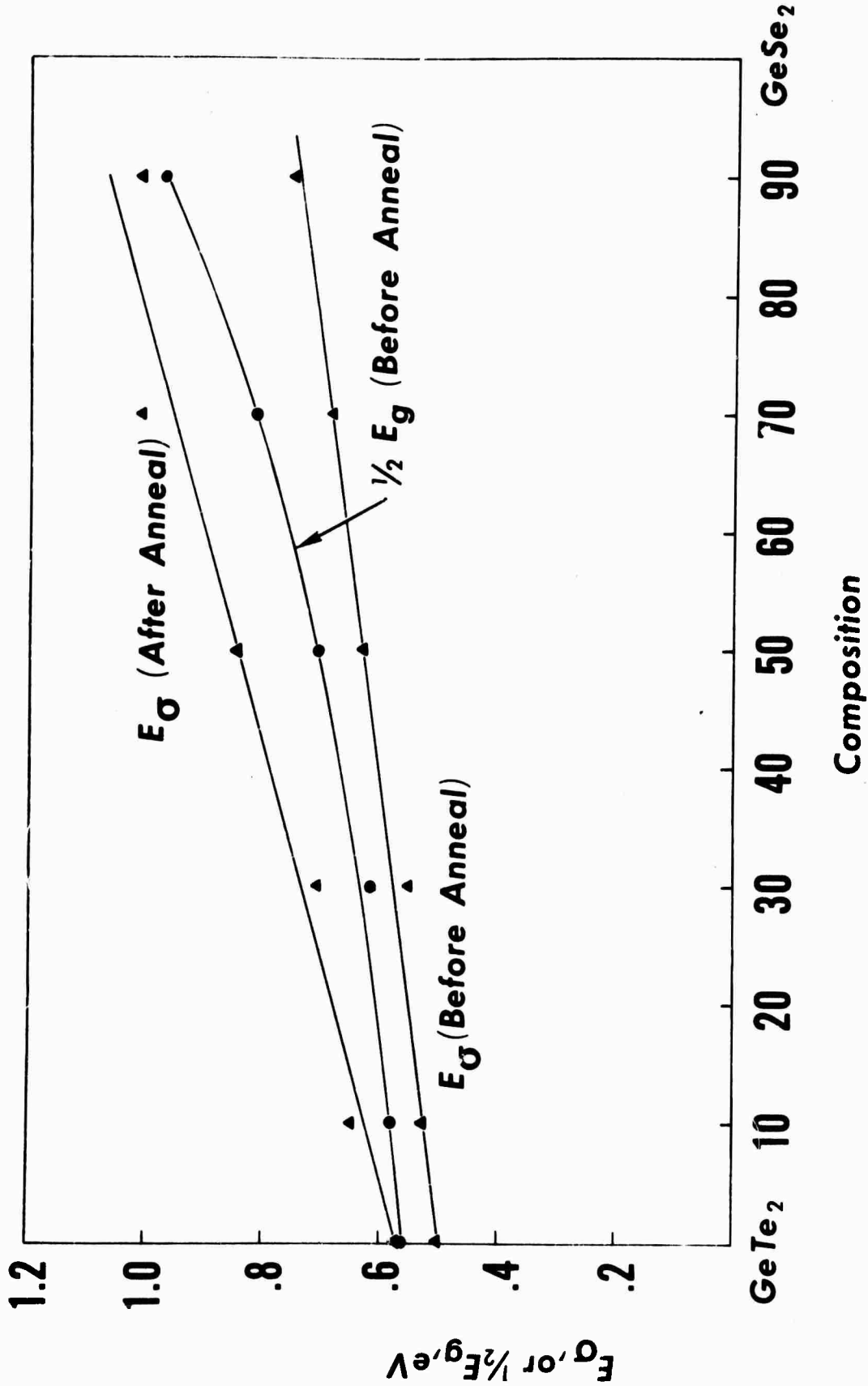


Fig. 3.3

with composition, this single annealing temperature appeared to be appropriate for all compositions examined in this system. In general, these films behaved similarly to pure  $\text{GeTe}_2$  with the exception that the magnitude of the relative annealing shift of the electrical gap increased substantially with increasing  $\text{GeSe}_2$  content. Optical absorption studies on  $(\text{GeTe}_2)_{90}(\text{GeSe}_2)_{10}$  and  $\text{GeTeSe}$  indicate that the  $\log \alpha$  vs. photon energy curves shift laterally to higher energies in analogy to the data presented for  $\text{GeTe}_2$  and  $\text{As}_{35}\text{Te}_{28}\text{S}_{21}\text{Ge}_{16}$ . The relative magnitude of these annealing effects appears to be related to the difference between the deposition temperature and the glass transition temperature, as indicated by a comparison of Figure 3.3 with Figure 2.1 on page 5, i.e., the greater the departure, the greater the annealing effect. This result can be understood equally well in terms of a bond healing model or a stress relief model for annealing.

In order to compare the composition dependence of optical absorption and electrical conductivity in this binary system, the photon energy at which the optical absorption coefficient attains  $10^4 \text{ cm}^{-1}$  for the freshly deposited films has been divided by 2 (an arbitrary normalizing factor to make the optical data and the electrical data more closely comparable) and plotted as "optical gap" in Figure 3.3. Note that the "optical gap" thus defined departs progressively from the "electrical gap" of the unannealed films.

In order to reconcile this annealing behavior with the amorphous Ge data,<sup>5</sup> we have measured the optical absorption of two sputtered samples of amorphous Ge, one  $19 \mu\text{m}$  and one  $0.35 \mu\text{m}$  thick. Data were obtained for

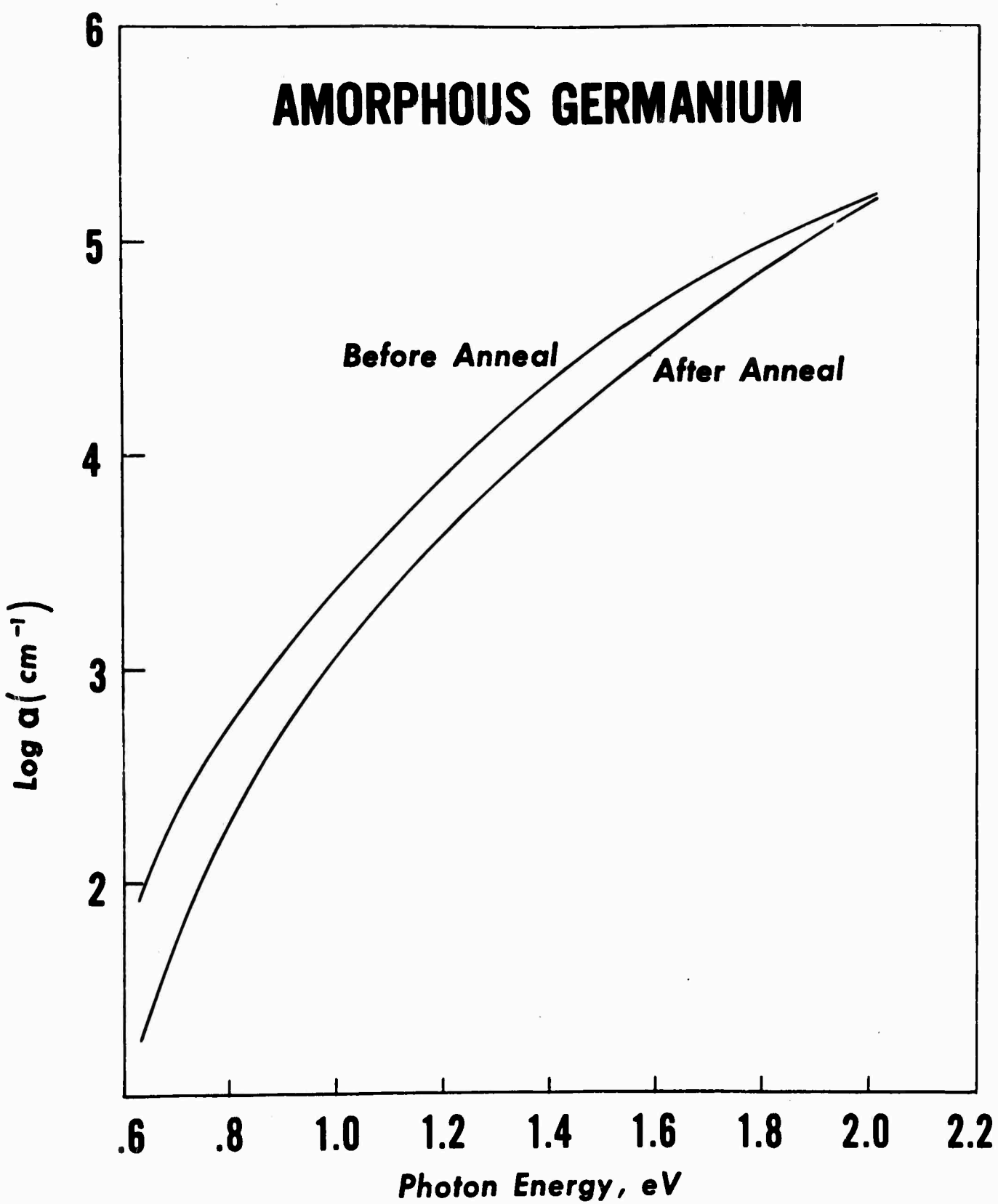


Fig. 3.4

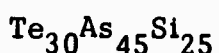
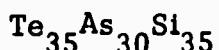
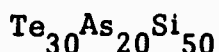
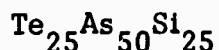
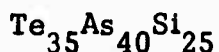
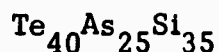
the films in the freshly deposited condition and after annealment at  $220^{\circ}\text{C}$  for two hours. In this case the annealment cannot be considered complete; abundant evidence<sup>5</sup> suggests that amorphous Ge anneals progressively with temperature increases up to  $\sim 300^{\circ}\text{C}$ . However, the present experiment is sufficient to distinguish the direction and character of the annealing process. Note first that the slope of  $\log \alpha$  vs. photon energy before and after annealment is of the order of  $1.25 \text{ eV}^{-1}$  in the  $\log \alpha = 3-4$  range vs.  $\sim 2.5 \text{ eV}^{-1}$  for the chalcogenides in the same absorbing range. Also, note that the effect of annealing is to shift the slope of  $\log \alpha$  vs. photon energy curve rather than to translate the curve laterally, i.e., the magnitude of the change of  $\log \alpha$  is greater at lower energies and almost zero at 2 eV. However, no indication of a sharp edge, as reported by Theye<sup>5</sup> on the evaporated films annealed at a similar temperature, is observed. This discrepancy may derive from the greater (10X - 400X) thickness of the present samples or from the nature of defects introduced by sputtering relative to evaporation deposition. In either case, the present results are in agreement with Theye's results in the sense that the initial slope of  $\log \alpha$  vs. photon energy is much lower than for the chalcogenides and that the annealing process involves an increase in this slope rather than a lateral blue shift of optical absorption as in the chalcogenides.

In addition to the above reported annealing effect studies, we have continued our survey of optical absorption and electrical conductivity of sputtered thin film samples of new materials in the freshly deposited

amorphous state. We have measured the compositional dependence of optical absorption and reflectivity in the  $\text{As}_2\text{Te}_3$ -rich portions of the  $\text{As}_2\text{Te}_3 - \text{GeTe}_2$  and the  $\text{As}_2\text{Te}_3 - \text{Ga}_2\text{Te}_3$  pseudobinary systems whose glass transition temperature was previously reported<sup>15</sup> as a function of composition. Both systems show slight increases of electrical and optical gaps with the progressive addition of  $\text{GeTe}_2$  and  $\text{Ga}_2\text{Te}_3$  respectively, although the observed increases are scarcely outside the scatter of the data (~5%).

We have also measured the optical absorption of a series of sputtered Te-As-Si films from compositions in the high glass transition temperature portion of this system as reviewed in Chapter 2. of the present report. While the scatter of these data was larger than usual (i.e., ~ 10%), probably due to compositional variations from run to run (the cathodes were inhomogeneous in some cases due to fabrication difficulties), the variation of optical absorption with composition in the  $\log \alpha = 4-5$  range for all six compositions tested was only about 5 fold, with  $\alpha = 10^4 \text{ cm}^{-1}$  at an average energy of 1.55 eV.

The compositions tested were as follows:



Unfortunately these films were deposited on electroded substrates which were inappropriate for measuring the conductivity of such large gap materials so that no electrical data could be obtained for comparison. Several 4-point probe measurements of these materials at room temperature indicated resistivities in the range  $10^{10} - 10^{11} \Omega\text{cm.}$

#### 4. TRANSPORT MEASUREMENTS

##### 4.1 Thermoelectric Measurements

###### 4.1.1 Introduction

The thermoelectric power, or Seebeck coefficient S, was measured for a number of chalcogenide films. Purposes of the study are to gather information about the transport mechanisms and to determine the most suitable amorphous chalcogenide materials for high temperature thermoelectric generation. Annealing studies were included.

Chalcogenide compositions which were studied include the  $(GeTe_2)_x (GeSe_2)_{1-x}$  system,  $As_2Te_3$ ,  $Ge_{15}Te_{81}Sb_2S_2$ ,  $Te_{40}As_{35}Si_{18}Ge_7$ , and  $Ge_{16}As_{35}Te_{28}S_{21}$ . These compositions include stoichiometric materials and complex multi-component alloys. The observed Seebeck coefficients were large and positive, being of the order of 1 mV/deg for all amorphous materials studied. Electrical conductivities for these amorphous materials are also small, so that the highest thermoelectric figure of merit estimated to date,  $10^{-6} \text{ deg}^{-1}$ , is two to three orders of magnitude smaller than that obtained for the best crystalline materials such as InSb. However, some of the amorphous materials are stable to fairly high temperatures where the electrical conductivity becomes sizeable, and the figure of merit increases nearly

exponentially in  $(-1/T)$  for a given material. It is therefore possible to improve the value for amorphous materials by examining at higher temperatures materials which resist crystallization under these conditions.

The thermoelectric power was found to be very sensitive to annealing, with the thermopower changing in annealing ranges where the electrical conductivity did not change. Apparently the thermoelectric power is much more sensitive to subtle structural changes and perhaps to impurities than is the conductivity.

The theoretical formulas for the temperature dependence of the Seebeck coefficient contain a parameter A which, in the case of crystalline semiconductors, is usually 1 to 4 depending upon the carrier scattering mechanism. Treating A as a disposable parameter, we find for our materials in various stages of annealment that A ranges from about -10 to +4. The negative values are extremely puzzling. Nevertheless, it is interesting to note the trend in A as a function of composition and annealing. It appears that A might be considered to be a disorder parameter, with A being largest for the material with the greatest disorder. For example, materials with both structural and compositional disorder, such as  $Ge_{15}Te_{81}Sb_2S_2$ , give  $A \sim 4$ . Unannealed  $As_2Te_3$  and

$\text{GeTe}_2$  also give  $A \sim 3$  to 4, but  $A$  decreases progressively with annealing for these latter materials, becoming large and negative for heavy annealing.

It also appears that thermoelectric data for the complex alloys may be best explained by the assumption of a temperature-dependent mobility, whereas such a mobility is not implied for simpler compositions in their annealed states.

#### 4.1.2 Experimental Procedure

Thermoelectric power and electrical conductivity are measured consecutively in the same apparatus with the sample in a vacuum chamber. Film samples on sapphire substrates, with molybdenum electrodes, are in the configuration of Fig. 4.1.

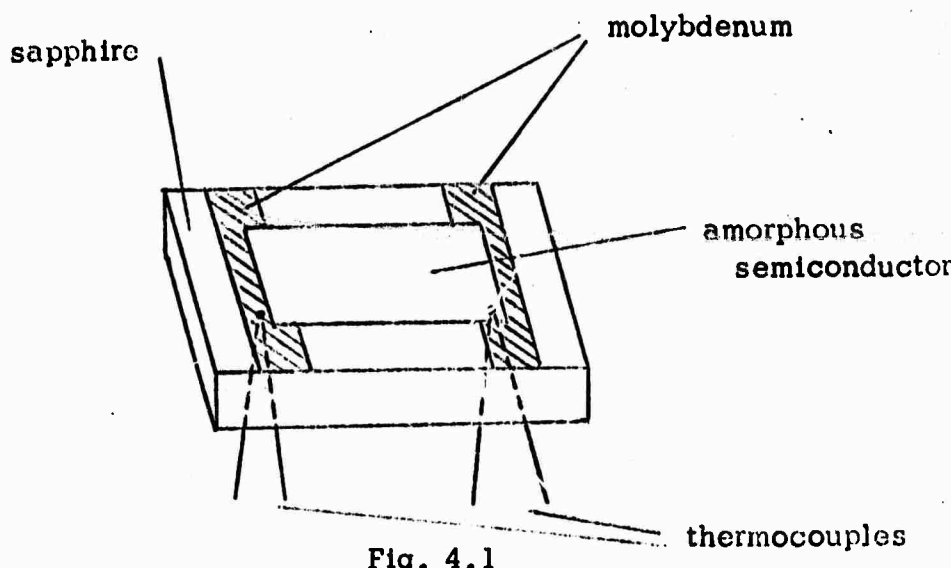


Fig. 4.1

The substrate is contacted on each end by independently controlled heater coils to provide the reference temperature  $T$ , and the temperature difference across the sample  $\Delta T$ .

Copper-constantan thermocouples attached to the back face of the sapphire substrate and aligned with the electrodes measure the temperatures of the ends of the sample. Because of the design,  $\delta T$  across the substrate thickness is negligible. The Seebeck voltage  $\Delta V$  and the temperatures  $T$  and  $\Delta T$  are measured with a Keithley 610 CR electrometer and a Keithley 149 voltmeter, respectively. As the temperature of one end of the sample is varied relative to the other,  $\Delta V$  vs  $\Delta T$  is automatically recorded - the slope gives the Seebeck coefficient at a particular reference temperature.  $S$  can be measured for sample resistances up to  $10^{10}$  or  $10^{11}$   $\Omega$ .

When  $S(T)$  and  $R(T)$  are measured, generally  $S(T)$  is measured as the sample is heated, and  $R(T)$  is measured continuously as the sample cools with no input to the heater coils, so that the sample temperature is nearly uniform for the resistance measurement. For detailed studies of the effect of annealing, another procedure is also used. In this procedure, the sample is annealed briefly at a given temperature  $T_a$ , and  $S$  and  $R$  are both measured at a certain low temperature  $T_m$ . The sample is then annealed at successively higher temperatures and  $S(T_m, T_a)$  and  $R(T_m, T_a)$  can be plotted vs  $T_a$ .

Materials which have been studied include the  $(\text{GeTe}_2)_x(\text{GeSe}_2)_{1-x}$  system,  $\text{As}_2\text{Te}_3$ ,  $\text{Ge}_{15}\text{Te}_{81}\text{Sb}_2\text{S}_2$ ,  $\text{Te}_{40}\text{As}_{35}\text{Si}_{18}\text{Ge}_7$ , and  $\text{Ge}_{16}\text{As}_{35}\text{Te}_{28}\text{Sb}_{21}$ . All samples were films sputtered onto substrates held at  $\sim 40^\circ\text{C}$ .

#### 4.1.3 Results

Figure 4.2 summarizes  $S(T)$  for some of these materials in the virgin or unannealed state. The samples of  $(\text{GeTe}_2)_{.9}(\text{GeSe}_2)_{.1}$  and  $(\text{GeTe}_2)_{.7}(\text{GeSe}_2)_{.3}$  may not be equivalent to virgin samples, since they were exposed to temperatures of about  $70^\circ\text{C}$  or more during processing. Data for all samples measured was usually well presented by a linear  $S$  vs  $1/T$  plot. All materials studied have shown positive thermopowers with a negative temperature dependence in the virgin state. The thermoelectric power was of the order of 1 to 1.5 mV/deg between  $-30$  to  $+125^\circ\text{C}$  for all virgin materials.

Figure 4.3 illustrates the annealing behavior of  $S(T)$  and  $\sigma(T)$  for a  $\text{GeTe}_2$  sample. For annealing temperatures up to  $150^\circ\text{C}$ ,  $S$  increases as the conductivity activation energy  $\Delta E_\sigma$  increases, and the conductivity simultaneously decreases. However, the most striking changes in  $S$  with annealing occur near and above  $238^\circ\text{C}$ , where the conductivity change has saturated. In this latter annealing region,  $S$  actually increases to a maximum and then decreases. Thus, in certain annealing regions the thermopower is more sensitive to annealing than is the conductivity.

Fig. 4.2

Seebeck coefficient vs  $10^3/T$  for several amorphous chalcogenide films in the virgin or near-virgin state. Two materials, labeled (l.a.), were lightly annealed.

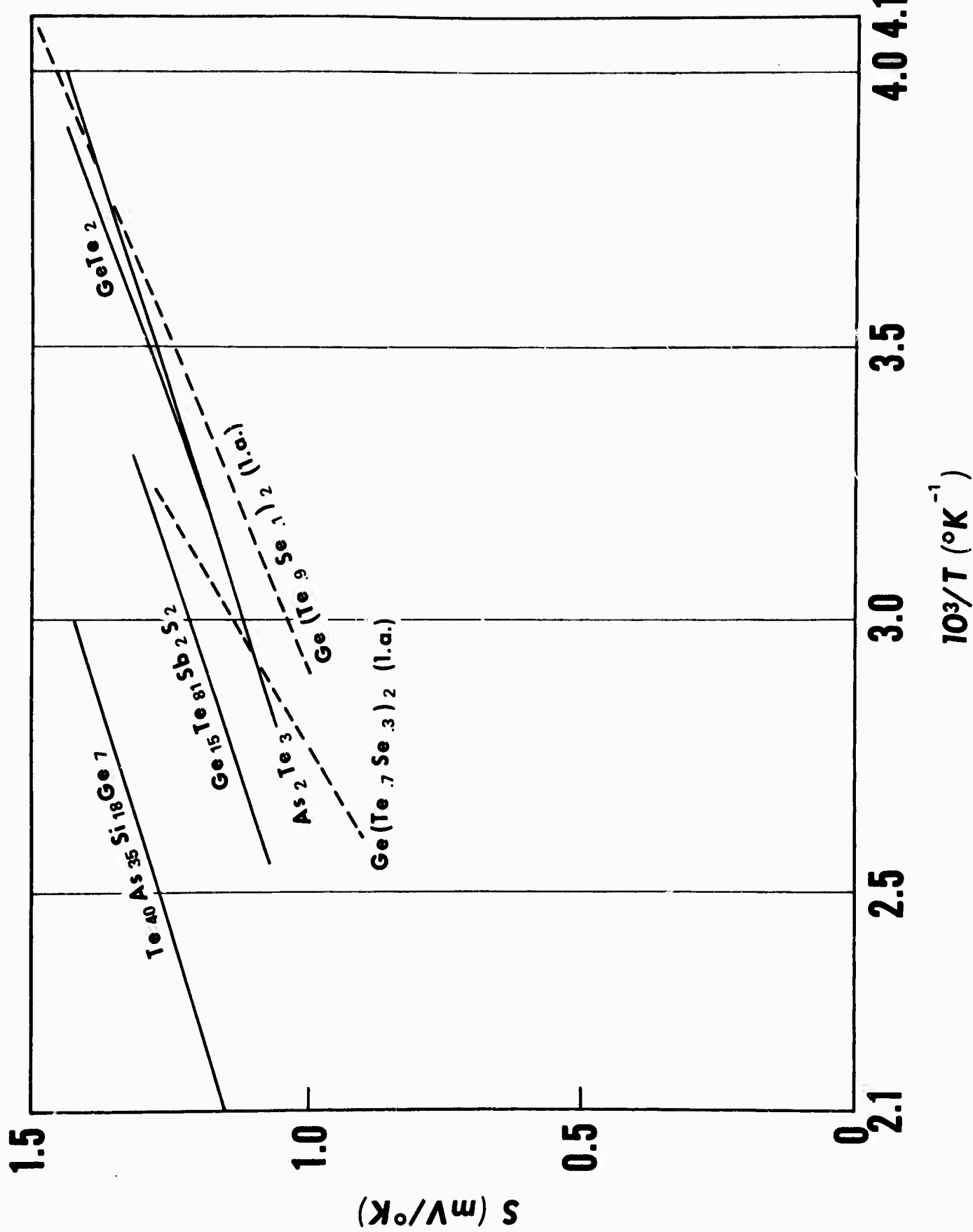


Fig. 4.2

Fig. 4.3

Seebeck coefficient and Electrical conductivity for a  $\text{GeTe}_2$  film in the virgin state and after annealing briefly at each of several annealing temperatures. The insert shows the Seebeck coefficient and conductivity measured at  $60^\circ \text{C}$  as a function of annealing temperature.

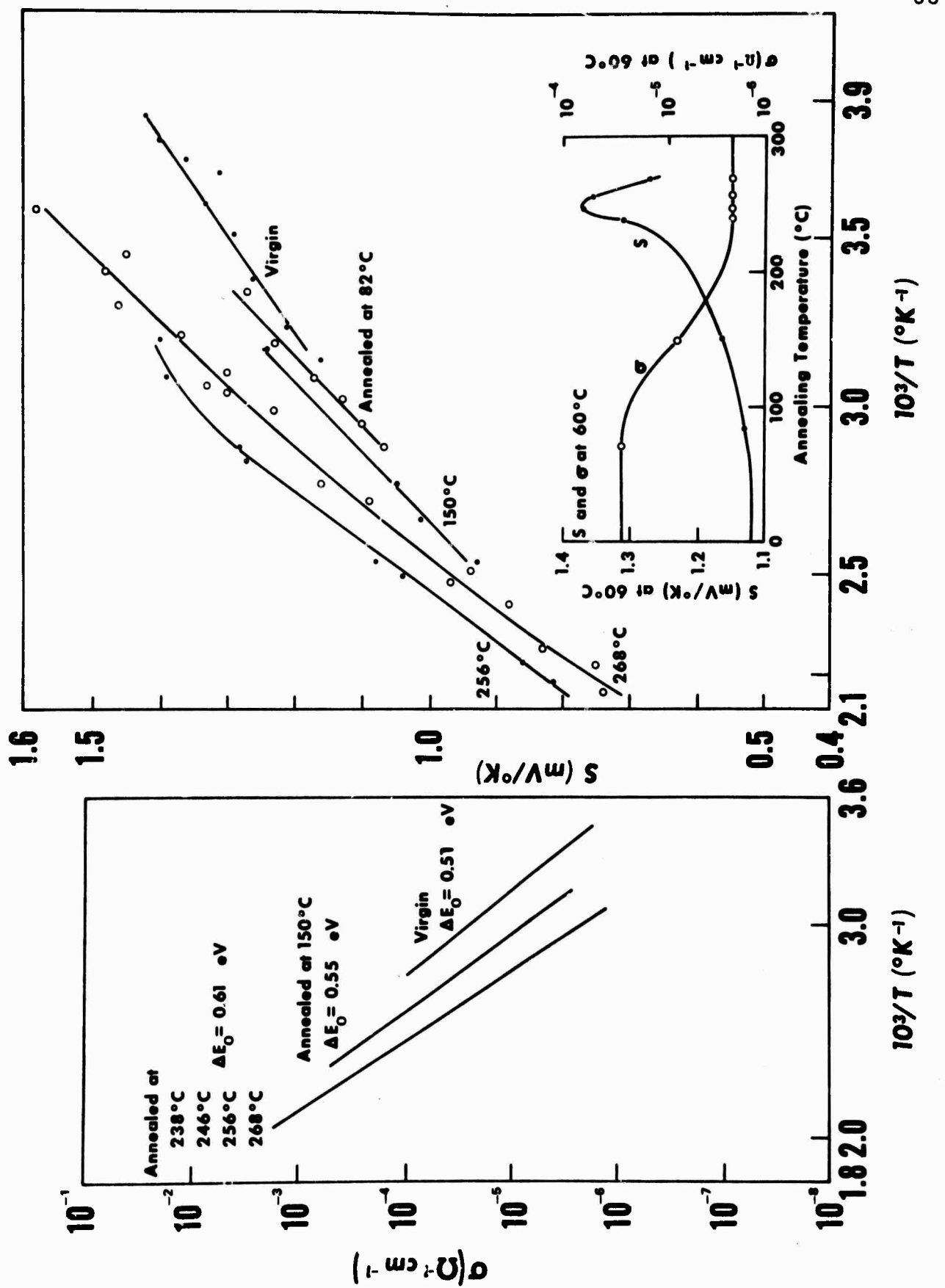


Fig. 4.3

The annealing behavior of  $S(T)$  and  $\sigma(T)$  for a nominal  $Ge_{15}Te_{81}Sb_2S_2$  film is shown in Figs. 4.4 and 4.5. Unfortunately, this sample is apparently impure due to temporary problems in sputtering. Nevertheless, except for somewhat different slopes and activation energies, its gross behavior is likely to be qualitatively the same as properly prepared material, which will be rerun later.

$S(T)$  in the virgin state and when annealed up to  $155^\circ C$  is linear with  $1/T$ . At annealing temperatures above  $194^\circ C$ ,  $S$  dropped while  $\sigma$  rose. The slope of  $S$  vs  $1/T$  went to zero even though  $S$  itself was still 0.4 to 0.55 mV/deg, and the conductivity activation energy decreased.  $\sigma(T_m, T_a)$  and  $S(T_m, T_a)$  with  $T_m = 87^\circ C$  are plotted vs the annealing temperature  $T_a$  in Fig. 4.5a). The conductivity activation energy  $\Delta E_\sigma$  and  $\Delta E_s$  are plotted vs  $T_a$  in Fig. 4.5 b), illustrating the abrupt change in behavior between 160 and  $190^\circ C$ . Obviously there is a change in the conduction mechanism as the material is annealed at those temperatures. The  $\sigma(1/T)$  data in Fig. 4.4 for the annealed states show considerable curvature, which may represent an extrinsic type of conduction rather than representing a drastic reduction of the intrinsic activation energy with annealing. That is, the annealed  $\sigma - 1/T$  data for  $T_a = 194^\circ, 214^\circ, 266^\circ C$  can be

Fig. 4.4

Seebeck coefficient and electrical conductivity for a  $\text{Ge}_{15}\text{Te}_{81}\text{Sb}_2\text{S}_2$  film in the virgin state and after annealing briefly at each of several annealing temperatures. The film is highly crystallized after annealing at and above  $194^\circ\text{C}$ .

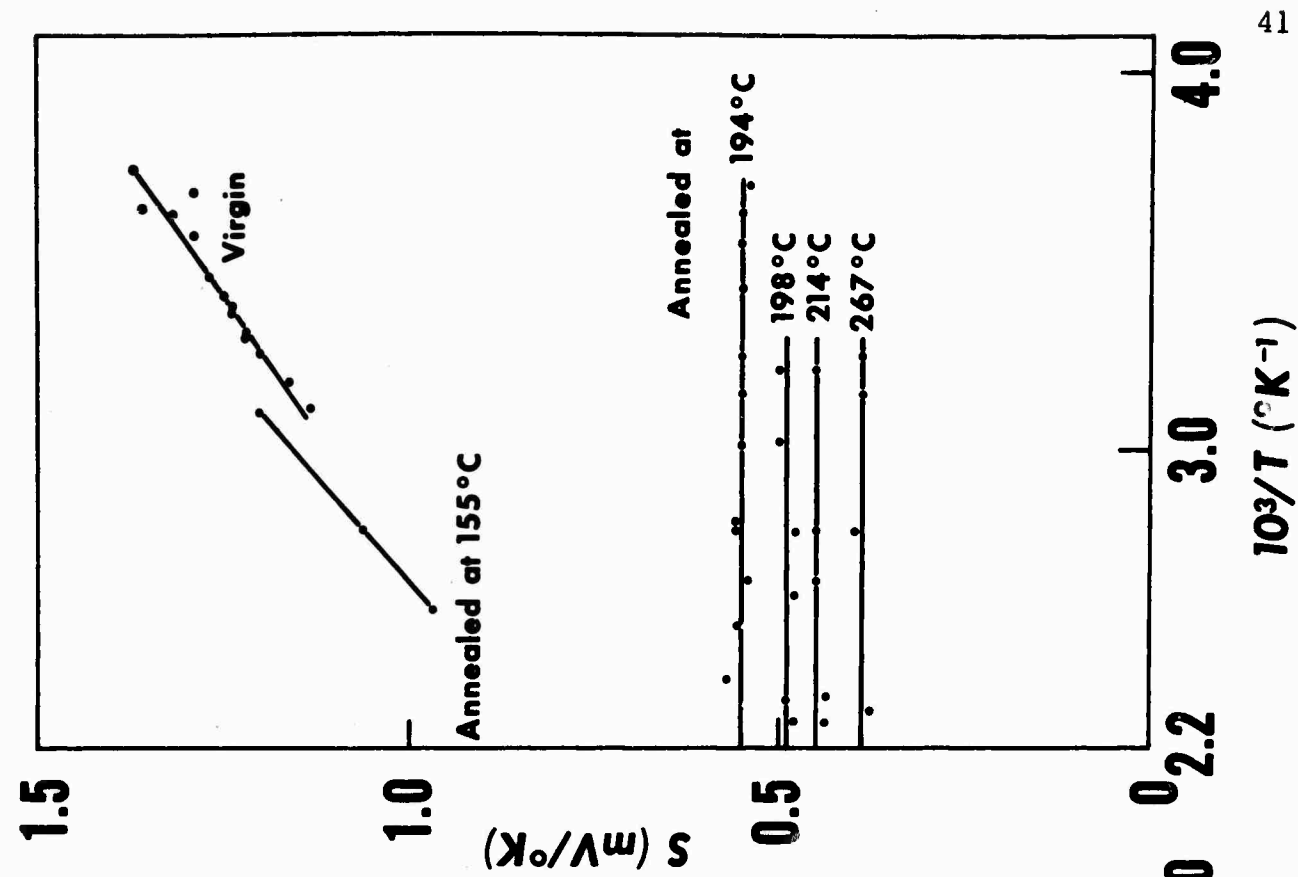
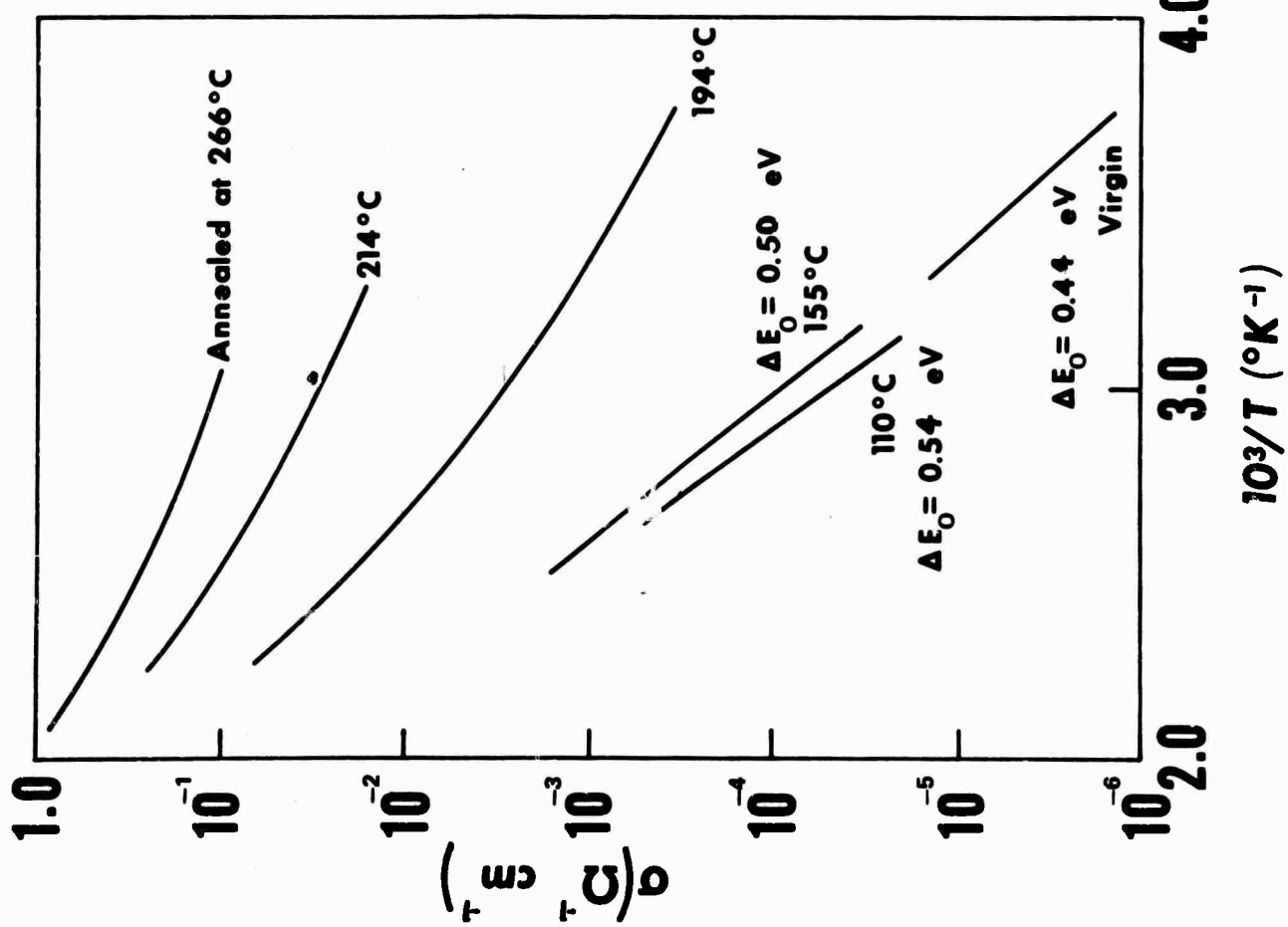


Fig. 4.4

extrapolated to give at higher temperatures approximately the same intrinsic activation energy as the 0.5 eV of the data for  $T_a = 155^\circ \text{ C}$ . Such annealing behavior has been shown in detail for another chalcogenide alloy by Fagen and Fritzsche<sup>6</sup> in their Fig. 1. Nevertheless, in view of the temperature dependent conductivity, the temperature independent thermopower is difficult to explain. X-Ray analysis indicates that in the last annealing stages, at and above  $194^\circ \text{ C}$ , the material contains Te crystallites in an amorphous matrix. Crystallization began with annealing between  $155^\circ$  and  $194^\circ \text{ C}$ .

Figure 4.6 shows the temperature dependence of thermopower for an  $\text{As}_2\text{Te}_3$  film in the amorphous state and after crystallization. Curve a) contains data points from several annealing steps up to  $110^\circ \text{ C}$ . Although the thermopower did not change during these steps, the conductivity increased modestly by  $\sim 50\%$  and the activation energy increased from 0.43 to 0.47 eV.

Heating to about  $160^\circ \text{ C}$  gave curve b). X-Rays showed the material at that stage to be essentially crystallized, containing crystalline phases not identifiable as either crystalline  $\text{As}_2\text{Te}_3$  or Te. In this crystallized state the thermopower is small and positive, and its magnitude increases with temperature. The conductivity at room temperature increased

Fig. 4.5

Upper: Seebeck coefficient and electrical conductivity measured at 85° C as a function of annealing temperature for the  $Ge_{15}Te_{81}Sb_2S_2$  film of Fig. 4.4.

Lower: Conductivity activation energy  $\Delta E_0$ , slope of  $eS$  vs  $1/T$ ,  $\Delta E_s$ , and  $\Delta E$ , where  $\Delta E$  is obtained from the slope of the  $\sigma$  vs  $1/T$  curves in the annealing region where intrinsic conduction was not observed, all vs annealing temperature.

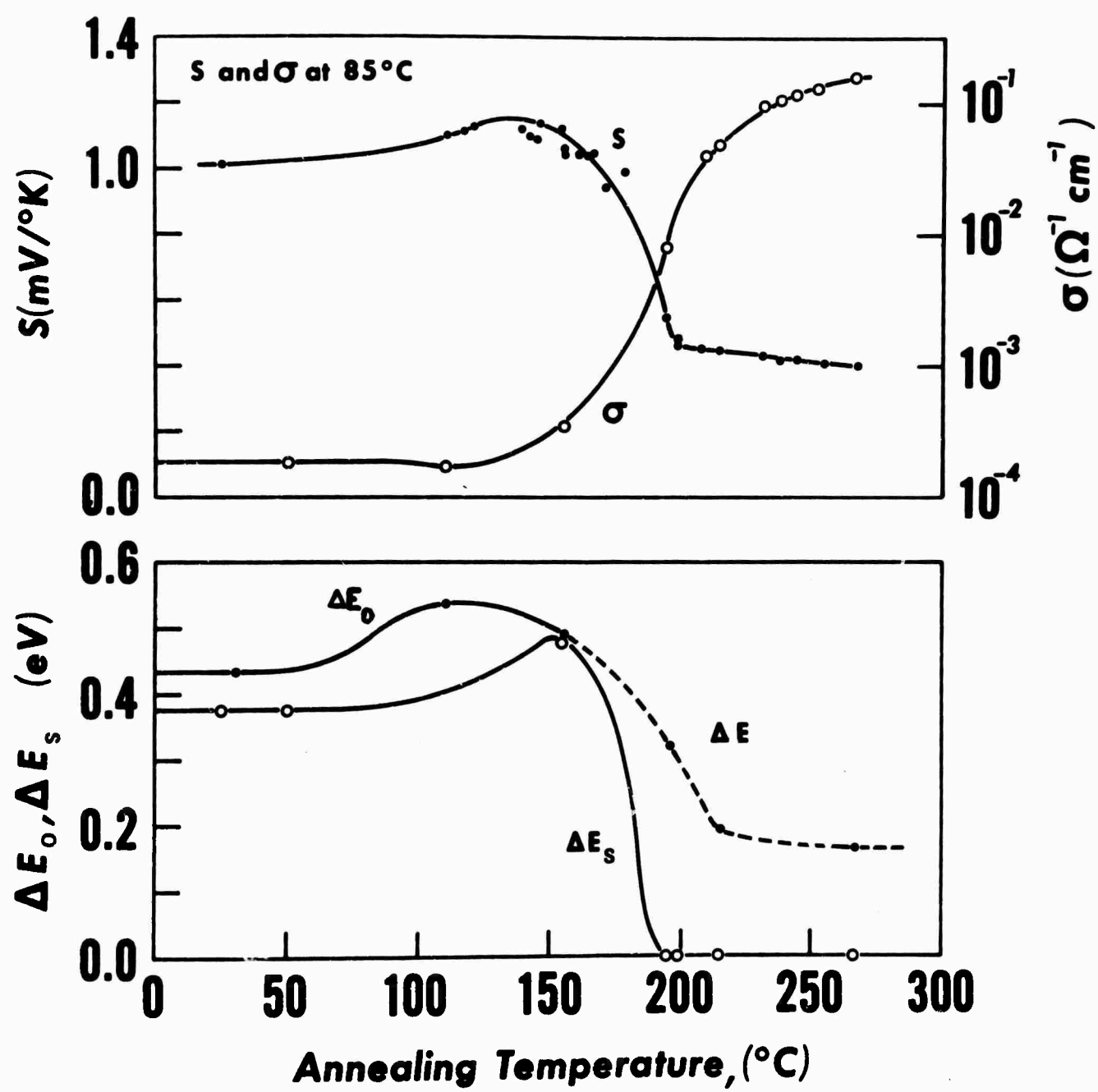


Fig. 4.5

Fig. 4.6

- a) Seebeck coefficient vs  $10^3/T$  for an as-sputtered amorphous  $As_2Te_3$  film.
- b) Seebeck coefficient, after annealing at  $160^\circ C$  has brought about crystallization.

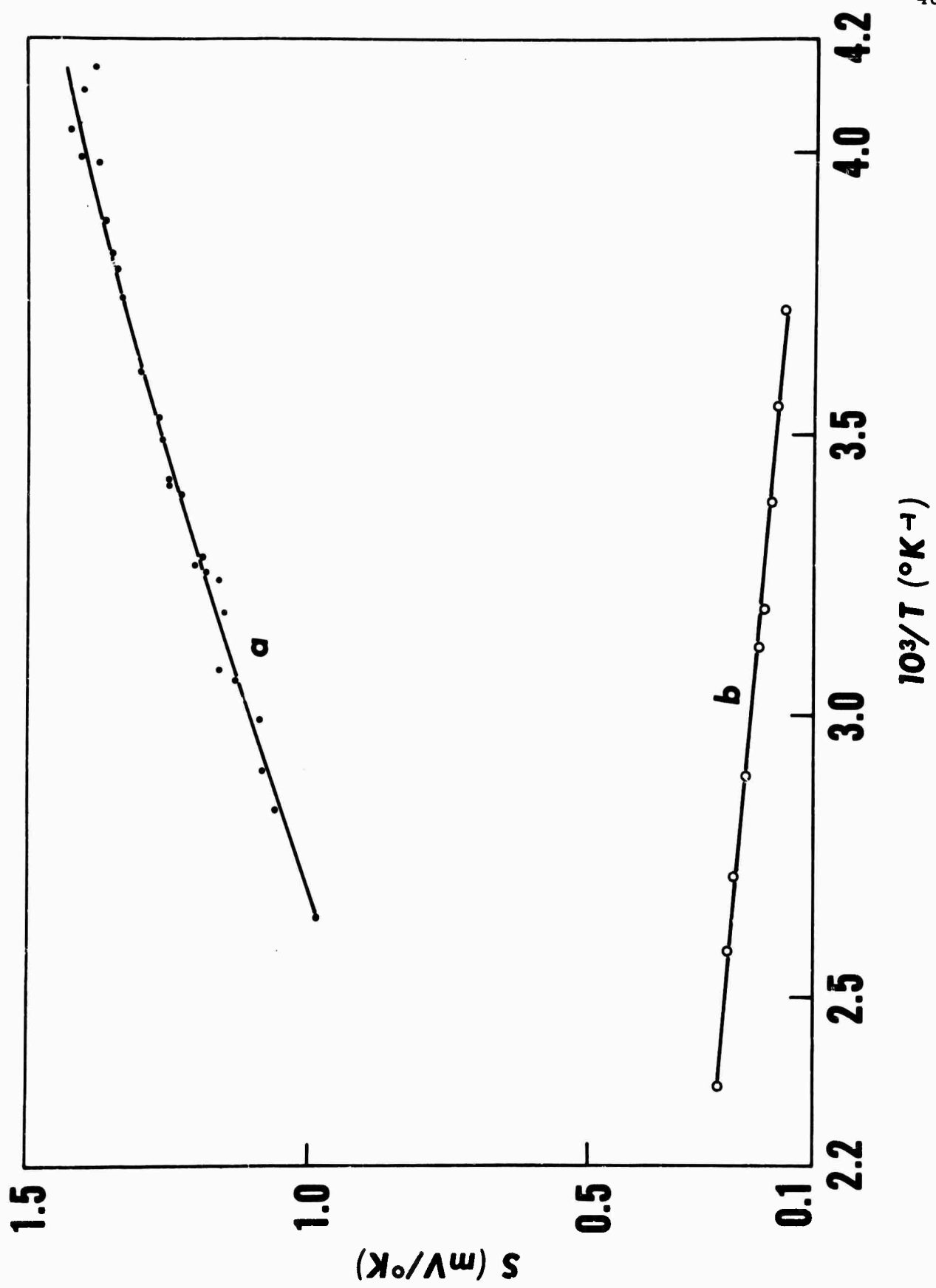


Fig. 4.6

from about  $6 \times 10^{-5} \Omega^{-1} \text{cm}^{-1}$  in the amorphous state to  $6 \Omega^{-1} \text{cm}^{-1}$  in the crystallized state.

The activation energy for these sputtered  $\text{As}_2\text{Te}_3$  films is somewhat higher than the  $\sim 0.39$  eV observed for evaporated  $\text{As}_2\text{Te}_3$ <sup>2,3</sup> and the conductivity is accordingly less. The discrepancy is not understood.

Figures 4.3 and 4.4 illustrate annealing effects on two widely different types of materials. In general, we have found that the thermopower is very sensitive to subtle differences in samples which are not seen in conductivity, optical absorption, or X-ray measurements. For example, another  $\text{GeTe}_2$  sample nominally identical with that of Fig. 4.3 had a thermopower which annealed down only, rather than up before down, illustrating that subtle differences in the two samples were detected by thermopower measurements.

Generally, intrinsic conductivity activation energies  $\Delta E_o$  were greater than slopes  $\Delta E_s$  obtained from  $eS$  vs  $1/T$ .  $\Delta E_o$  and  $\Delta E_s$  are summarized in Table 4.1 for a number of materials at various annealing stages.

#### 4.1.4 Structure

The  $(\text{GeTe}_2)_x(\text{GeSe}_2)_{1-x}$  films with  $x = 1.0$ ,  $0.9$ , and  $0.7$  also were amorphous to X-rays at the annealing stages examined up to  $250^\circ \text{C}$ . That is, for all the annealing stages considered

TABLE 4.1

Composition	Sample	Virgin, or Annealed at	$\Delta E_s$	$\Delta E_o$	$\Delta E_o - \Delta E_s$	$A_2 - \frac{\beta_h}{k}$	$A_1 - \frac{\beta_h}{k}$
GeTe <sub>2</sub>	A	Virgin	0.34	0.46	0.12	1.4	1.9
		173-230°C	0.40	0.57 - 0.60	0.17 - 0.20	-1.4	-2.0
	C	254°C	0.57	0.60	0.03	-8.4	-8.8
As <sub>2</sub> Te <sub>3</sub>	A	Virgin	0.36	0.51	0.15	0.4	0.6
		54°C	0.32	0.46	0.13	1.2	2.1
	B	118°C	0.34	0.47	0.13	1.0	1.4
Ge(Te <sub>.9</sub> Se <sub>.1</sub> ) <sub>2</sub>	A,B	Virgin	0.30	0.42	0.12	2.4	3.4
		~70°C	0.40	0.53	0.13	-1.6	-2.0
	B	220°C	0.52	0.62	0.10	-3.0	-3.6
Ge(Te <sub>.7</sub> Se <sub>.3</sub> ) <sub>2</sub>	A	~70°C	0.59	0.62	0.03	-6.0	-6.4
		185°C	0.65	0.74	0.10	-13	-16
	B	~70°C	0.58	0.62	0.04	-6.7	-7.2
Ge <sub>15</sub> Te <sub>81</sub> Sb <sub>2</sub> S <sub>2</sub>	A	~70°C	0.31	0.48	0.17	3.6	5.3
		B	~70°C	0.34	0.48	0.14	2.3
	B	~70°C	0.40	0.62	0.22	3.7	5.9
Te <sub>40</sub> As <sub>35</sub> Si <sub>18</sub> Ge <sub>7</sub>	A	~70°C	0.41	0.61	0.20	3.7	6.0
	B	~70°C	0.41	0.61	0.20	3.7	6.0

in Fig. 4.3 and Table 4.1 the materials were amorphous to X-rays. Even though the materials remained amorphous to X-rays during annealing, large changes were observed in the conductivity and thermopower lines. The conductivity activation energies and the  $S$  vs  $1/T$  slopes both increased. It is not certain whether the annealing process involves healing of broken bonds or the formation of an undetectable degree of crystallization, although we favor the bond healing model.

Another  $\text{GeTe}_2$  sample which was partially crystallized with about 1% crystallinity showed a much smaller thermopower (ranging from 0 to 0.5 mV/deg depending on temperature) than the above samples. If there was any crystallinity in the other samples in the  $(\text{GeTe}_2)_x(\text{GeSe}_2)_{1-x}$  system, in any of the annealing states described, it must have been much less than 1%. Of course, crystallization of these materials is possible, but at higher temperatures than discussed here.

The final states of  $\text{As}_2\text{Te}_3$  and  $\text{Ge}_{15}\text{Te}_{81}\text{Sb}_2\text{S}_3$ , as shown in Figs. 4.4 and 4.6, are highly crystallized, as discussed earlier.

#### 4.1.5 Theory of Thermoelectric Effects in Amorphous Semiconductors

Defining  $\zeta_e$  and  $\zeta_h$  as the separations of the Fermi level and the conduction and valence bands, the thermopower for either type of carrier is

$$S_{h,e} = \pm (k/e) [\zeta_{h,e}/kT + A_{h,e}] \quad 4.1$$

where  $A_{h,e}$  is a positive constant. Taking account of the temperature dependence of the band gap, with

$\zeta_{h,e} = \zeta_{ho,eo} - \beta_{h,e} T$ , the two-carrier formula for thermo-power is

$$S = \frac{k}{e} \frac{\sigma_h \left[ \frac{\zeta_{ho}}{kT} - \frac{\beta_h}{k} + A_h \right] - \sigma_e \left[ \frac{\zeta_{eo}}{kT} - \frac{\beta_e}{k} + A_e \right]}{\sigma_h + \sigma_e} \quad 4.2$$

with  $\sigma_h$  and  $\sigma_e$  being the hole and electron contributions to the conductivity. If  $\zeta_{eo} = \zeta_{ho}$ ,  $\beta_e = \beta_h = \frac{1}{2} \beta$ , and  $A_e = A_h = A$ , Eq. 4.2 becomes

$$S = \frac{k}{e} \frac{\sigma_h - \sigma_e}{\sigma_h + \sigma_e} \left[ \frac{\zeta_{ho}}{kT} - \frac{\beta}{2k} + A \right] \quad 4.3$$

for an intrinsic semiconductor.

For crystalline semiconductors,  $A$  is determined by the carrier scattering mechanism, and is usually expected to be between 1 and 4.  $A$  is related to the kinetic energy of transport of the carriers. Little theory exists for amorphous semiconductors, but Hindley<sup>9</sup> gives Eq. 4.3 with  $A = 1$  from the random-phase model.

In Table 4.2 the expressions for  $S$  are summarized for two cases which give linear  $S$  vs  $1/T$  relations: two-carrier intrinsic and one-carrier conduction. If the carrier mobility is independent of temperature  $\Delta E_s$  is related to  $\Delta E_o$  as shown in the third column. We see  $\Delta E_s / \Delta E_o < 1$  due to two-carrier contributions.

TABLE 4.2

S	$\Delta E_s$	$\Delta E_s$	$\Delta E_s$
	For $\mu = \text{constant}$ $\Delta E_s = \zeta_{ho}$	For $\mu = \mu(T)$ $\sim \exp(-\Delta E_\mu/kT)$	For $\mu = \mu(T)$ $\sim \exp(-\Delta E_\mu/kT)$
Two-carrier Intrinsic	$\frac{\sigma_h - \sigma_e}{\sigma_h + \sigma_e} \frac{k}{e} \left[ \frac{\zeta_{ho}}{kT} - \frac{\beta_h}{k} + A \right]$	$\frac{\sigma_h - \sigma_e}{\sigma_h + \sigma_e} \Delta E_o$	$\frac{\sigma_h - \sigma_e}{\sigma_h + \sigma_e} (\Delta E_o - \Delta E_\mu)$
One-carrier holes	$\frac{k}{e} \left[ \frac{\zeta_{ho}}{kT} - \frac{\beta_h}{k} + A \right] = \frac{k}{e} \left[ \frac{\Delta E_s}{kT} - \frac{\beta_h}{k} + A \right]$	$\Delta E_o$	$\Delta E_o - \Delta E_\mu$

$\Delta E_s/e$  = slope of S vs  $1/T$ ,  $\Delta E_o$  = conductivity activation energy

If the mobility is temperature dependent and can be approximated by  $\mu(T) \sim \exp(-\Delta E_\mu/kT)$  over the temperature interval of interest, then the conductivity activation energy contains  $\Delta E_\mu$  as  $\Delta E_s = \zeta_{ho} + \Delta E_\mu$ . Hence, for one-carrier conduction  $\Delta E_s$  is less than  $\Delta E_o$  as  $\Delta E_s = \Delta E_o - \Delta E_\mu$ . Expressions are also given in the final column for  $\Delta E_s$  for two carrier conduction, though these expressions are unlikely since they assume  $\Delta E_\mu$  is the same for both carriers. The two useful expressions relating  $\Delta E_s$  and  $\Delta E_o$  are outlined in bold in the table. In summary,  $\Delta E_s$  can be less than  $\Delta E_o$  for two reasons: 1) two-carrier contributions and 2) a mobility increasing with T.

#### 4.1.6 Discussion of Thermopower Results

The data for lightly annealed  $\text{GeTe}_2$  and  $\text{Ge}(\text{Te}_{.9}\text{Se}_{.1})_2$  agree well with Eqs. 4.3 and with the  $\sigma_h/\sigma_e$  ratios being large. Using  $A = 1$  in Eq. 4.3 gives reasonable values of  $\beta \sim 6$  to  $9 \times 10^{-4}$  eV/deg, or, conversely, assuming  $\beta = 6 \times 10^{-4}$  eV/deg gives small values of  $A \sim 1$ . However, the materials with complex compositions (e.g.  $\text{Ge}_{15}\text{Te}_{81}\text{Sb}_2\text{S}_2$ ) and the virgin (as-sputtered) materials with simpler compositions ( $\text{As}_2\text{Te}_3$  and  $\text{GeTe}_2$ ) give large values of  $A \sim 4.5$  to 8 if  $\beta = 6 \times 10^{-4}$  eV/deg is assumed.

In Table 4.1 on Page 48, several parameters are presented for a number of measurements on virgin and annealed samples.

For each sample,  $A_1 - \beta_h/k$  is calculated from Eq. 4.3 and  $A_2 - \beta_h/k$  is calculated from Eq. 4.1 with  $\zeta_{ho} = \Delta E_s$  for the latter.  $A_1$  and  $A_2$  represent  $A$  calculated in two extremes of temperature-independent and dependent mobilities, respectively (i.e.,  $\Delta E_o - \Delta E_s$  is attributed to two-carrier contributions and a temperature-dependent mobility, respectively). As was noted in the last section,  $A$  is related to the kinetic energy of transport, and its magnitude depends on the nature of scattering. In Fig. 4.7,  $A_2 - \beta_h/k$  and  $A_1 - \beta_h/k$  are plotted vs sample composition and annealing. Both  $A_1 - \beta_h/k$  and  $A_2 - \beta_h/k$  are quite sensitive to  $\Delta E_s$  and  $\Delta E_o$  so that an error of at least  $\pm 2$  should be attached to the  $A$  values in Fig. 4.7. Nevertheless, trends in  $A$  can be discerned. For a given composition  $A$  (either  $A_1$  or  $A_2$ ) apparently decreases with annealing. Also,  $A$  depends upon composition. Generally,  $|A_2| < |A_1|$ .

In summary for the first four materials in Fig. 4.7, it appears that materials with greater disorder give larger values of  $A$ . This disorder includes both compositional disorder as in  $Ge_{15}Te_{81}Sb_2S_2$  and a positional disorder that is reduced by annealing, as in  $GeTe_2$ . Complex compositions such as  $Ge_{15}Te_{81}Sb_2S_2$  maintain a large value of  $A$  even with annealing, whereas simpler compositions such as  $GeTe_2$  give a much reduced  $A$  with only slight annealing, far below the glass transition temperature.

Fig. 4.7

Upper: The parameter  $A_2 - \beta_h/k$  calculated for a variety of materials in various stages of annealment with the assumptions of single-carrier conduction and a temperature-dependent mobility.

Lower: The parameter  $A_1 - \beta_h/k$  calculated with the assumptions of two-carrier conduction and a temperature-independent mobility.

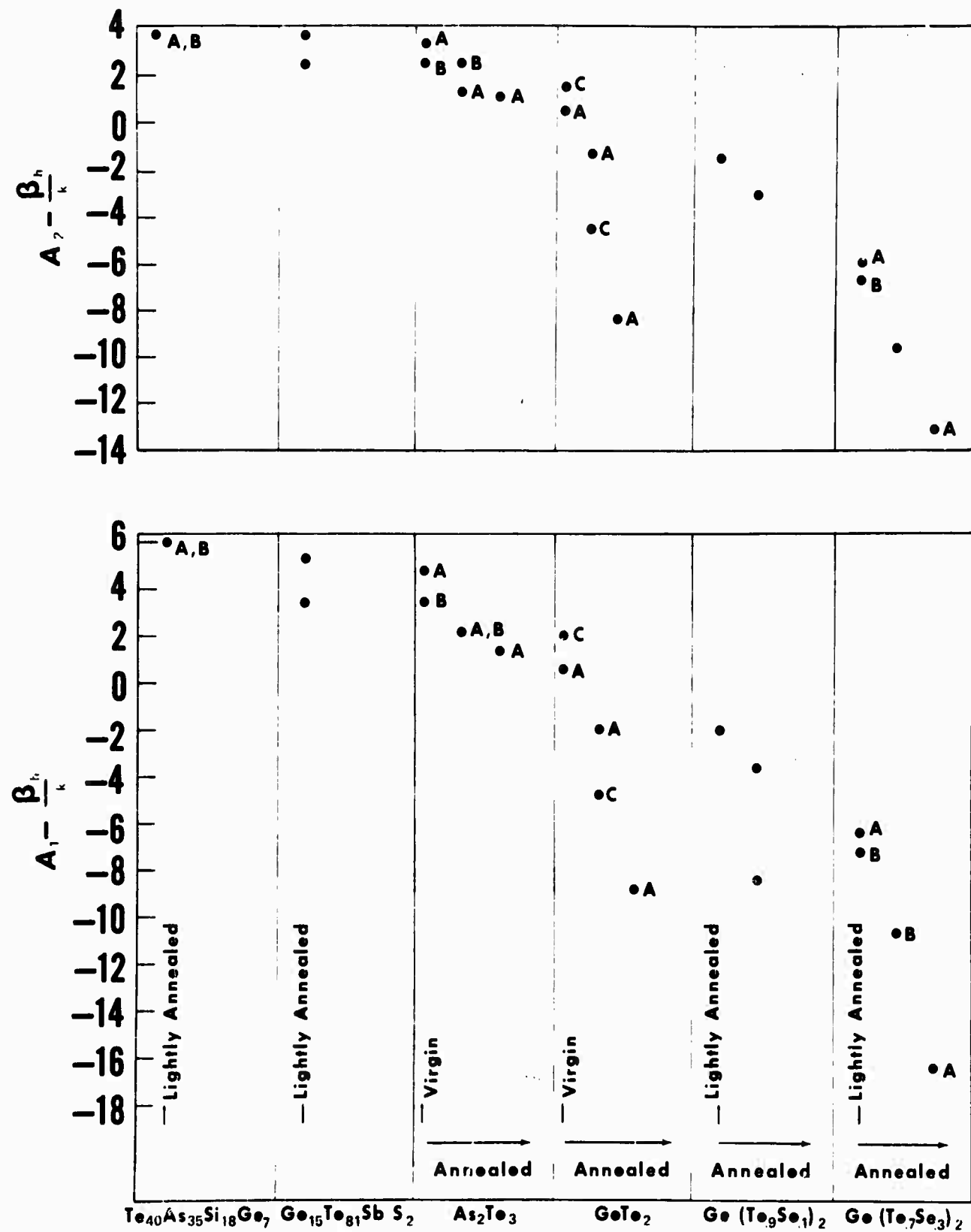


Fig. 4.7

Typical values of  $\beta$  that may be expected are 5 to  $10 \times 10^{-4}$  eV/deg. Some values given in the literature for amorphous chalcogenides, obtained from optical measurements, are:

$\text{As}_2\text{Se}_3$ :	$7 \times 10^{-4}$ eV/deg	Getov et al. <sup>10</sup>
$\text{As}_2\text{Te}_3$ :	$5 \times 10^{-4}$ eV/deg	Weiser and Brodsky <sup>8</sup>
$\text{Te}_{80}\text{Si}_{20}$		
$\text{Te}_{28}\text{As}_{35}\text{Ge}_{16}\text{S}_{21}$	$7 \times 10^{-4}$ eV/deg	Fagen et al. <sup>11</sup>

Taking  $\beta_h = \beta/2 \sim 2.5$  to  $5 \times 10^{-4}$  eV/deg, we may then expect  $\beta_h/k \sim 3$  to 6.

For  $\text{Ge}_{15}\text{Te}_{81}\text{Sb}_2\text{S}_2$ ,  $\text{Te}_{40}\text{As}_{35}\text{Si}_{18}\text{Ge}_7$  and as-sputtered  $\text{As}_2\text{Te}_3\text{A}_2$ ,  $\beta_h/k \sim 3$  and  $A_1 = \beta_h/k \sim 4$  to 6 or  $A_2 \sim 6$  to 9 and  $A_1 \sim 7$  to 12. Both  $A_1$  and  $A_2$  are extremely large, since the largest  $A$  predicted for crystals is 4. Choosing the smaller  $A$ , it seems likely that the mobility is temperature dependent so that  $A \sim A_2 \sim 6$ .

For as-sputtered  $\text{GeTe}_2$ ,  $A_1$  can be 4 to 5 which is plausible so that it is unnecessary to assume a temperature-dependent mobility. However, a temperature-dependent mobility also gives a comparable  $A_2$ . A mixture of the two extreme cases, with a temperature-dependent mobility and contributions from both carriers is a reasonable interpretation, as well.

The decreases of  $A_2 - \beta_h/k$  or  $A_1 - \beta_h/k$  with replacement of Te by Se in the  $\text{Ge}(\text{Te}_x \text{Se}_{1-x})_2$  series is puzzling. In the first place, A should be positive. In the second place, if A does increase with increasing disorder, as suggested earlier, then one expects A to increase as x decreases from 1 to 0.7 because of added compositional disorder. Both  $A_1$  and  $A_2$  are negative for annealed  $\text{Ge}(\text{Te}_{.7} \text{Se}_{.3})_2$  unless  $\beta_h$  is extremely large.  $\beta_h \sim 7.5 \times 10^{-4}$  eV/deg would give  $A_1$  and  $A_2 = 1$  for lightly-annealed  $\text{Ge}(\text{Te}_{.7} \text{Se}_{.3})_2$ , but an even larger  $\beta_h$  is required to explain the heavily annealed data.

A large  $\beta_h$  could result from a large  $\beta = \beta_e + \beta_h$ , or it could result from an ordinary magnitude of  $\beta$  but with the Fermi-level position being a strong function of temperature. It is conceivable that the density of localized states spectrum in this system is such that the Fermi-level position relative to the center of the band gap is a strong function of temperature. Also, the increase of energy gap with decreasing x may imply a corresponding increase in  $\beta$ .

Finally, for the last two materials in Fig. 4.3, agreement with the conventional model is only made more difficult by the introduction of  $u = \mu(T)$ .

Further work will be necessary before we understand the large but temperature independent S in Fig. 4.4 when the

conductivity shows extrinsic behavior. It is of interest, however, that degenerate conduction with an  $A \sim 5$  to 6.5 could account for  $S \sim 0.4$  to 0.55 mV/deg independent of  $T$ .

#### 4.1.7 Thermocconductivity

Apparatus has been built to measure the thermocconductivity  $\kappa$  of bulk materials directly in the steady state as a function of temperature, from room temperature to  $170^\circ C$ . With minor changes, the range can be extended to  $-40^\circ$  to  $200^\circ C$ .

The following data have been obtained:

	T	$\kappa$ (mW/cm-deg)
$As_2S_3$	$33^\circ C$	$3.2 \pm .1$
$Ge_{16}As_{35}Te_{28}S_{21}$	$35^\circ C$	$2.3 \pm .1$
$Te_{40}As_{35}Si_{18}Ge_7$	$35^\circ C$	$3.0 \pm .1$
	$88^\circ C$	$3.9 \pm .1$
$Ge_{15}Te_{81}Sb_2S_2$	$31^\circ C$	$2.0 \pm .1$

To date we have focused our attention on Seebeck coefficient measurements, and have not made detailed thermal conductivity measurements.

#### 4.1.8 Thermoelectric Figure of Merit

Since the figure of merit  $Z$  is given by  $S^2\sigma/\kappa$ , it is necessary to know  $S$ ,  $\sigma$ , and  $\kappa$  as a function of  $T$  to give  $Z(T)$ . However, we can assume that  $\kappa$  does not vary

drastically from one amorphous chalcogenide to another, and estimate  $Z$  without measurements of  $\kappa$ . In Fig. 4.8  $Z \cdot \kappa / (3 \times 10^{-3}$  watt/cm deg) is plotted vs  $1/T$  for several materials. Since  $\kappa$  increases with increasing  $T$  by  $\sim 2x$  from  $300^\circ$  to  $400^\circ$  K (e.g. the  $\kappa$  data above and published data for  $\text{As}_2\text{S}_3$ ),<sup>29</sup> the  $Z$  curves should be slightly (but only slightly) flatter than the curves of Fig. 4.8.

As expected, for a given material,  $Z$  increases exponentially with  $(-1/T)$  because  $Z(T)$  is determined primarily by  $\sigma(T)$ . Also, smaller band gap materials give a larger  $Z$  at a given  $T$  than do large gap materials. Although  $S^2$  increases as the gap increases,  $\sigma$  decreases exponentially, since  $\sigma = \sigma_0 \exp(-\Delta E_0/kT)$  and  $\sigma_0$  is roughly the same for the various materials. Nevertheless, in a given temperature range the smallest band gap materials may not be the most desirable. For example, below  $100^\circ$  C,  $\text{As}_2\text{Te}_3$  has the highest  $Z$  shown. Near  $200^\circ$  C, amorphous  $\text{As}_2\text{Te}_3$  is not stable, so that annealed  $\text{GeTe}_2$  has a higher  $Z$  at that temperature.

The highest estimated figure of merit for the various materials we have studied to date is  $10^{-6}$  deg<sup>-1</sup>, which is two to three decades less than that obtained for crystalline materials such as  $\text{InAs}_{0.9}\text{P}_{0.1}$ .<sup>13</sup> Since the electrical conductivity is the dominate variable in  $Z$ , the problem of obtaining a large  $Z$  is

Fig. 4.8

Temperature dependence of  $Z \cdot \alpha / (3 \times 10^{-3}$  Watt/cm deg) for various amorphous chalcogenide films. This quantity approximates the thermoelectric figure of merit Z to the extent that the thermoconductivity is near  $3 \times 10^{-3}$  Watt/cm deg.

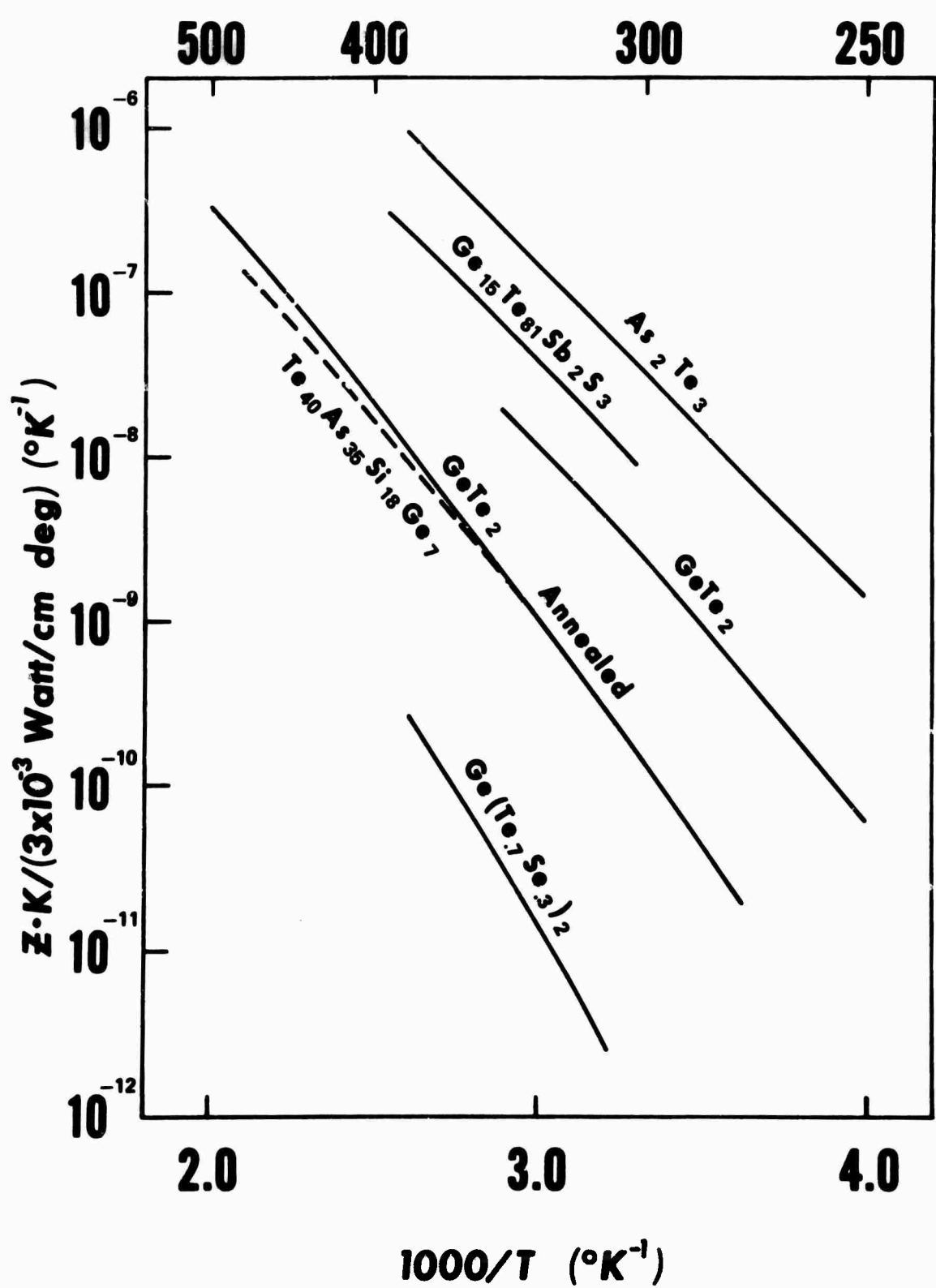


Fig. 4.8

one of optimizing a small band gap with stability of the amorphous state at high temperature. We anticipate that improvements in  $Z$  can be obtained in other materials.

#### 4.1.9 Further Experimentation

In addition to continuing measurements of the Seebeck coefficient, thermal conductivity will be measured in more detail.  $Z(T)$  will be extended. Also the temperature dependence of the gap,  $\beta$ , will be determined for more materials by optical measurements, for possible correlation with the thermoelectric analysis.

#### 4.2 Photoconductivity

The measurements of photoconductive response in amorphous chalcogenide alloy films, whose generic properties were described in the first Semiannual Technical Report to this contract, were undertaken initially in order to elucidate the band structure of this family of materials, presently a matter of some controversy. Despite the establishment of certain broad regularities and similarities of behavior, it had not been possible to extract from the experimental data quantitative information regarding the equilibrium density-of-states function or the dynamics of trapping and recombination, owing to the lack of a suitable conceptual model on which to base mathematical analysis. It now appears that a successful model can be constructed and made to yield (albeit in a somewhat oblique manner) numerical estimates for both the total density of states and a number of important transport parameters. The essential feature of this model is a high density of effective recombination states located within an energy  $E^*$  from each band edge, the energy  $E^*$  lying in the range 0.1 to 0.3 eV for several common chalcogenide alloys. A paper describing the model will be presented jointly with Professor R. Bube and Mr. T. Arnoldussen of Stanford University at the Fourth International Conference on Amorphous and Liquid Semiconductors at the University of Michigan in August 1971.

The necessity to guide development of the model at each stage by direct comparison with experiment has in turn provoked renewed laboratory effort in the refinement and extension of measurements. In particular, the properties of the prototypical memory alloy  $Ge_{15}Te_{81}Sb_2S_2$  have been measured over a much wider range of photocurrents and excitation intensities than hitherto reported, with results shown in Fig. 4.9. The characteristic features of this family of curves are a high temperature region in which the photocurrent increases exponentially with reciprocal temperature and is substantially linear with intensity, a low temperature region in which the photocurrent decreases exponentially with reciprocal temperature and becomes sublinear with intensity at high intensities, and a very low temperature region in which the photocurrent asymptotically approaches temperature independence and is again substantially linear in intensity. Additionally, the temperature of maximum photocurrent is independent of intensity at low intensities, but proportional to the logarithm of intensity at high intensities. All these features are satisfactorily explained by the proposed model. Note that the steady state photocurrent contains only two temperature dependent factors, the drift mobility and the lifetime of excited carriers. Thus the existence of maxima in Fig. 4.9 implies either a maximum in the lifetime or opposing thermally activated temperature dependences for the lifetime and the

Fig. 4.9

Equilibrium dark conductivity and steady-state photoconductivity of sputtered thin film ( $1.1 \mu\text{m}$  thickness) of  $\text{Ge}_{15}\text{Te}_{81}\text{Sb}_2\text{S}_2$  alloy, with coplanar molybdenum electrodes. The uppermost photoconductivity curve corresponds to illumination with approximately  $1.4 \times 10^{17}$  photons/ $\text{cm}^2\text{-sec}$  of narrow-band ( $\Delta\lambda/\lambda_0 \approx 0.4$ ) light, centered about  $\lambda_0 = 1.06 \mu\text{m}$ ; below this the intensity decreases in decade steps. Photoconductivity curves are interrupted below the dotted contour, a region in which the steady state is not attained because of instrumental limitations.

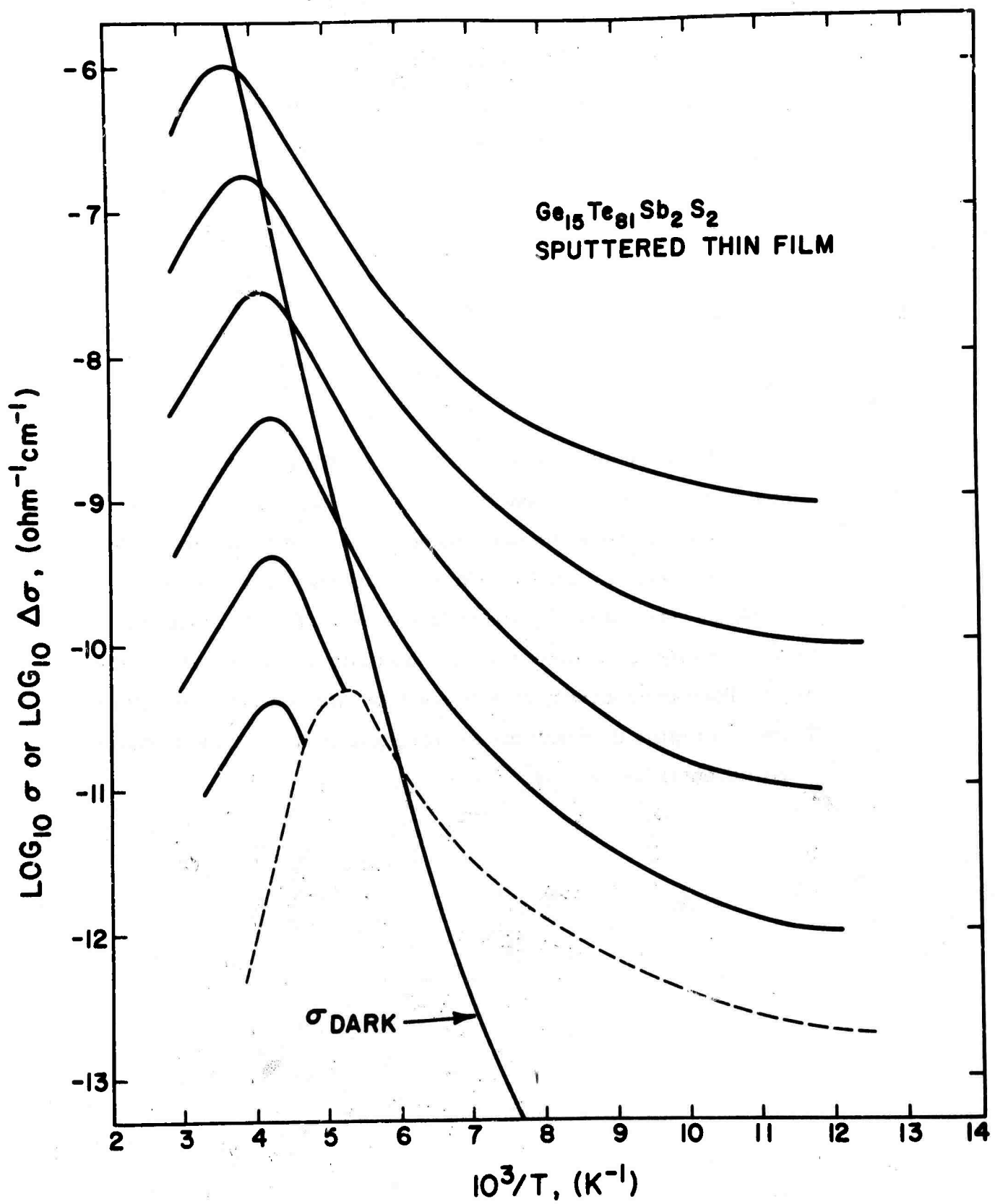


Fig. 4.9

mobility. (The maximum cannot occur in the mobility alone, for there is no corresponding anomaly in the electrical conductivity.) Therefore the task of analysis may be viewed as essentially that of decomposing the curves of Fig. 4.9 into lifetime and mobility contributions. In this instance we lack the assistance of independent measurements of the mobility. We can, however, profitably correlate our data with those derived from measurements of thermoelectric power and thermally stimulated conductivity currently in progress. A detailed account of these investigations, together with refined numerical estimates for various transport parameters, will appear in forthcoming publications.

#### 4.3 Switching Measurements

##### 4.3.1 Introduction

A survey type evaluation of switching characteristics was made on a large number of compositions in order to classify them as to their memory or threshold behavior. Measurements were also made on the "first fire" characteristics, threshold voltage as a function of thickness and composition, and threshold and memory switching as a function of temperature.

##### 4.3.2 Experimental Methods

To provide the necessary pulses, a four pulse generator was designed and constructed which provided pulses with independently adjustable temporal spacing, widths, rise and fall times, and amplitudes. The arrangement is a master timing unit controlling three pulse amplifiers and conditioners. The amplifiers are diode coupled through independently adjustable series load resistors to the sample. For measurements of memory switching, a pulse train shown in Fig. 4.10 was applied to the specimen. The voltage measured across a device undergoing switching is shown in Fig. 4.11

Referring to Fig. 4.10, pulse A is the "set" pulse; pulses B and D, the "read" pulses; and pulse C is the reset pulse. The pulse height of the set pulse is chosen so as to exceed the threshold voltage of the device. The series load

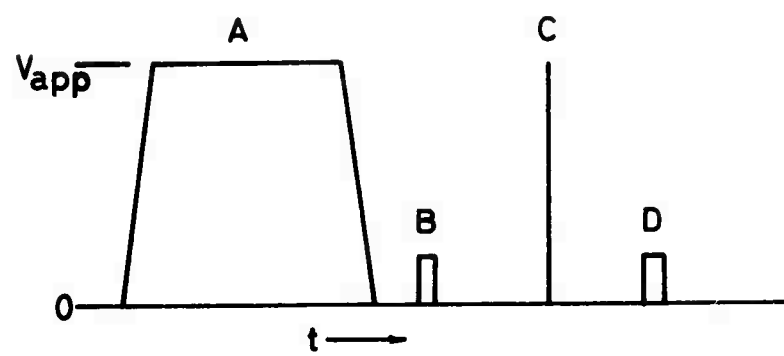


Fig. 4.10 Pulse Train

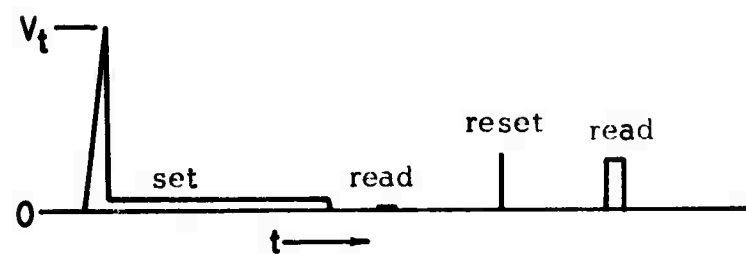


Fig. 4.11 Voltage Across OMS Device

resistor coupling the set pulse to the device is chosen to limit the "set" current delivered to the device after switching e.g. a 50 V set pulse amplitude and a series resistor of 10 K ohms would deliver a set current of 5 mA. The standard pulse shape has a rise and fall of 2 msec and a total duration of 17 msec.

The reset pulse is uniform for all measurements and is a current pulse of 150 mA in amplitude and 6  $\mu$ sec. wide.

The read pulses are low voltage pulses 2 to 5 V, two milliseconds wide interposed between the set and reset pulses, and following the reset pulse. Its purpose is to determine the state of the device - set or reset. It is coupled through a high value series load resistor, approximately 100 K ohms, so that in a low impedance state its amplitude would be severely diminished but in an off or reset state its amplitude would be virtually unaffected as shown in Fig. 4.11.

The values of the threshold voltage were determined by displaying the characteristics shown in Fig. 4.11 on a memory oscilloscope and by using a peak reading memory voltmeter in conjunction with a fast, strip chart recorder.

The resistance values of the specimens were determined by measuring the voltage drop across the devices when passing

$10^{-10}$  amperes through the device. This method reduces the probability of disturbing the state of the sample during the measurement.

The preferred sample configuration would be a sandwich type where the amorphous layer is disposed between two parallel conducting electrodes. Because of the large number of compositions to be evaluated, the sample configuration was impractical and a "probe" technique was utilized. This technique consists of depositing the material of interest on a previously metallized substrate, the metal layer, molybdenum in all cases, serving as one electrode. The other electrode was a tungsten probe with a two micron radius tip which was gently lowered into contact with the amorphous layer with a micromanipulator. The switching voltage was then applied between the probe and metal layer. The polarity of the probe was positive with respect to the metal layer. This technique was proven to give results similar to sandwich configurations by employing a material which had been well characterized using sandwich samples and comparing the results to those obtained by the probe technique. The probe technique also offers the advantage of more measurements per sample since a one square centimeter sample has hundreds of measurement sites; thereby allowing one to obtain a good statistical average of results.

OTS switching and OMS switching are distinguished by what happens after the "on" state is reached by exceeding the threshold voltage. OTS materials return from the "on" state to the "off" state as soon as the current falls below a certain current holding value. OMS materials remain in the "on" state as a result of the power dissipation during the setting action. The OMS devices thus require a reset pulse under normal operating conditions to return to the "off" state. The effectiveness of the reset pulse in resetting the device determines the reset "off" resistance and the threshold voltage for the next operating cycle.

The OMS devices can, however, be operated in a transient switching (TS) mode. Here the switching pulse is kept sufficiently short so that the OMS device is not set in the "on" state but returns to the "off" state at the end of the switching pulse.

For proper evaluation, it proved useful to subject each material to a TS (transient switching) and an OMS (memory switching) test pulse train.

Transient switching was achieved by means of a current sensor and electronic "crowbar" circuit. The combination of current sensor and crowbar circuit is referred to as the zero power tester (ZPT). When the current through the device exceeded

the level set on the current sensor, adjustable from 0.25 mA to 5 mA, it tripped the crowbar circuit thereby shunting the current from the device and preventing any significant setting action. For all TS measurements, the ZPT was set to trip at 0.5 mA and would reduce the voltage across the device to approximately 0.65 volts within 50 nsec after the threshold switching action.

#### 4.3.3 Results

##### 4.3.3.1 Switching at 298° K

A thorough investigation of threshold voltage as a function of thickness was made on the composition  $\text{Te}_{81}\text{Ge}_{15}\text{Sb}_2\text{S}_2$ , which is a typical OMS material. Several hundred devices were prepared in a sandwich configuration with sputtered Mo electrodes and an active glass area twenty microns in diameter. The thickness was varied from  $0.5 \mu$  to  $1.6 \mu$ .

The results are presented in Table 4.2 for TS operation and in Table 4.3 for OMS operation.

The resistance and geometry of virgin films gives a resistivity at 298 K of  $\rho = (1.15 \pm 0.15) \times 10^5$  ohm-cm. The virgin resistance is shown as a function of film thickness in Fig. 4.12.

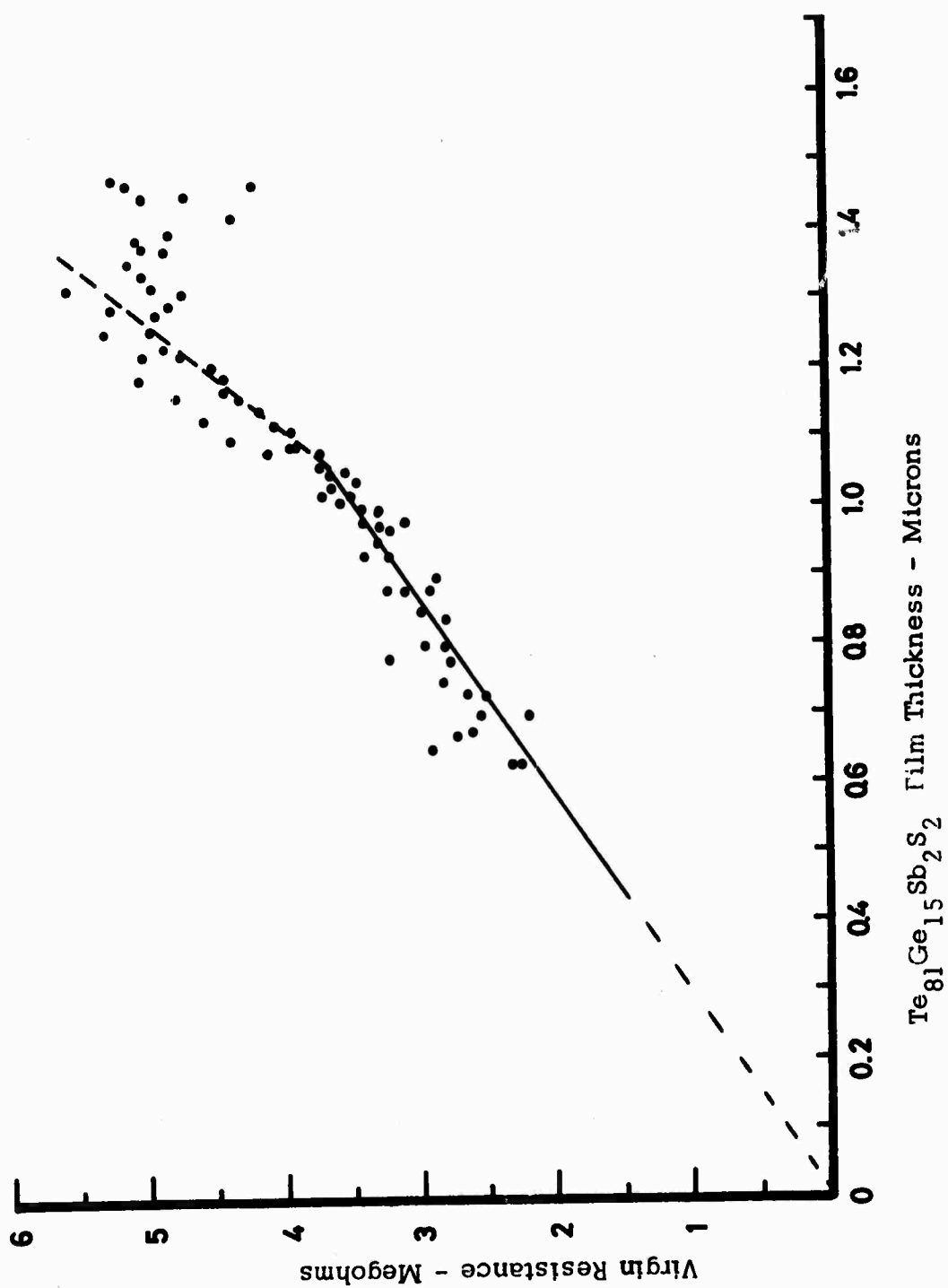


Fig. 4.12

TABLE 4.2 TS OPERATION

Device No.	Thickness (microns)	Virgin Resistance ( $10^6$ ohms)	First Fire Voltage	Off State Resistance ( $10^6$ ohms)	Average Threshold Voltage
4	0.63	2.29	25.2	1.70	12.5
6	0.675	2.70	26.0	1.90	12.9
8	0.73	2.50	27.0	1.81	12.2
10	0.78	2.75	28.2	1.90	12.8
12	0.83	2.86	28.8	2.00	13.1
14	0.88	2.90	29.6	1.90	12.2
16	0.93	3.21	31.0	2.10	14.5
18	0.97	3.22	31.2	2.10	14.5
20	1.00	3.30	32.2	2.10	15.0
22	1.02	3.50	33.0	2.20	14.5
24	1.04	3.52	34.0	2.21	14.5
26	1.06	3.60	34.5	2.20	15.8
28	1.08	3.71	35.2	2.22	15.9
30	1.09	3.89	35.8	2.37	16.2
32	1.11	3.90	36.8	2.30	16.0
34	1.12	4.05	37.2	2.32	16.2
36	1.14	4.15	33.0	2.38	16.8
38	1.15	4.30	38.5	2.40	16.2
40	1.17	4.40	39.0	2.48	16.8
42	1.18	4.42	39.2	2.56	16.9
44	1.20	4.49	40.2	2.50	17.2

TABLE 4.2 (cont'd.)

Device No.	Thickness (microns)	Virgin Resistance ( $10^6$ ohms)	First Fire Voltage	Off State Resistance ( $10^6$ ohms)	Average Threshold Voltage
46	1.22	4.76	40.8	2.52	17.2
48	1.23	4.85	41.0	2.60	17.1
50	1.25	5.30	41.6	2.74	17.7
52	1.26	4.95	42.0	2.61	17.8
54	1.28	4.90	42.5	2.68	17.8
56	1.29	4.82	42.6	2.58	17.8
58	1.31	4.71	43.0	2.55	18.1
60	1.32	4.94	43.2	2.70	18.1
62	1.34	5.00	43.9	2.77	18.1
64	1.36	5.11	43.9	2.86	18.1
66	1.37	4.86	44.1	2.70	18.1
68	1.39	5.04	44.2	2.75	18.5
70	1.4	4.80	44.8	2.68	18.1
76	1.45	4.50	44.9	2.59	18.5
78	1.47	5.13	45.1	2.74	18.5
80	1.48	5.20	45.1	2.90	18.5

TABLE 4.3 OMS OPERATION

Device No.	Thickness (microns)	First Fire Voltage	Reset Res. (ohms x 10 <sup>6</sup> )	Device No.	Thickness (microns)	First Fire Voltage	Reset Res. (ohms x 10 <sup>6</sup> )
4	0.63	27	1.50	17	0.95	33	1.88
5	0.65	27	1.80	18	0.97	33	1.92
6	0.68	28	1.60	19	0.98	34	1.91
7	0.70	28	1.56	20	1.00	34	1.95
8	0.73	29	1.61	21	1.01	34	1.92
9	0.75	29	1.62	22	1.02	35	1.98
0	0.78	30	1.80	23	1.03	--	--
1	0.80	30	1.70	24	1.04	35	2.07
2	0.83	--	--	25	1.05	36	2.00
3	0.85	31	1.72	26	1.06	36	2.00
4	0.88	31	1.81	27	1.07	37	2.00
5	0.90	31	1.87	28	1.08	37	2.10
6	0.93	32	1.90	29	1.08	37	2.01
				30	1.09	38	2.01

These samples all exhibited a first fire effect, i.e. the threshold voltage on the first firing of the virgin sample was higher than any subsequent firing and is not again observed after any treatment of the device. The first fire voltage as functions of film thickness is shown in Fig. 4.13 and virgin resistance in Fig. 4.14. The variation in running threshold, i.e. the average threshold voltage after first fire, is shown in Fig. 4.15 for both the TS and OMS operational modes.

The variation of TS threshold voltage with thickness for a number of compositions is shown in Fig. 4.16. These were obtained by the probe method.

A summary of the results for the alloys investigated is given in Table 4.4. All were probe tested at 298° K. Column 1 is the alloy; 2, the thickness in microns; 3 and 4 the resistance in ohms of the sample before (virgin) and after twenty TS firings; 5, the ratio of 3 and 4; 6, the first fire voltage; 7, the running ZPT-TS threshold voltage; and 8, the threshold voltage,  $V_{PT}$ , measured on the set pulse of the pulse train shown in Fig. 4.11. OTS materials switch off on the trailing edge of the set pulse and do not generally switch on again until the succeeding set pulse. Each entry is the average of twenty switching points which have each switched twenty times in either the Pulse-Train (PT) or transient switching (TS) mode.

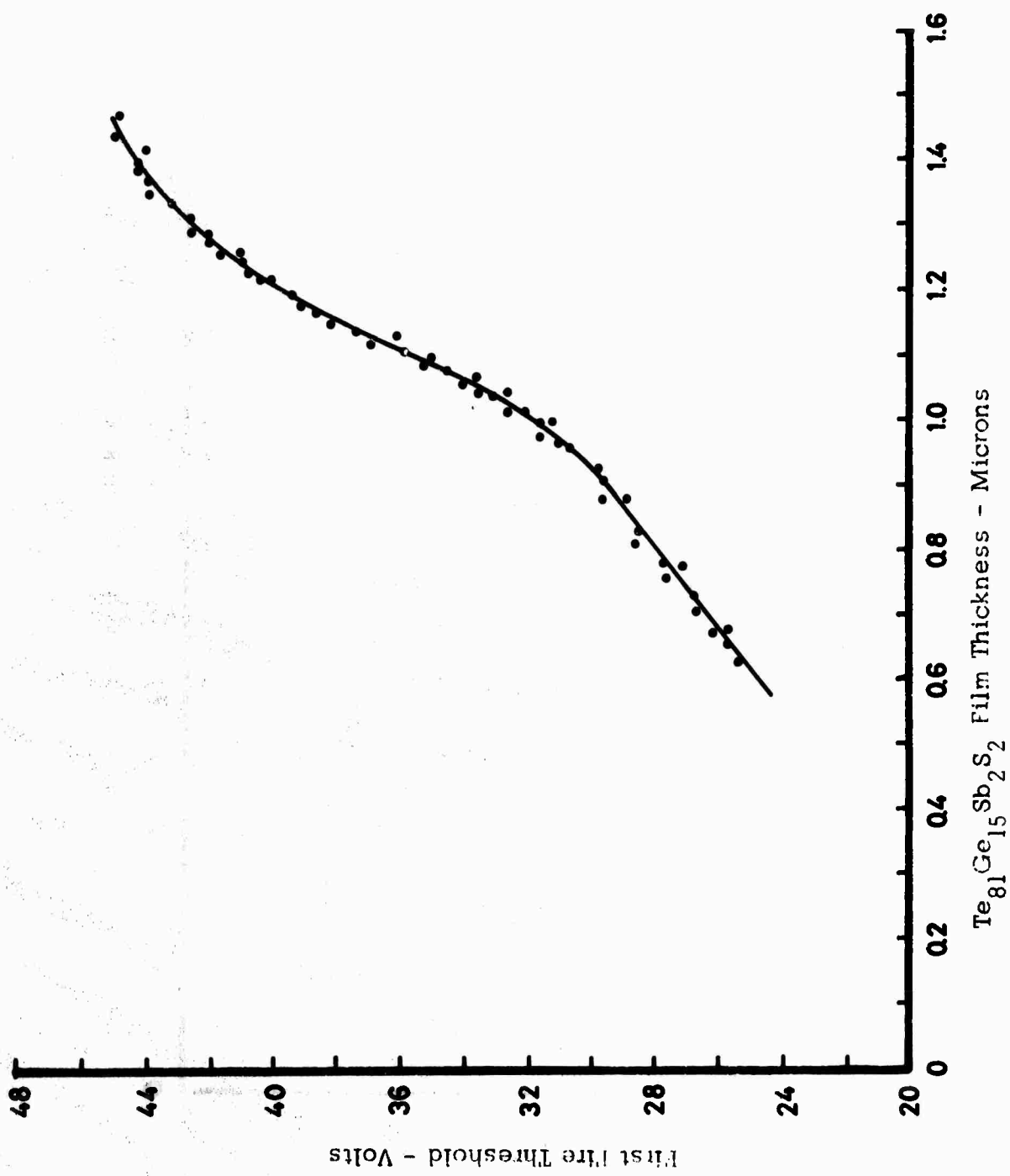


Fig. 4.13

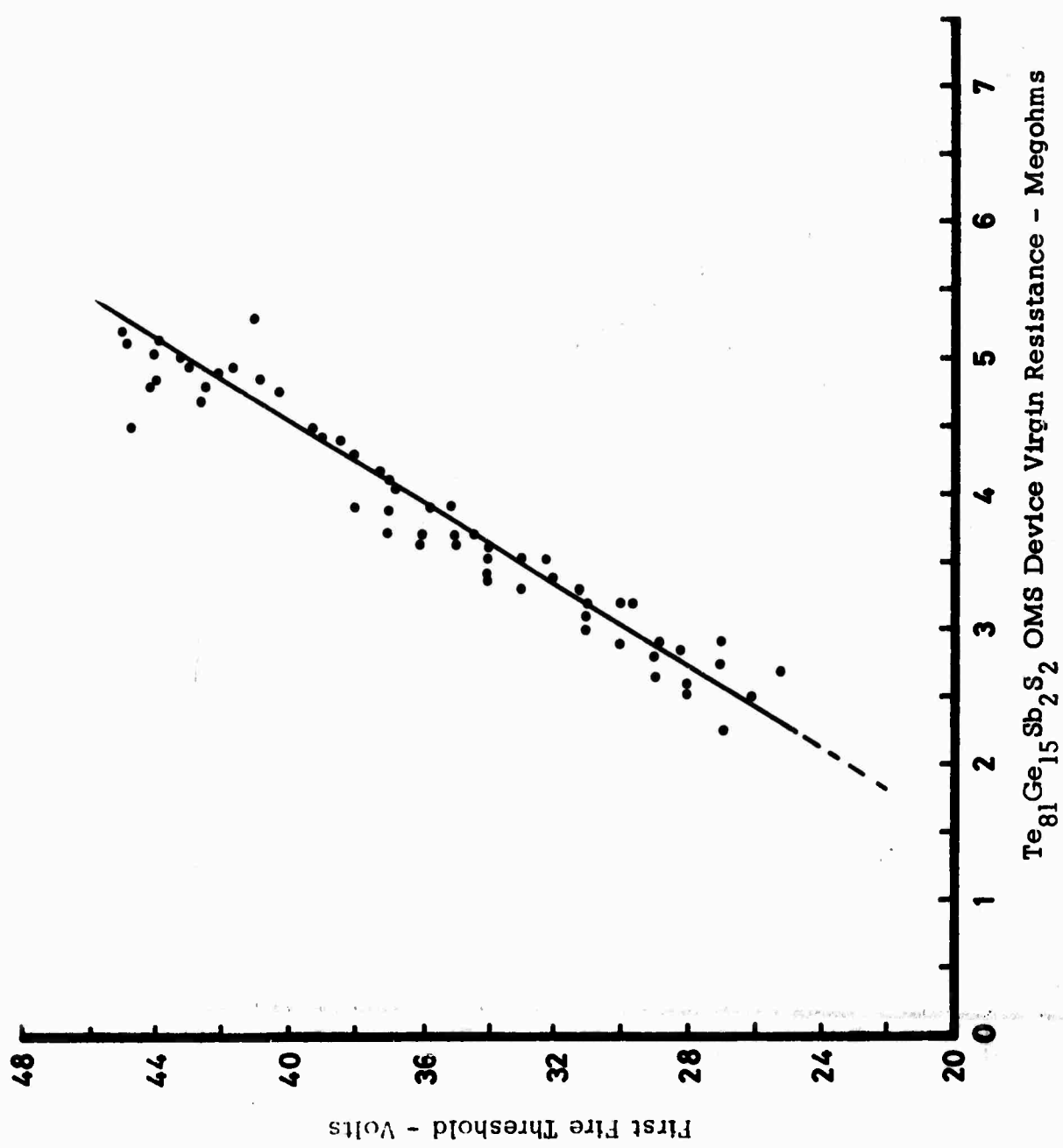


Fig. 4.14

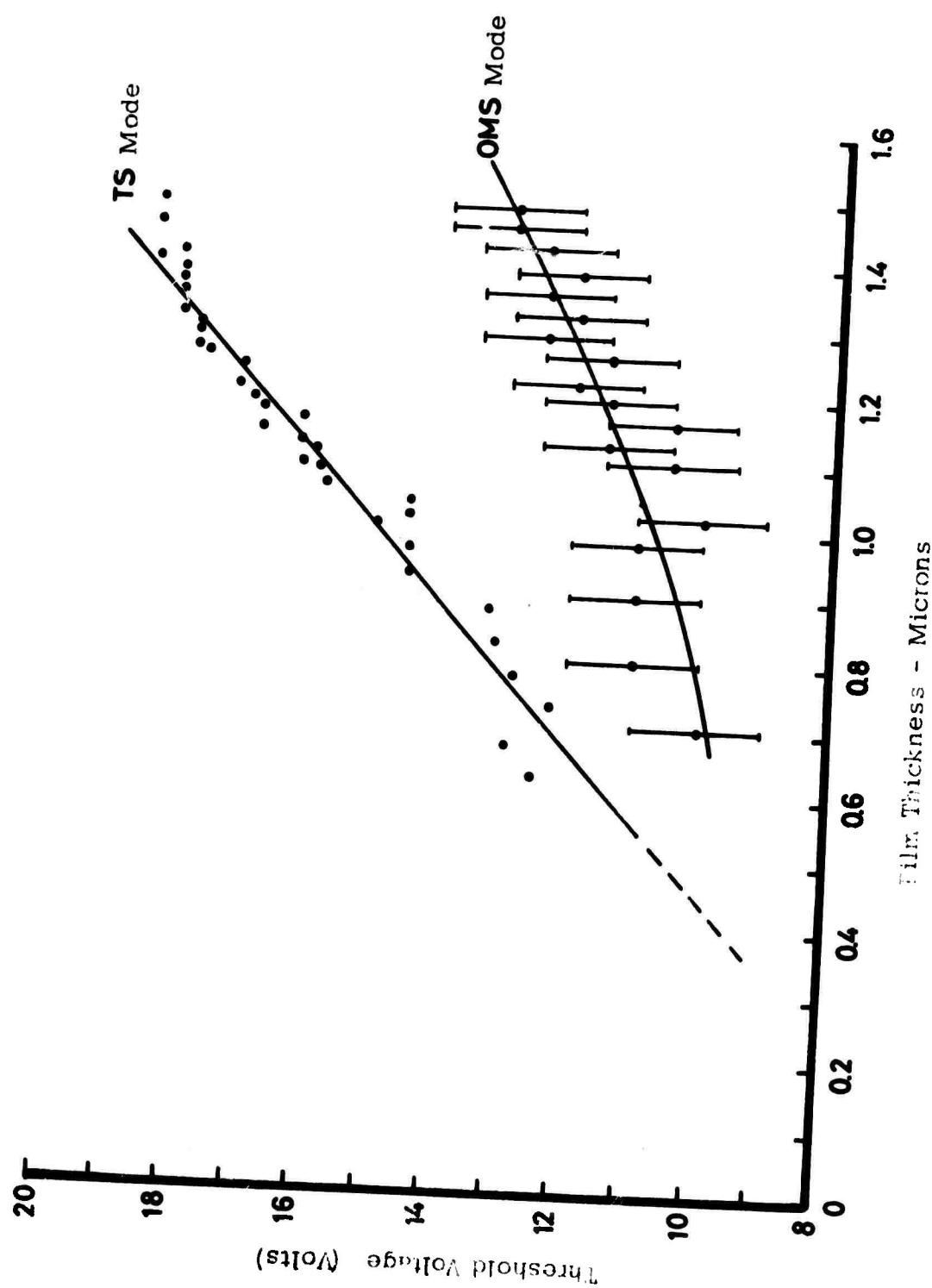


Fig. 4.15

**Fig. 4.16**

**Threshold voltage in TS switching mode vs thickness for films listed in Table 4.4. Compositions are identified by last 2 digits of numbers tabulated in Composition Index of Table 4.4.**

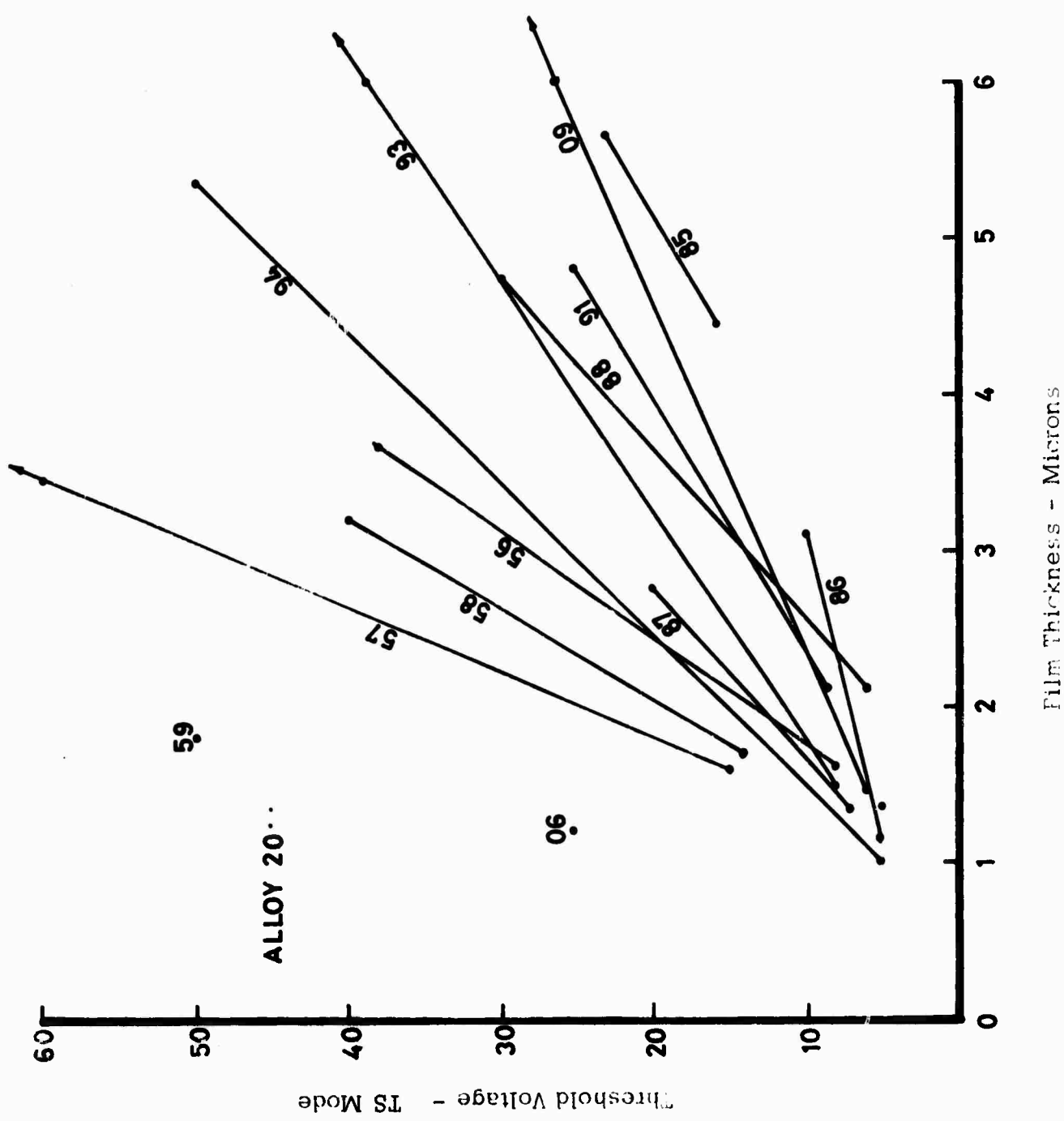


Fig. 4.16

TABLE 4.4

1	2	3	4	5	6	7	8
OTS							
		$R_1$	$R_2$	$R_1/R_2$	$V_{ff}$	$V_{OTS}$	$V_{PT}$
	Thickness	before	after				
2057	4.3	$10^8$	$5 \times 10^7$	2	80	80	75
2057	1.6	$2 \times 10^7$	$5 \times 10^6$	4	25	15	25
2058	1.7	$10^7$	$4 \times 10^6$	2.5	25	14	18
2058	3.18	$5 \times 10^7$	$2 \times 10^7$	2.5	60	40	50
2055	1.35	$7 \times 10^5$	$3 \times 10^5$	2.2	8	4	10
2056	3.66	$3 \times 10^7$	$10^7$	3	45	38	40
2056	1.62	$3 \times 10^6$	$10^6$	3	13	8	12
2059	1.8 $\mu$	$9 \times 10^8$	$4 \times 10^8$	2.2	60	50	set
2060	Very unstable resistance and threshold voltage						
2061							
2009	1.45	$6 \times 10^5$	$2 \times 10^5$	3	8	6	9
2009	7.78	$10^7$	$6 \times 10^6$	1.7	60	33	40
2008	1.33	$2 \times 10^7$	$2 \times 10^5$	10	21	11	18
2007	1.65	$4 \times 10^7$	$4 \times 10^6$	10	25	15	20
2006	1.2	$10^9$	$10^8$	10	38	25	25
2005	.74	generally unstable					
2085	5.66	$2.9 \times 10^6$	$2 \times 10^6$	1.45	28	23	23
2085	4.45	$4 \times 10^6$	$2 \times 10^6$	2	25	16	22
2087	1.42	$3 \times 10^6$	$5 \times 10^5$	6	15	7	12
2087	2.74	$2 \times 10^8$	$7 \times 10^6$	30	50	20	12
2086	1.12	$8 \times 10^5$	$1.5 \times 10^5$	4.5	10	5	10
2086	3.10	$6 \times 10^6$	$7 \times 10^5$	9	30	10	20
2088	2.12	$7 \times 10^5$	$4 \times 10^5$	1.8	10	6	9
2088	4.72	$10^7$	$7 \times 10^6$	1.4	50	30	40
2089		$5 \times 10^7$	$1.5 \times 10^7$	3	70	50	unstable
2090		$6 \times 10^7$	$6 \times 10^7$	4	60	40	30
2091	2.12	$2 \times 10^6$	$10^8$	2	15	9	15
2091	4.81	$6 \times 10^6$	$3 \times 10^6$	2	38	25	30
2092		$1.5 \times 10^6$	$7 \times 10^5$	2	13	9	12
2092		$1.5 \times 10^7$	$7 \times 10^6$	2	60	30	36
2093	1.48	$1.8 \times 10^6$	$8 \times 10^5$	2.2	12	8	12
2093	7.67	$1.9 \times 10^7$	$1.2 \times 10^7$	1.7	65	50	50
2094	5.37	$3 \times 10^7$	$2 \times 10^7$	1.5	80	50	55
2094	1.06	$1.3 \times 10^6$	$4 \times 10^5$	3.2	10	5	12

\* OTS material - switched off on trailing edge of the set pulse;  $V_{PT}$  is the threshold voltage measured on subsequent set pulse.

+ OMS material

TABLE 4.4 - Cont'd.  
Composition Index

Composition Number	S	Se	Te	As	Si	Ge
2005		33.33	30	20		16.66
2006		26.66	36	24		13.33
2007		20	42	28		10
2008		13.33	48	32		6.66
2009		6.66	54	36		3.33
2055	6		54	40		
2056	12		48	40		
2057	18		42	40		
2058	24		36	40		
2059	30		30	40		
2060	36		24	40		
2061	42		18	40		
2085		60.33		38	1.66	
2086		60.66		36	3.33	
2087		61		34	5	
2088		61.33		32	6.66	
2089		61.66		30	8.33	
2090		60.66		36	3.33	3.33
2091		61.33		32	6.66	6.66
2092		62		28	10	10
2093		62.66		24	13.33	13.33
2094		63.33		20	16.66	16.66

#### 4.3.3.2 Switching Characteristics at Elevated Temperatures

Switching characteristics at temperatures above 298° K were investigated for two compositions;  $\text{Te}_{81}\text{Ge}_{15}\text{Sb}_2\text{S}_2$  and  $\text{Te}_{40}\text{Ge}_7\text{As}_{35}\text{Si}_{18}$ . The first is a good OMS alloy and the second a good OTS alloy. We report here probe measurements made with sample and probe immersed in silicone oil. All TS measurements were made using the zero power tester and the OMS measurements used the standard set and reset pulses.

The variation of TS first fire and running threshold (at 1 c.p.s.) are shown in Fig. 4.17 for the composition  $\text{Te}_{81}\text{Ge}_{15}\text{Sb}_2\text{S}_2$ . The running threshold for OMS operation (at  $\sim 0.05$  c.p.s.) is given in Fig. 4.18. The OMS mode could be sustained as high as 150° C with a 10 c.p.s. rate. At lower set-reset rates there was appreciable thermal setting resulting in depressed threshold voltages. We calculate a crystallization rate of order  $10^{-3} \text{ cm sec}^{-1}$  at 150° C from these observations.

The variation of OTS first fire and running threshold voltages for the composition  $\text{Te}_{40}\text{Ge}_7\text{As}_{35}\text{Si}_{18}$  with temperature is given in Fig. 4.19.

#### 4.3.4 Discussion of Switching Materials Survey

Pending further measurements of a detailed nature, a few comments may be offered to summarize the work to date.

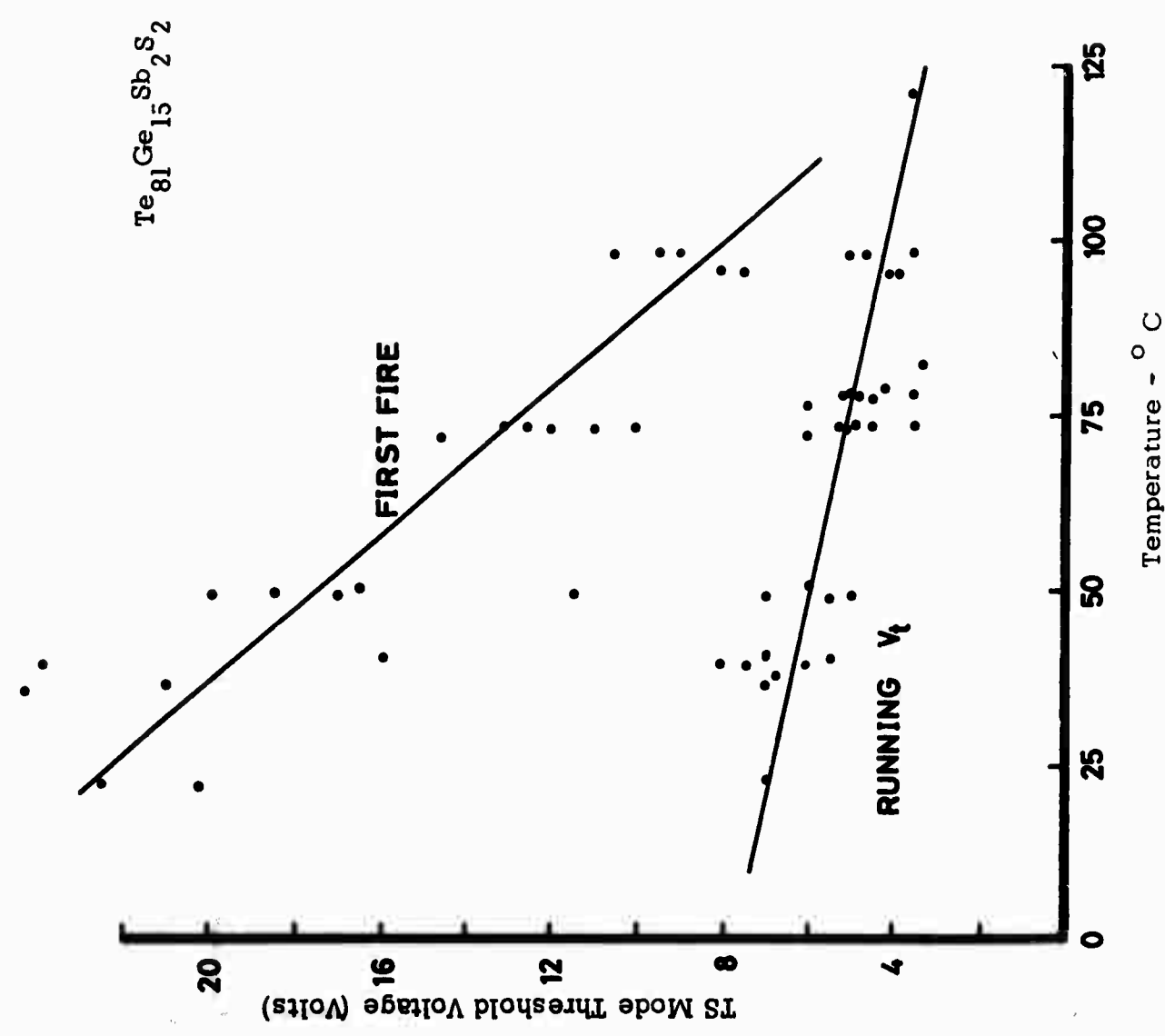


Fig. 4.17

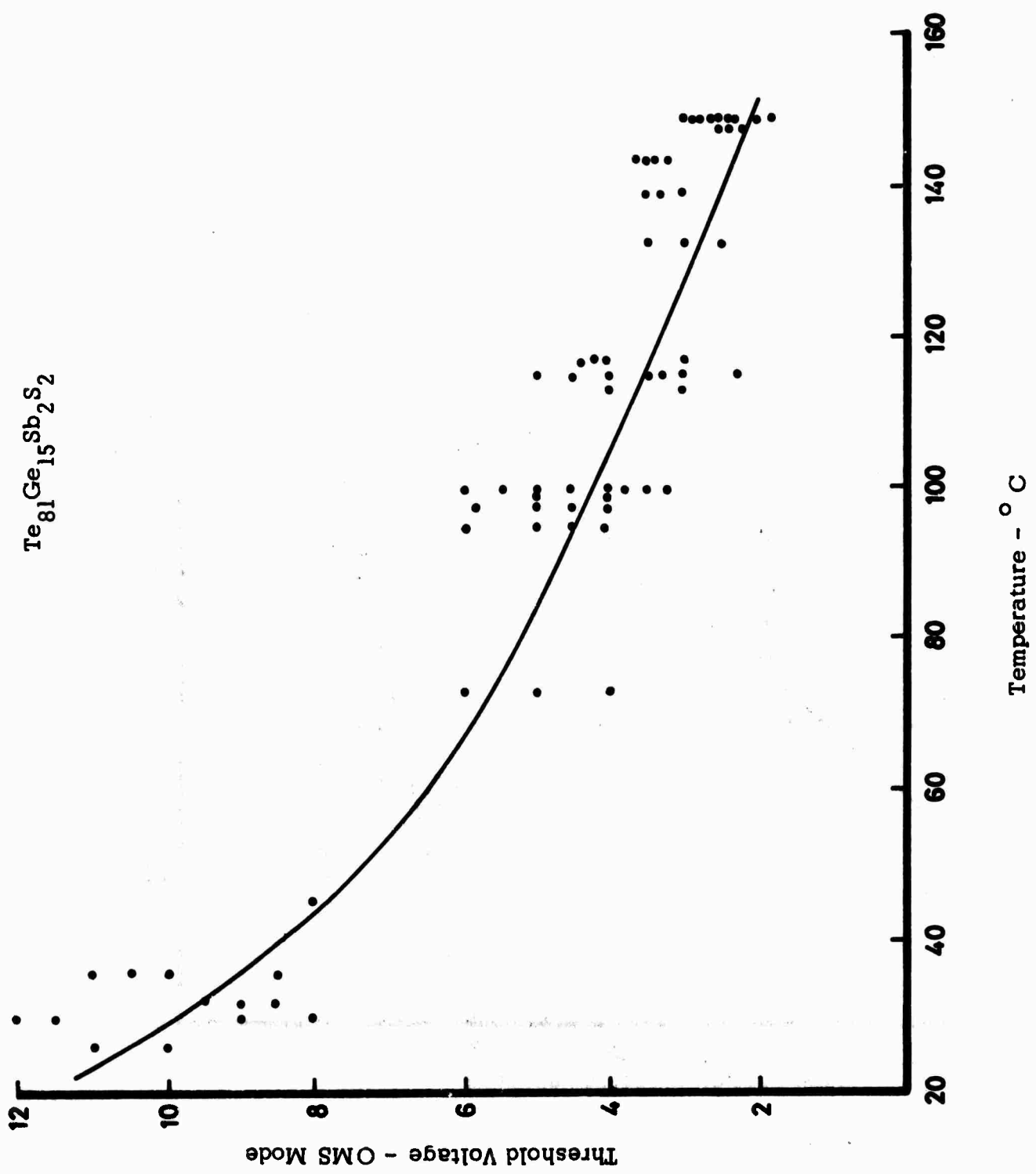


Fig. 4.13

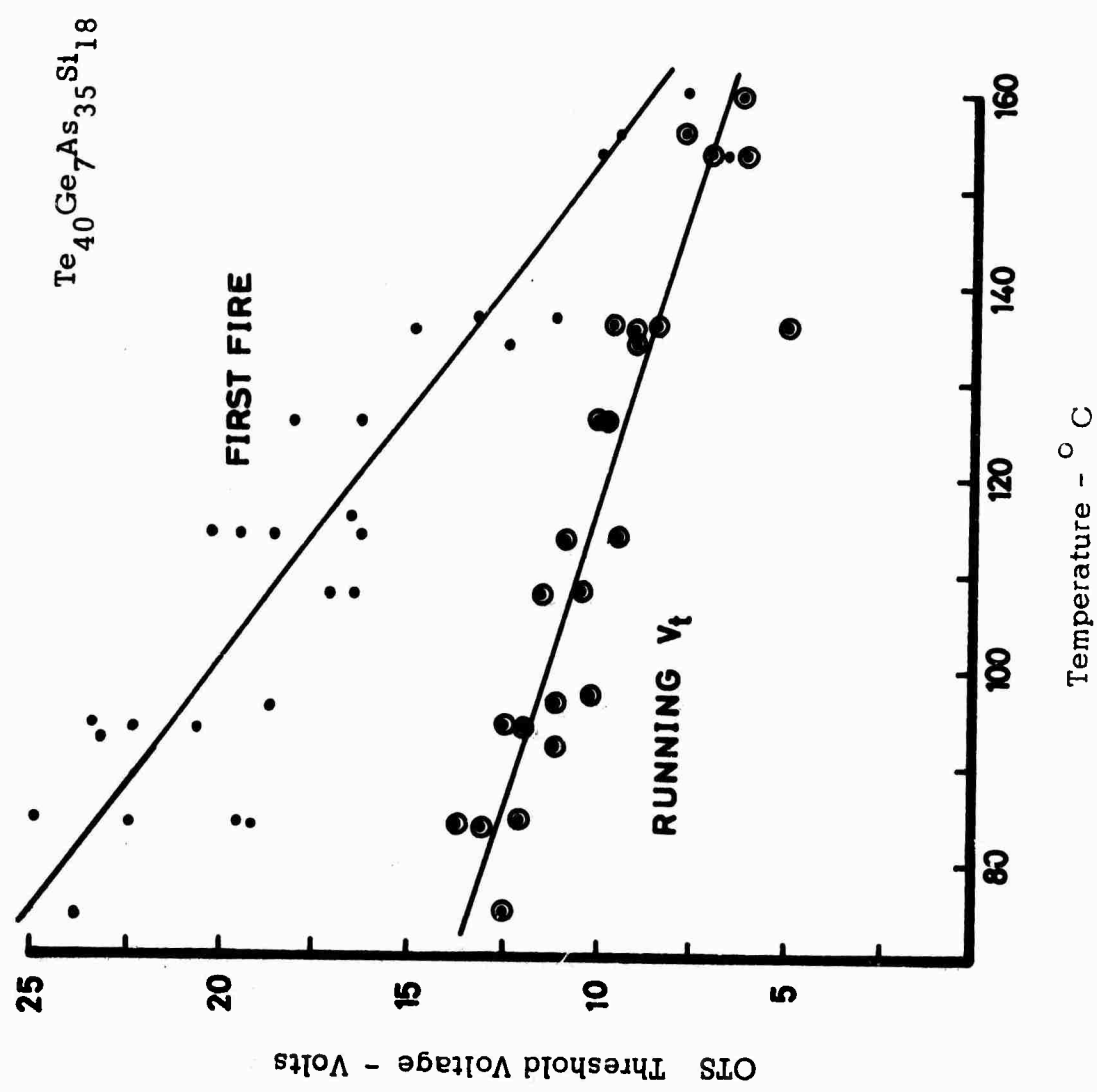


Fig. 4.19

The probing method is a rapid, reliable method for films whose thickness exceeds one micron. Above one micron, all measured properties scale accurately with thickness. At thicknesses less than one micron, the data become very scattered. This is probably due to the probe penetrating a small distance into the film and to variations in effective contact area. A technique has been evolved which would permit the fabrication of many, small sandwich devices per square centimeter of sample film which would eliminate the difficulties involved in probing methods.

The resistances and threshold voltages scale linearly with film thickness with the threshold fields being in the  $10^5 - 10^6$  V/cm range.

Switching OTS materials in the OMS pulsing mode results in "turn on" at  $V_{PT}$  on the leading edge of the set pulse and "turn off" when the conduction current falls below the minimum OTS holding current on the trailing edge of the set pulse. The values of  $V_{PT}$  and off state resistance measured for OTS materials were usually significantly higher than the values of  $V_{TS}$  measured in the ZPT-TS switching mode. We tentatively associate these differences with different degrees of threshold recovery in the two operating modes following the large capacitative discharge which accompanies the initial switching event.

Most of the materials surveyed can be operated in a stable ZPT-TS mode, and most are OTS materials. Many of the high threshold voltage OTS materials have high resistivities and will require fabrication into submicron thick sandwich configurations to properly evaluate OTS stability and lifetime. No examples of highly stable OMS materials were encountered in this survey. This was to be expected because most materials of this survey are rather stable multicomponent glasses and quite unlike the prototype OMS composition  $\text{Te}_{81}\text{Ge}_{15}\text{Sb}_2\text{S}_2$ . We therefore conclude that properties such as the glass transition temperature and resistivity may be varied widely by compositional variations and still yield stable OTS switches. However, the properties of OMS alloys depend sensitively on composition, and thus occur in a much narrower group of materials.

Work planned for the future includes extensive use of the scanning electron microscope, selective etchants, and microprobe to investigate the memory setting phenomena. In addition, we intend to fabricate simplified devices to further evaluate promising high  $T_g$  materials in device configurations.

## 5. EFFECTS OF SUBSTRATE TEMPERATURE ON THE PROPERTIES OF RF SPUTTERED OMS MATERIAL

As a first step in evaluating the effects of deposition parameters on the properties of thin films of amorphous chalcogenide materials, we have undertaken a broad study of the properties of OMS films produced by R.F. sputtering. By selecting a low temperature OMS material whose physical properties are well characterized in both bulk and thin film configurations, it has been possible to detect subtle property variations which correlate directly with substrate material and deposition temperature.

The material selected for this study is  $\text{Te}_{81}\text{Ge}_{15}\text{Sb}_2\text{S}_2$  whose  $T_g$  is  $130 \pm 3^\circ\text{C}$ . A six inch diameter cathode was prepared by hot-pressing crystalline material. For a standard run, the following substrates were utilized:

1. 1 - 1" x 1" - 7059 glass slide with two 1/4" x 1" x 0.1  $\mu\text{m}$  molybdenum pads separated by a 1/2" space. This substrate was placed beneath an out-of-contact aluminum mask in such a way that a 1" x 3/4" pad of OMS material was produced connecting the two molybdenum electrode pads; this test sample is identified as an "R-1" substrate in the following test and in Table 5.1.
2. 1 - 2" diameter silicon wafer (~ 0.025" thick coated with a ~ 1  $\mu$  layer of amorphous  $\text{SiO}_2$  produced by oxidation in steam at  $900^\circ\text{C}$ .
3. 1 - 2" diameter silicon wafer, oxidized as above and coated by an additional layer of molybdenum ~ 0.1  $\mu\text{m}$  thick.

TABLE 5.1 SUMMARY OF PHYSICAL PROPERTIES, SPUTTERED OMS MATERIAL

Run No. and Deposition Temperature	Substrate & State of Annealing	Electrical Activation Energy Measured 0 - 100°C	Resistivity at 250°C, ohm-cm	Probed Resistance Through Films, ohms	Threshold Voltage Probed at 25°C	Estimated percent Te Crystallization	Reflectivity in percent at 0.8 μm	Energy in eV at which $\alpha = 2 \times 10^4 \text{ cm}^{-1}$	Microprobe Results, Composition in Atomic Percent	
									Te = 81.0 Ge = 15.3 S = 1.5 Sb = 2.15	
SA-1179 20°C	R-1 Before	.45	$2.7 \times 10^4$	$1.0 \times 10^6$	10 11		40.5	1.125	Te = 81.0 Ge = 15.3 S = 1.5 Sb = 2.15	
	R-1 After	.10	$2.7 \times 10^2$	$3.3 \times 10^5$	6 9	~ 15	47.5	1.082		
	SiO <sub>2</sub> Before						41.7			
	SiO <sub>2</sub> After						47.5			
	Mo Before						40.2			
	Mo After						43.5			
SA-1170 550°C	R-1 Before	.47	$3.0 \times 10^4$	$2.8 \times 10^6$	19 15	~ 8			Te = 80.5 Ge = 16 S = 1.45 Sb = 2.15	
	R-1 After	.09	$2.3 \times 10^2$	$3.3 \times 10^5$	10 11	~ 3	39.3			
	SiO <sub>2</sub> Before									
	SiO <sub>2</sub> After									
	Mo Before									
	Mo After									
SA-1176 78°C	R-1 Before	.48	$5.2 \times 10^4$	$2.8 \times 10^6$	17 12	~ 12	43.7		Te = 81 Ge = 15.5 S = 1.35 Sb = 2.2	
	R-1 After	.16	$7.2 \times 10^2$	$8.0 \times 10^5$	9 12	~ 9	37.2	1.098		
	SiO <sub>2</sub> Before									
	SiO <sub>2</sub> After									
	Mo Before									
	Mo After									
SA-1171 110°C	R-1 Before	.47	$2.0 \times 10^4$	$1.2 \times 10^6$	13 14	~ 11	42.6		Te = 81.1 Ge = 15.5 S = 1.15 Sb = 2.25	
	R-1 After	.08	$2.5 \times 10^2$	$2.8 \times 10^5$	10 10	~ 8	48.0	1.100		
	SiO <sub>2</sub> Before									
	SiO <sub>2</sub> After									
	Mo Before									
	Mo After									
SA-1175 130°C	R-1 Before	.08	$3.9 \times 10^2$	$0.8 \times 10^6$	9 8	~ 5	39.2		Te = 81.3 Ge = 15.4 S = 1.00 Sb = 2.3	
	R-1 After	.17	$1.7 \times 10^3$	$6.8 \times 10^5$	9 10	~ 4	43.2	1.094		
	SiO <sub>2</sub> Before									
	SiO <sub>2</sub> After									
	Mo Before									
	Mo After									

These substrates were selected in order to maximize the variety of electrical and optical data which could be obtained. In addition, they offered the opportunity to verify the effects of substrate composition and structure upon the properties of freshly deposited thin films of OMS material, and, in addition, the effects of these substrate properties upon the subsequent crystallization of the films when annealed at  $170^{\circ}\text{C}$  for 4 minutes in air. This annealing procedure was selected as an appropriate environment for observation of the early stages of thermally induced crystallization of this particular OMS material.

The substrate temperature was controlled by resistive heating or water cooling of the copper anode and monitored by a thermocouple junction held in contact with one of the silicon wafer substrates on its free surface. Temperatures measured in this manner are internally consistent, although they may deviate substantially from the temperature at the substrate surface.

A series of five depositions was performed at temperatures ranging between  $20 - 130^{\circ}\text{C}$  as indicated in Table 5.1. The Ge:Te ratio and trace element (S, Sb) concentrations were determined by electron microprobe analysis and indicate that little fractionation occurred during deposition with the exception of a progressive depletion of S as a function of deposition temperature. Film thickness was  $1.7 \pm 0.2 \mu$  deposited in a  $6 \mu\text{m}$  argon atmosphere at an R.F. voltage of  $\sim 620$  volts and at a deposition rate of  $\sim 350 \text{ \AA/min}$ . Note that the

sputtering rate was essentially constant for all depositions.

The samples were examined by a wide spectrum of analytical tools in addition to the above-described microprobe analyses. Optical transmission and reflection, electrical resistance vs. temperature, switching characteristics and X-ray diffraction were measured on the substrate types indicated below:

Optical Reflection 1, 2, 3

Optical Transmission 1

Resistance vs. Temperature 1  
(in range 0 - 100°C)

Switching Characteristics 1, 3

X-ray Diffraction 2

One sample of OMS film coated on each substrate type was then annealed at 170°C for 4 minutes and reexamined via repetition of the above listed experiments to determine the comparative degree of thermal crystallization occurring during the annealment. In addition, half of each Mo coated 2" Si wafer was thermally decomposed by heating to ~ 450°C in a mass spectrometer, and the temperature dependence of the gaseous emissions was observed.

### 5.1 Detailed Description of Each Experiment

The optical reflection and transmission experiments were performed using the Beckman monochromator and an uncoated 7059 glass substrate as the transmission standard and an aluminum mirror for the reflection standard. Values of optical absorption coefficient

were calculated from the transmission data knowing the thickness and reflectivity of the absorbing OMS film. Samples annealed at  $170^{\circ}\text{ C}$  were carefully examined by optical microscopy to determine whether any surface roughening had accompanied partial crystallization, thereby invalidating the assumption of zero light scattering utilized in the reflectivity and absorption coefficient calculations, but none was observed.

The resistivity vs. temperature was measured by cycling the electroded samples from  $25^{\circ}\text{ C} \rightarrow 100^{\circ}\text{ C} \rightarrow -25^{\circ}\text{ C} \rightarrow +25^{\circ}\text{ C}$ , a range in which neither crystallization nor film cracking was anticipated. The raw resistance vs. thermocouple output data were reduced to resistivity vs. reciprocal absolute temperature.

From these graphs a best fit straight line was drawn through the data and the slope of each such line is tabulated as the electrical activation energy. In addition, the tabulated values of resistivity at  $25^{\circ}\text{ C}$  were read directly from the graphs. In general all resistivity data collected in the  $-25^{\circ}\text{ C}$  to  $+100^{\circ}\text{ C}$  temperature range could be fitted to a single straight line and little or no hysteresis was observed.

The X-ray diffraction experiments consisted of scanning each sample of the three substrate types deposited at each of the five deposition temperatures in a Norelco-Phillips X-ray diffractometer and monitoring the intensity of the Te (100) reflection. Aside from diffraction off the silicon substrates, only Te crystalline diffraction

peaks were observed and the Te (100) peak was selected for semi-quantitative analysis of the degree of crystallization since this reflection is the most intense during the earliest stages of crystallization.

The switching measurements were performed using an Electroglas Wafer Prober equipped with electropolished tungsten probes. One probe made contact with the molybdenum undercoating of either the Type 2 or Type 3 substrates while the second probe was lowered gently onto the free surface of the chalcogenide film against which it rested with the force of its own dead load. Using this geometry it is possible to initiate switching of a memory-type thin film using the following sequence of constant current pulses:

Set: 5 mA for 12 msec with a 2 msec ramp rise and fall

(max. voltage applied is 25 V)

Reset: 150 mA for 7.5  $\mu$  sec.

Ten points on each substrate were each switched ten times, and the results plotted in Table 5.1 are the averages of these data. In addition, a single point on each substrate was switched  $\sim$  2000 cycles at 10 cycles per second to observe switching stability. The resistance between the two probes prior to any switching pulses was measured on a Keithley 610 C Electrometer for each of the ten points tested, and the averaged data are listed in Table 5.1

The mass spectrometry experiments were intended to identify the molecular species in the vapor produced by heating scraped

films in an effusion cell and the approximate temperature dependence of their various partial pressures, as rough clues to the overall thermal stability of the alloy as a function of its deposition temperature.

We employed an Associated Electrical Industries model MS-10 mass spectrometer, a  $180^{\circ}$  magnetic focusing instrument capable of reading to  $m/e \approx 200$  and resolving individual peaks to  $m/e \approx 130$ . This is coupled with the aid of a short adapter or spool piece to an elaborately trapped Norton 3-inch oil-pumped high vacuum system capable of vacua in the range below  $5 \times 10^{-8}$  torr. Side ports in the adapter permit the introduction of a compact graphite-lined Knudsen cell, from the orifice of which (0.010" diameter) there exists a short (< 5 cm.) line-of-sight path to the accelerator region of the mass spectrometer. The design of this cell evolved from several unsuccessful earlier designs, and its temperature calibration was established with respect to the melting point of lead. All active films were removed from their substrates by scraping with a clean glass slide onto plate glass. The resultant powder, weighing slightly more than 5 mg., was then loaded into a graphite crucible which had been previously baked at  $600^{\circ}\text{C}$  under high vacuum. A small area (ca.  $10 \text{ mm}^2$ ) of the silicon substrate was also crushed and inserted in the crucible.

During operation, the temperature of the Knudsen cell is raised

slowly and uniformly, at a rate of approximately 2 degrees per minute. The mass spectrometer is meanwhile scanned repetitively over both low and high mass ranges. Thus the entire mass spectrum from  $m/e = 18$  to  $m/e \approx 200$  is sampled in approximately  $25^\circ$  increments. By scrupulous attention to the cleanliness of the apparatus and the standardization of operating procedure, it has been found possible to produce spectra in which the ever-present background due to residual air, hydrocarbons, and elastomers is substantially independent of the temperature of the Knudsen cell. Against this background the strongly temperature-dependent lines due to the specimen are immediately apparent, as shown in Figure 5.1., a representative set of traces. These lines form a "mass signature" whose deposition, strength, and temperature dependence are characteristic of the material. In most cases, it is observed that the rate of vapor evolution attains a broad maximum and then declines, presumably indicating exhaustion of the volatile fraction.

## 5.2 Summary of Experimental Results

The electrical, optical and X-ray results are well summarized in Table 5.1, and their interpretation is relatively straight-forward. The films deposited at  $20 - 110^\circ\text{C}$  show closely similar properties in the virgin state: a resistivity of  $3.5 \pm 1.5 \times 10^4 \Omega/\text{cm}$ ; a conductivity activation energy of  $0.465 \pm 0.015 \text{ eV}$ ; a reflectivity at  $0.8\mu$  of  $39 \pm 2\%$ ; an optical absorption coefficient of  $2 \times 10^4 \text{ cm}^{-1}$  at  $1.12 \pm 0.01 \text{ eV}$ .

The probing of the films before and after the  $170^\circ\text{C}$  anneal revealed

Fig. 5.1

Temperature dependence of representative lines in the mass spectrum of specimen SA-1171. Numbers near curves indicate mass/charge ratio. Note that rapid variation with temperature serves to distinguish "characteristic" lines of the specimen itself (e.g.,  $m/e = 76$ ) from background lines due to the apparatus (e.g.,  $m/e = 58$ ). Normal melting point of this specimen ca.  $370^{\circ}$  C.

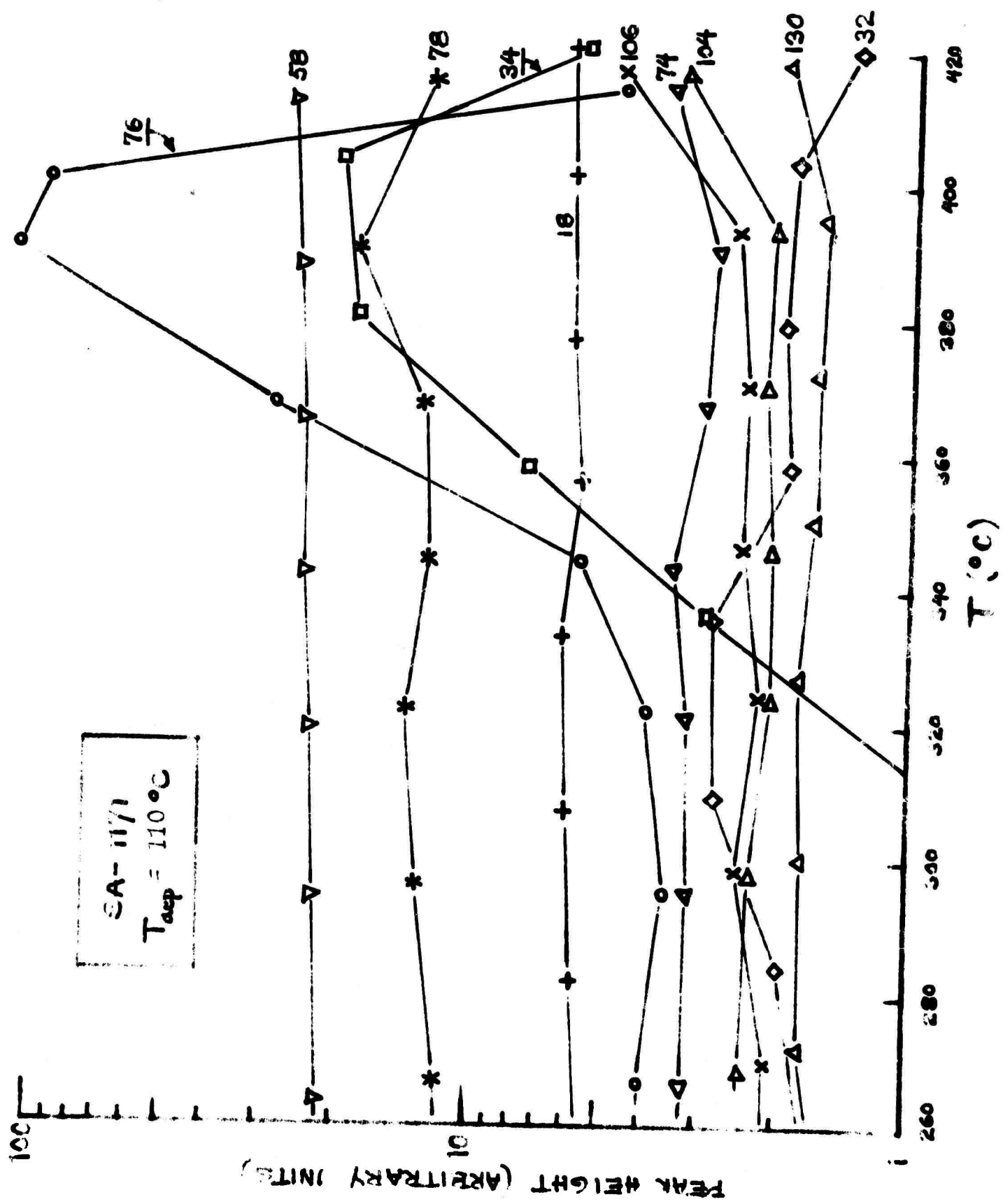


Fig. 5.1

only a tenfold decrease in resistance in contrast to the 100-fold decrease in resistivity as calculated for the coplanar electroded R-1 patterns. A possible explanation of this discrepancy is that the Te crystallites which form at 170°C nucleate and grow primarily along one surface of the film, thus providing a lower resistance path for coplanar configuration measurements than for sandwich configuration measurements.

Reflectivity and optical absorption are mostly increased by the 170°C anneal with the exception of the reflectivity of several of the higher deposition temperature films. Although none of these films contained optically detectable crystallites or other indication of surface scattering sites, a possible explanation for the reduced reflectivity of these films is the presence of tiny surface crystallites less than 1  $\mu\text{m}$  in size. Such crystallites have been observed in SEM photographs and may effectively reduce reflectivity by scattering light out of the narrow receiving slit in the reflectometer. If this explanation is correct, then the low-reflectivity partially-crystallized films contain a lower crystallite density and a larger crystallite size than the films deposited at lower temperatures.

The mass spectrometric results are presented in Table 5.2, along with data from comparison runs using bulk samples. These techniques are relatively untested in contrast to the other measurements presented for the  $\text{Te}_{81}\text{Ge}_{15}\text{Sb}_2\text{S}_2$  films and therefore

TABLE 5.2  
SUMMARY OF MASS SPECTROMETRIC RESULTS

Specimen Number	Deposition Temperature or Form	Characteristic Lines	T <sub>onset</sub>	T <sub>max</sub>	Relative Strength
SA-1179	20°	34 74 <sup>a</sup> 76 130 <sup>b</sup>	335° --- 320° 380°	390° 515° 402° 440°	.04 .15 .29 .03
SA-1170	55°	34 76	290° 320°	358° 370°	.06 .12
SA-1176	78°	34 76	330° 330°	377° 388°	.10 1.30
SA-1171	110°	34 76	300° 334°	395° 390°	.40 2.20
SA-1175	130°	34 76	327° 380°	>450° 434°	>.20 .44

a: Ge mass multiplet, consisting of m/e = 70, 72, 73, 74, 76.

b: Te mass multiplet, consisting of m/e = 122, 124, 125, 126, 128, 130.

TABLE 5.2, continued

Specimen Number	Type	Characteristic Lines	T <sub>onset</sub>	T <sub>max</sub>	Relative Strength
Bulk Te <sub>81</sub> Ge <sub>15</sub> Sb <sub>2</sub> S <sub>2</sub>	massive	34 74 <sup>a</sup> 106 <sup>c</sup> 130 <sup>b</sup>	365° 380° 390° 355°	450° 450° 465° 493°	.04 .09 .42 1.15
Bulk Te <sub>81</sub> Ge <sub>15</sub> Sb <sub>2</sub> S <sub>2</sub>	crushed	34 74 <sup>a</sup> 76 106 <sup>c</sup> 130 <sup>b</sup>	> 240° --- 370° 380° 385°	350-470° 435° 435° 510° 515°	.96 .08 .19 .14 .80
Bulk Ge <sub>17</sub> Te <sub>83</sub>	crushed	34 74 <sup>a</sup> 78 130 <sup>b</sup>	--- --- --- 360°	440° 370° 370° >550°	.05 .04 .40 1.25

c: GeS mass multiplet, consisting of m/e = 102, 104, 105, 106, 108.

require considerable detailed comment to be understood thoroughly.

The first column in Table 5.2 gives the run number in which the specimen was prepared. The second column gives the temperature of the deposition. The third column gives the mass/charge ratio of the most prominent lines in the "mass signature" of the specimen. The fourth column gives the temperature at which each characteristic line first emerges from the background spectrum; and the fifth column gives the temperature, if any, at which this line attains its maximum strength. Such temperatures are of course approximate, in view of the coarseness of temperature increments, and embody a certain amount of arbitrary curve-fitting. A dash indicated that the line is so weak, or grows so gradually, that a well-defined temperature of onset cannot be identified. Finally the sixth column gives the maximum strength attained by the line, here in units of  $10^{-13}$  A of electrometer current. We have not thought it necessary to normalize this maximum strength with respect to some residual background line, inasmuch as the total background pressure is virtually identical from run to run.

It will be seen that the "mass signature" of the sputtered  $\text{Te}_{81}\text{Ge}_{15}\text{Sb}_2\text{S}_2$  alloy consists typically of singlets at  $m/e = 34$  and  $m/e = 76$ , peaking at roughly the same temperature, followed for the 20° deposition by multiplets at  $m/e \approx 74$  emerging at successively higher temperatures. The latter can be unambiguously assigned to elements

tellurium and germanium, respectively, as proven by the correspondence between the relative strengths of the members of each multiplet and the natural isotopic abundances of these elements. (Note that the compound  $\text{GeTe}$  exceeds the mass range of the instrument.  $\text{Ge}_2$  has been detected, however.) The assignment of  $m/e = 34$  and  $m/e = 76$  is only slightly more difficult. The presence of weak satellites at  $m/e = 36$  and  $m/e = 78$ , together with a slight dip in  $m/e = 32$  just before the principal lines appear, strongly suggest binary sulfur compounds whose other component is monoisotopic. Thus we have assigned these lines to hydrogen sulfide ( $\text{H}_2\text{S}$ ) and carbon disulfide ( $\text{CS}_2$ ) respectively. The bulk  $\text{Te}_{83}\text{Ge}_{17}$  sample displays a stray line at  $m/e = 78$ , and we are inclined to believe it represents residual disiloxane ( $\text{SiH}_3\text{Si}_2\text{O}$ ) from the silicone oil quenching procedure.

Some light is shed on the question of the origin of the  $\text{H}_2\text{S}$  and  $\text{CS}_2$  vapors by comparison with measurements on bulk alloys. At first glance, it might be thought that both compounds have a common origin in some artifact of our measuring technique; e.g., perhaps only elemental sulfur is released from the films, which then scavenges hydrocarbons from the interior of our vacuum system. If this were the case, one would expect the  $\text{H}_2\text{S}/\text{CS}_2$  ratio to be roughly constant, whereas in fact it varies strikingly from run to run. Note too that the massive bulk quaternary alloy evolves only a vanishingly

small amount of  $H_2S$ . Indeed, comparison with bulk  $Te_{83}Ge_{17}$ , a sulfur-free variant of the quaternary alloy, suggests that this amount of  $H_2S$  may be a residual of the apparatus. Crushed bulk  $Te_{81}Ge_{15}Sb_2S_2$ , however, exhibits the largest and broadest  $H_2S$  signal encountered in the program. The implication is strong that  $H_2S$  evolves from the surface of the material, possibly via a hydrolysis reaction with water vapor in the air, and to this extent its appearance is a consequence of the process of scraping films free of their substrates.

The  $CS_2$  line, on the other hand, almost certainly arises at an earlier stage of sample preparation. In contrast to the thin film series where it is invariably the strongest line present, it is absent in the massive bulk  $Te_{81}Ge_{15}Sb_2S_2$  alloy and in crushed bulk  $Te_{83}Ge_{17}$ , and only moderately strong in crushed bulk  $Te_{81}Ge_{15}Sb_2S_2$ . We conclude that its intensity variations reflect real differences in the composition of the sputtering cathode, the residual hydrocarbon content of the sputtering atmosphere, or other factors characteristic of the machine itself; and these differences largely outweigh the changes due to deliberate variation of deposition temperature.

We now turn to consideration of the  $m/e \approx 74$  (germanium) and  $m/e \approx 130$  (tellurium) mass multiplets. Here the most striking single observation is the great relative strength of the Te signal from bulk specimens, both massive and crushed. By contrast, Te lines are

weak or absent throughout the thin film series. Ge lines, on the other hand, are vanishingly small in the bulk, and of moderate strength in thin films, indicating weaker bonding or more numerous defect sites in the latter. (Those runs in the thin film series for which no Ge is tabulated terminated at temperatures too low to permit evaluation.)

We intend to calibrate the Knudsen cell to ascertain whether or not equilibrium partial pressures are established for both the thin film and bulk specimens. This is necessary for a quantitative analysis of the mass spectrograms.

We intend to pursue these studies for other sputtered film compositions, emphasizing techniques which reduce the sample handling contamination problems incurred in the presently reported study, and to extend the mass spectrometer gas analysis technique to directly monitor the sputtering atmosphere during film deposition.

This study of the effects of substrate temperature on the properties of sputtered OMS films revealed the following. OMS films sputtered at  $110^{\circ}$  C, that is about  $20^{\circ}$  C below the glass transition temperature, appear to be better suited for device purposes than films sputtered at lower temperatures. They appear more stable and have a smaller relative change of the threshold voltage after first firing and after annealing in air at  $170^{\circ}$  C for 4 minutes.

## 6. THERMAL CRYSTALLIZATION OF SELECTED Te-BASED CHALCOGENIDES

The purpose of this part of the program has been to elucidate the mechanisms, morphologies and rates of thermal crystallization in certain memory glasses based on the Te-Ge eutectic and to uncover the influence of impurities and interfaces. Among the issues to be resolved were questions of phase separation (spinodal decomposition) as a precursor to the crystallization, the role of micro-phase segregation that accompanies crystallization, the relative stabilities and rates of formation of the various crystalline phases, and the relationship of thermodynamic factors to the nonequilibrium decomposition of the alloy glasses. The influence of the substrate (on which the glass has been deposited) on the nucleation rate was also considered an important issue.

Some of these questions have been resolved while others are currently underway in various stages. The primary tools for these studies have been X-ray diffraction (on 1 - 10  $\mu$  films) and transmission electron microscopy (TEM) and electron diffraction on thinner (300 - 800  $\text{\AA}$ ) films. Occasionally, reflection electron diffraction has been employed where the interface nucleation behavior of thin films on thick substrates has seemed interesting. Finally, scanning electron microscopy (SEM) and electron beam  $\mu$ -probe analysis has been performed where it was considered relevant.

We wish in this work to emphasize the thin film aspect. It certainly could have been decided to do much more controlled diffraction studies, for example, by using bulk glasses especially prepared to ensure randomness of

crystallite orientation, infinite thickness, more homogeneous nucleation and so forth. It was decided, however, to use the sputtered films in order to replicate more closely those thermal aspects of crystallization which might obtain in sputtered 1 - 2  $\mu$  films in actual memory devices. This naturally placed limitations on the work as we fully expected (and were justified in our expectations) to observe nonrandom crystallographic features, or crystallization textures, which sometimes varied over the sample face and rendered the quantitative use of relative diffraction intensities impossible. Still some quite general conclusions emerge about crystallization behavior which appear to be consistent with the thin film TEM studies. It should also be noted that very small changes in composition with respect to impurity content - including, for example, the influence of dissolved or attached oxygen - have quite remarkable effects on the initial crystallization behavior of virgin films. Subsequent growth behavior on cycling, after nucleation has been initiated, seems less sensitive.

#### 6.1 Thermodynamics and Metastability in the Partial System Te-GeTe

The basis for our analysis is the well-known Ge-Te phase diagram where the relevant portion extends from pure Te to the compound GeTe. The present description is concerned with the extension of the Te-rich liquidus boundary into the region below the eutectic where the equilibrium products are Te and the telluride, GeTe. In Figure 6.1(a), the partial diagram is drawn to include the relevant boundaries as discussed below. It is assumed that the

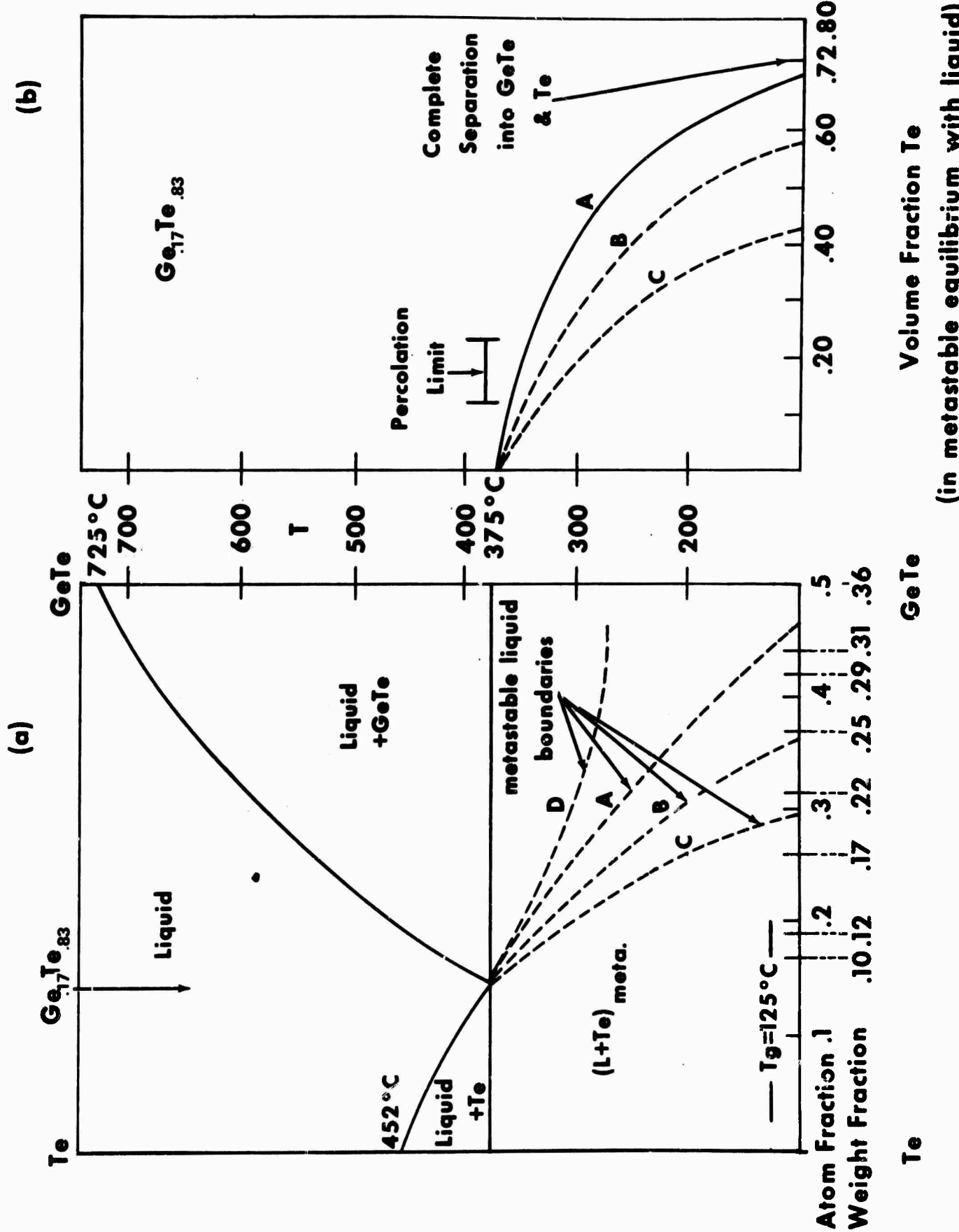


Fig. 6.1

(in metastable equilibrium with liquid)

eutectic comes at  $Ge_{15}Te_{85}$ , but this could vary by as much as a few percent. The composition of  $Ge_{17}Te_{83}$  is chosen because it simulates in many respects the memory alloy  $Ge_{15}Te_{81}Sb_2S_2$ , on which we have accumulated so much other data. The differences in crystallization behavior between  $Ge_{17}Te_{83}$  and the above quaternary glass are also worthy of note and will be discussed.

For the alloy in question,  $T_g \approx 125^\circ C$ . Above that temperature it will be more or less free to crystallize into one or more phases. The morphology of that crystallization process was noted some time ago by Willens<sup>14</sup>, in a splat-cooled alloy of similar composition, as being dendritic. Should that tendency prove to be a universal feature of crystallization in these Te-Ge alloys it would seem to rule out nucleationless homogeneous phase separation (spinodal decomposition) as the intermediate path in their crystallization. Another possibility of course is the eutectic decomposition of the alloy into its equilibrium -- or nearly equilibrium -- products. The dendritic growth again militates somewhat against that interpretation.

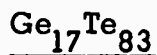
Consistent with the dendritic morphology is the initial crystallization of Te and the rejection of Ge into the glass. This has two immediate consequences. The first is that such a process is self-regulating or self-inhibiting because as Ge is rejected into surrounding glass its glass transition and viscosity are increased

as long as the alloy composition falls to the low Ge side of  $\text{GeTe}_2$ .<sup>15</sup> The traditional nucleation behavior is thus altered by this additional inhibition. In other words, not only is the driving force reduced but the pre-exponential part of the diffusion controlled growth is altered.

The second consequence is that the volume fraction of Te that can crystallize out is limited by the application of the lever law to the metastable liquid boundary. Eventually of course the sluggish GeTe precipitation will take place from the interdendritic glass and release the remainder of the Te, but initially the amount of Te is regulated by the metastable boundary. In fact the amount of Te crystallizing from the glass should decrease with increasing temperature if the telluride does not form and if the process is allowed to proceed to the metastable boundary at any temperature.

An important line in the phase diagram is thus the extension of the Te-rich liquidus below the eutectic temperature. In Fig. 6.1(a), curves A, B and C are all reasonable choices inasmuch as the actual liquidus is not well known and its extension is thus doubly tentative. Curve D, which would be more characteristic of a very non-ideal system tending toward phase separation, is more speculative but it obviously permits a much higher volume fraction of Te crystallizing from the metastable liquid at temperatures near the eutectic.

In the equilibrium mixture Te + GeTe, for the 17 percent alloy, the volume fraction of Te is about 0.72 as given by the simple calculation below:



Wt. Fract. Ge = 0.10 (in glass)

Wt. Fract. Ge in GeTe = 0.36

$$\frac{\text{Wt. Fract. GeTe}}{\text{Wt. Fract. Te}} \text{ (in equil. mixt.)} = \frac{0.10}{0.26}$$

Wt. Fract. Te in fully crystallized mixt. = 0.72

Densities:  $\rho$  (Te cryst.) = 6.24 gms/cc.

$\rho$  (GeTe cryst.) = 6.20 gms/cc.

(and thus  $\rho$  (bulk crystallized glass)  $\cong$  6.2 gms/cc.)

$\rho$  (Ge<sub>17</sub>Te<sub>83</sub> glass) = 5.60 gms/cc.

$\rho$  (GeTe glass)  $\cong$  5.40 gms/cc.

Thus: vol. fract. Te in fully cryst. glass  $\cong$  0.72

In Figure 6.1(b), the volume fractions of Te in equilibrium with the metastable Ge-enriched liquid (glass) have been calculated simply by applying the lever law to the curves in Fig. 6.1(a). Assuming A, for example, to be a reasonable extension, curve A in Fig. 6.1(b) yields about 50 volume percent Te crystallized at 275° C in the absence of GeTe. The percolation limit of ~ 15-25 percent is included to indicate about where one would expect a

conductivity cut-off in a crystallized film. This has obvious applications to the memory behavior of a chalcogenide glass based on this composition, but in the first instance it should simply serve as a precaution in applying resistivity as a measure of the crystallization kinetics in semiconductor glasses.

## 6.2 X-Ray Diffraction

The present X-ray diffraction has been on samples of  $Ge_{15}Te_{81}Sb_2S_2$ . The questions of preferential association of the Sb and S with either the telluride or Te phases will be discussed briefly in a later section as will their apparent influence on the rates and morphologies.

### 6.2.1 Experiment

The X-ray samples were approximately 1.5 - 2.0 microns ( $\mu$ ) in thickness sputtered over Corning 7059 1" x 1" glass plates. The samples were analyzed in the as-sputtered condition and all were amorphous. Because the linear X-ray absorption coefficient for this chalcogenide glass composition is  $\mu_1 \approx 1500 \text{ cm}^{-1}$ , for  $CuK_{\alpha}$  radiation, a 2.0  $\mu$  sample gave more than 60% of the diffracted intensity of a bulk sample even at  $2\theta = 70^\circ$ . Inasmuch as we were dealing with the early stages of crystallization, in most cases, the X-ray traces were not taken in the back reflection region and we did not suffer a lack of intensity due to insufficient thickness. Again the choice of thickness

was motivated by a desire to reproduce some of those conditions which would prevail in a device.

The X-ray diffractometer was a standard Phillips powder unit equipped with a constant potential source and a fine-focus Cu X-ray tube run at 40 kV and 15 ma. The detection system consisted of an AMR post specimen graphite monochromator and a scintillation counter with pulse height analyzer. Following the usual electronics, a strip chart recorder was used to record the scans.

Excellent noise free signals were observed with the first broad peak in diffuse scattering from the glassy material reaching about 500 counts per second.

It is difficult to estimate the detectability of a small volume fraction crystallized but we would place this at about .5% - 1%. The problem is further complicated by the fact that the nucleation in these films initially occurs mainly at the 7059/chalcogenide interface. It is therefore quite reasonable to assume that a 50 Å interface layer of well-nucleated Te crystallites will not be visible in a diffraction experiment of this kind. To illuminate this particular question, we are currently running X-ray and electron diffraction studies together on, respectively, 1.5  $\mu$  and 300 Å films from the same deposition. Reflection electron diffraction from the

300 Å films will reveal, in addition, distinctions among various interfaces in providing easy nucleation sites for the chalcogenide. The same experiment on the thicker films will deal with the nucleation events at the chalcogenide - air interface. Preliminary results to date indicate that it is the substrate - chalcogenide interface which initiates nucleation, but the top surface should not be disregarded.

#### 6.2.2 Results

The runs in this series of X-ray experiments spanned a range of temperatures (one sample run for progressively longer times at each temperature) from 140° C to 275° C including: 140° C, 160° C, 180° C, 200° C, 220° C, 250° C, 275° C all for times ranging from 1-2 minutes up to 18 hours.

The X-ray data were collected at room temperature after anneals at the elevated temperatures. The results are listed below:

1. Only hexagonal Te crystallites were observed for the 18 hour anneals up to 220° C.
2. GeTe does not appear in the X-ray pattern from these samples until 250° C.
3. There appears to be a tendency, increasing with temperature, towards an (00.1), or C axis, crystallization texture in the films. Until 275° C where a more random texture appears, there is a definite

enhancement of 003 with respect to 101 and 102. For example, while the ideal integrated intensity ratios of (101)/(102)/(103) are 100/37/8, these ratios ranged roughly from 100/54/20 at 160° C, to 100/66/26 at 180° C, to 100/156/72 at 220° C back to 100/87/40 at 250° C and finally to 100/52/17 at 275° C which latter value is closest to random. The above are representative of the various temperatures, although, in fact for some treatments the intensities varied over the sample face in a nonsystematic way. Still the trend is as we note above.

4. The Te particle sizes seemed to be more a characteristic of the annealing temperature than of the time spent at that temperature. This is a weak tendency based on monitoring the Te(102) peak at  $2\theta \approx 38.4^\circ$  which is a rather low angle reflection to be using for a particle size estimate but turns out to be a necessary compromise in this case. Particle sizes were calculated using the Scherrer formula:

$$\Delta 2\theta(hkl) = \frac{.9\lambda}{L \cos \theta(hkl)}$$

$$\lambda = 1.54 \text{ \AA} (\text{CuK}_\alpha)$$

$\Delta 2\theta(hkl)$  = full  $2\theta$  width (in radians) of  
of the  $hkl$  reflection at the  
half-maximum intensity above  
background.

$L$  = avg. crystallite size.

The instrumental broadening was removed using a standard Te pattern run with the same instrumental settings where, for the (102) reflection,

$\Delta 2\theta \approx 0.38^\circ$ . If both profiles have a Cauchy shape, the breadths are given below, where  $\Delta 2\theta_{\text{stand}} = 0.38^\circ$ :

$$\text{Cauchy: } \Delta 2\theta_{\text{true}} = \Delta 2\theta_{\text{meas}} - \Delta 2\theta_{\text{stand}}$$

If they both have Gaussian shapes, the breadths are related by:

$$\text{Gaussian: } (\Delta 2\theta_{\text{true}})^2 = (\Delta 2\theta_{\text{meas}})^2 - (\Delta 2\theta_{\text{stand}})^2$$

In Table 6.1 below are the results of the particle size estimates for each temperature. We have chosen to represent each annealing temperature by a single particle size (plus a large error). This, as we noted, is really not true. In fact, we would naturally expect both nucleation and growth at any temper-

TABLE 6.1  
 Particle Sizes in the Thermal Crystallization of Te and GeTe  
 from the Memory Glass  $\text{Ge}_{15}\text{Te}_{81}\text{Sb}_2\text{S}_2$

Annealing Temperature	$\Delta 2\theta$ (102) refl.	Particle Size, $L(\text{\AA})$		Average
		Cauchy	Gaussian	
160°C	1.00° ± .05	140	94	115 ± 30
180°C	.85° ± .03	185	114	150 ± 40
200°C	.75° ± .04	233	134	184 ± 50
220°C	.60° ± .03	399	192	295 ± 100
250°C	.50° ± .02	721	261	490 ± 230
250°C (final)	.39° ± .02			≥ 1,000 Å
GeTe	$\Delta 2\theta$ (200) refl.			
275°C (18 hrs.)	.65° ± .04	254	149	200 ± 50

ature. But, while there was a small decrease in half width during a given temperature sequence, the initial breadth at the next higher temperature was usually smaller than the final breadth at the lower. This was true even though the final intensities at the lower were the same or greater than the initial at the higher. (Naturally, separate samples are used for each temperature series.) In fact, for example, at  $160^{\circ}\text{C}$  after 18 hours, the average particle size was  $L \approx 115 \text{ \AA} \pm 30 \text{ \AA}$  while at  $180^{\circ}\text{C}$  after 20 minutes, the integrated intensities were definitely less but the particle size was  $140 \text{ \AA} \pm 50 \text{ \AA}$  which finally increased to, at best,  $170 \text{ \AA} \pm 50 \text{ \AA}$  after 18 hours. Therefore, rather than report a trend at a given temperature, we have merely assigned a size to each temperature based on the average of the variations at that temperature but weighted toward the long-time annealing results. The GeTe particle size after 18 hours at  $275^{\circ}\text{C}$  was only  $200 \text{ \AA} \pm 50 \text{ \AA}$ .

6.2.3 Conclusions

1. The crystallization of Te dominates the thermal crystallization of the memory glass  $Ge_{15}Te_{81}Sb_2S_2$ . (In fact, from what we can determine, Te crystallization is the dominant factor in the memory setting of the majority of thin film Te based chalcogenides). The influence of impurities is yet to be discussed, but it seems apparent that they must be important in determining the rate and scale of Te crystallization and the ease of GeTe formation.
2. The particle size of the Te increases monotonically with annealing temperature but is not so sensitive a function of time at any temperature. At  $275^{\circ}C$ , the Te crystallite size has reached the limiting observable value of  $\geq 1,000 \text{ \AA}$ .
3. The Te appears to come out with a slight to strong (00.1) or C-axis texture normal to the film. In other words, the C axis tends to grow and/or nucleate more easily normal to the plane of the film. This tendency increases with increasing temperature and then falls off as the ease and rate of crystallization enhances the tendency toward randomness.
4. The GeTe does not appear until several minutes at  $250^{\circ}C$ . This is difficult to assess because only two peaks are really prominent in the well crystallized film in any

case: i.e. the (200) and, to a lesser extent, the (111). But it can be seen that the GeTe precipitation is a sluggish affair and that the particle or crystallite size assumed by GeTe is much smaller than for Te:

$200 \text{ \AA} \pm 50 \text{ \AA}$  after 18 hours at  $275^\circ \text{ C}$ . This suggests that the GeTe eventually comes out between the particles of Te as the Ge enriched glass, formed by the Te precipitation, finally itself crystallizes into GeTe + Te.

There is a bit of evidence for an enhancement of Te content as the GeTe comes out. But the evidence is too limited to warrant elaboration. It does seem that both of our stipulations about the metastable crystallization of Te will be important. These were the limitations on volume imposed by both the metastable liquidus and the enrichment of Ge in the remaining glass which raises its  $T_g$  and thus increases its resistance to crystallization.

### 6.3 Transmission Electron Microscopy

The microscopy and electron diffraction reported here will be confined mainly to a description of the crystallization in thin ( $\sim 500 \text{ \AA}$ ) films of  $\text{Ge}_{15}\text{Te}_{81}\text{Sb}_2\text{S}_2$  and  $\text{Ge}_{17}\text{Te}_{83}$ .

#### 6.3.1 Experiment

Films of both compositions were sputtered onto standard carbon coated  $1/8"$  Nickel electron microscope grids.

In addition, for reflection electron diffraction, 1" x 1" substrates of 7059 were included in some of the runs.

All anneals were performed on these grids under an atmosphere of dry  $N_2$  and the temperature was known to be better than one degree. The samples were then examined in transmission in the tilting stage of a JEOLCO JEM-7 microscope. Both compositions were studied in the as-sputtered condition and after anneals at  $130^\circ C$ ,  $140^\circ C$ ,  $275^\circ$  and  $340^\circ C$  where  $T_g \approx 125^\circ C$  for both. No attempt was made in these initial studies to duplicate the rather extensive series of treatments that were given the X-ray diffraction samples. In fact, the anneals were as follow:

1. 5 hours @  $130^\circ C$
2. 5 hours @  $140^\circ C$
3. 10 minutes @  $275^\circ C$
4. 20 minutes @  $340^\circ C$  after 10 minutes @  $130^\circ C$

The rationale was that we wished to explore the very earliest stages of heterogeneous interface crystallization that were inaccessible to the X-ray work on thicker films and also to explore the morphology and fine structure of a sample treated so as to initiate GeTe at a higher temperature in two ways: a) directly crystallizing from a virgin film

and b) precipitating from a film already nucleated at a lower temperature.

Because of the prior issue of phase separation (spinodal) decomposition) versus nucleation and growth as a crystallization mode, we also ran selected samples of  $Ge_{15}Te_{81}Sb_2S_2$  at  $120^\circ$  for 3 hours. The point here was to determine, via reflection electron diffraction, if there would be appreciable heterogeneous surface or interface crystallization at a temperature well below that at which no volume crystallization took place in the X-ray study. The latter films were  $2\mu$  thick and 500 Å thick.

Finally in conjunction with this TEM work,  $\mu$ -probe analysis and SEM studies were performed. The  $\mu$ -probe was on the bulk thermally equilibrated quaternary alloy while the SEM (plus solid state -  $\mu$  chemical analysis) was on one of the thermally treated microscopy samples (500 Å @  $275^\circ$  C for 10 minutes).

#### 6.3.2 Results and Discussion

In Figs. 6.2(a) and 6.2(b) are transmission electron micrographs at 40,000X of  $Ge_{15}Te_{81}Sb_2S_2$  and  $Ge_{17}Te_{83}$  respectively annealed at  $140^\circ$  C for ~ 5 hours. In the first place, the crystallization has clearly not proceeded

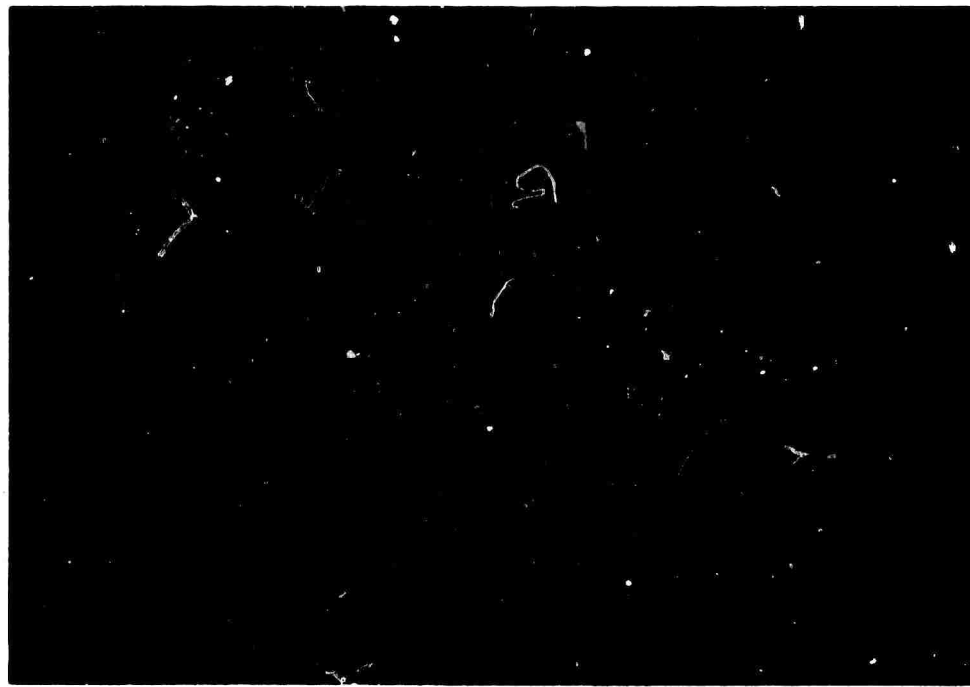


**Figure 6.2 (a)** 40,000X transmission electron micrograph of  $\text{Ge}_{15}\text{Te}_{81}\text{Sb}_2\text{S}_2$  annealed for 5 hours at  $140^\circ\text{C}$ .



**Figure 6.2 (b)** 40,000X transmission electron micrograph of  $\text{Ge}_{17}\text{Te}_{83}$  annealed for 5 hours at  $140^\circ\text{C}$ .

dendritically at this temperature. The grain size, which is indicated by the size of the sharp dark dots and not by the large scale mottling, is extremely fine and the orientations are essentially random as reflected in selected area diffraction patterns taken from large areas of these samples. The light network which runs throughout the darker crystalline regions is residual amorphous chalcogenide. The darker areas contain mainly Te crystallites and no telluride. In either case, ((a) or (b)), it is difficult to estimate the volume fraction crystallized and it is probably true that the Ge-rich glass between the crystalline regions has prematurely retarded the growth of these regions at 140° C. Because the difference in overall electron transmission of the two areas is not that large, the Ge enrichment in the light areas (Ge is the less absorbing) is not substantial. The Te grain size is notably finer in the  $Ge_{17}Te_{83}$ .

The morphology in these two samples is interesting. It is almost as if the Te crystallized spherulitically but on an extremely fine scale such that while the spherulites range from ~ 3000 Å - 7000 Å the individual crystallite sizes are ~ 50 - 100 Å which is consistent with an extrapolated estimate from the previous section on X-ray results. The latter is reasoned from the sizes of the black

dots that arise when, with a fine objective aperture, a single particle diffracts out of the image. The growth is apparently slow at this temperature and the randomness of crystallite orientation comes possibly from multiple nucleation continuously seeded at the old nuclei as in a spherulite. A selected area diffraction pattern from one isolated darker patch of Fig. 6.2(a) still yields fine Debye rings. It might be argued that the alteration of dark and light patches in, say, Fig. 6.2(b) is reminiscent of spinodal decomposition in glasses where the Te crystallization has followed liquid-liquid separation into a Te enriched glass (or liquid). We rule this out simply because at  $120^{\circ}\text{ C}$ ,  $130^{\circ}\text{ C}$  and  $140^{\circ}\text{ C}$  we have consistently noted heterogeneous interface crystallization in samples which show no crystallization throughout their thickness. (We have in other sections discussed why the variation in  $T_g$  with percentage Ge militates against phase separation in these glasses.)

In Figures 6.3(a) and 6.3(b), we see the structure of the chalcogenides annealed at  $275^{\circ}\text{ C}$  for 10 minutes at low magnification. Figures 6.4(a) and 6.4(b) show much higher mag. shots of the same samples. This sequence demonstrates the dendritic morphology noted earlier.

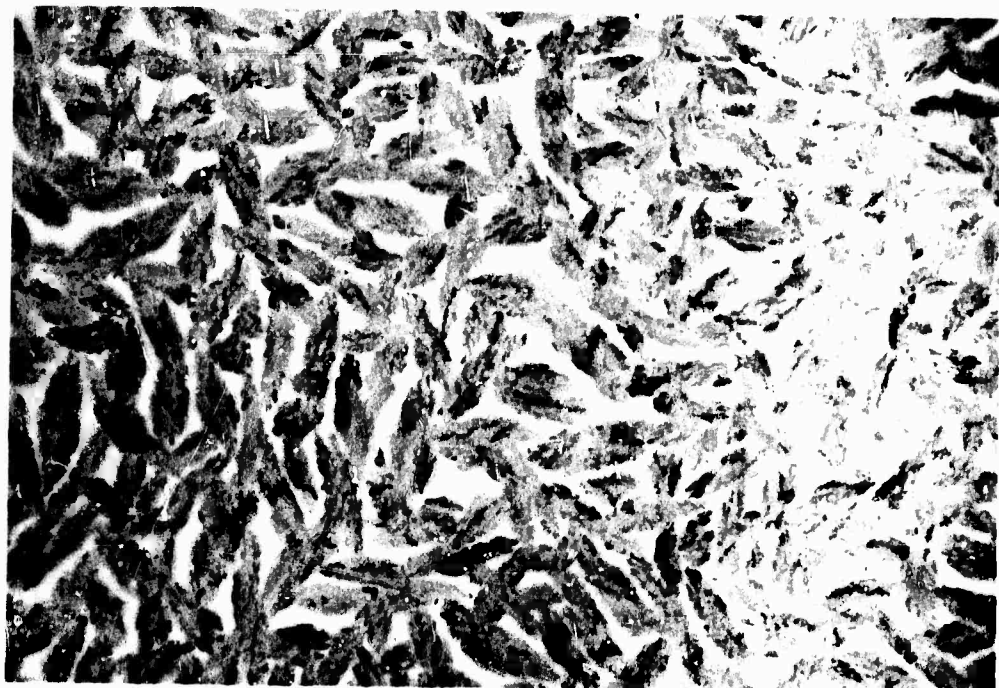


Figure 6.3 (a) 4,700X TEM photo of  $\text{Ge}_{15}\text{Te}_{81}\text{Sb}_2\text{S}_2$  annealed at  $275^\circ\text{C}$  for 10 minutes.



Figure 6.3 (b) 12,100X TEM photo of  $\text{Ge}_{17}\text{Te}_{83}$  annealed at  $275^\circ\text{C}$  for 10 minutes.



Figure 6.4 (a) 33,600X TEM photo (same as Figure 6.3 (a))

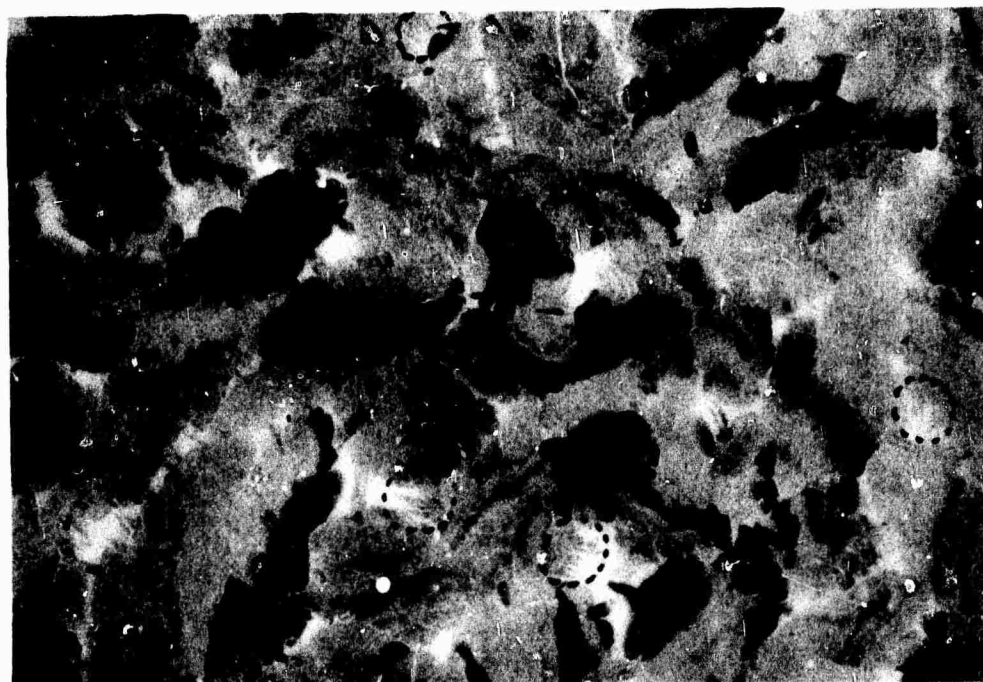


Figure 6.4 (b) 105,000X TEM photo (same as Figure 6.3 (b))

At 275° C, especially in the Sb, S containing glass, the dendrites are quite apparent and contrast greatly (via both diffraction contrast and overall electron transparency) with the Ge rich interdendritic glass. In fact  $\mu$ -chemical analysis of this same film shows that, averaged over a single dendrite arm, there is a 30% increase in Te content over the white (more transparent) glass between the dendrite arms. This fine scale analysis is possible only in the SEM using a solid-state detection system to collect the emitted X-rays from the small (~ 500 Å in diameter) X-ray volume. The distinction between the 140° C and 275° C Te morphologies is simply a result of the increased ability for dendrite arms to penetrate the glass in front of them. The scale inside a singly nucleated arm (with its "deltas" and "rivulets") is still quite fine and there are interdendritic glass threads visible in Fig. 6.4(a) that are ~ 25 Å in width.

Even though each dendrite and its branches comes from a single nucleus, the temperature at 275° C is still sufficiently low to yield a large mosaic spread in Te crystallite orientations which accounts for the very fine scale speckling of the arms. The dark bands arise from regions of similar enough orientation to diffract out of the objective

aperture. Figure 6.5(a) and 6.5(b) show a micrograph and its selected area diffraction pattern from a dark piece of one Te dendrite indicated by the circular end of the pointer. That dark region seems all to be nearly of one orientation - namely the (010) of the hexagonal representation of the Te trigonal structure with many unallowed reflections brought about by simple double diffraction. For example, 001 is obtained by the combination (101) +  $(\bar{1}00)$  or (102) +  $(\bar{1}0\bar{1})$ . Both (010) and (001) were quite frequent orientations.

Figures 6.6(a) and 6.6(b) are from equally large selected areas of Figs. 6.3(a) and 6.3(b). Figure 6.6(a) is obviously representative of a larger grained sample as expected from the micrographs. In addition, both figures show a prominent Debye ring for Te(001) (and, to a lesser extent, for Te (002)) which is not a normally allowed Te reflection. We have also noted this electron reflection in fairly large grained pure Te and believe it to arise, even in the powder pattern, from double diffraction. It is never observed in the X-ray diffraction pattern of either of these crystallized chalcogenides or pure Te. It did appear as a strong spot in Fig. 6.5(b) - again, as we suggested, presumably because of strong multiple Bragg scattering.



Figure 6.5 (a) 33,600X TEM photo of  $\text{Ge}_{15}\text{Te}_{81}\text{Sb}_2\text{S}_2$  annealed at  $275^\circ\text{C}$  for 10 minutes.

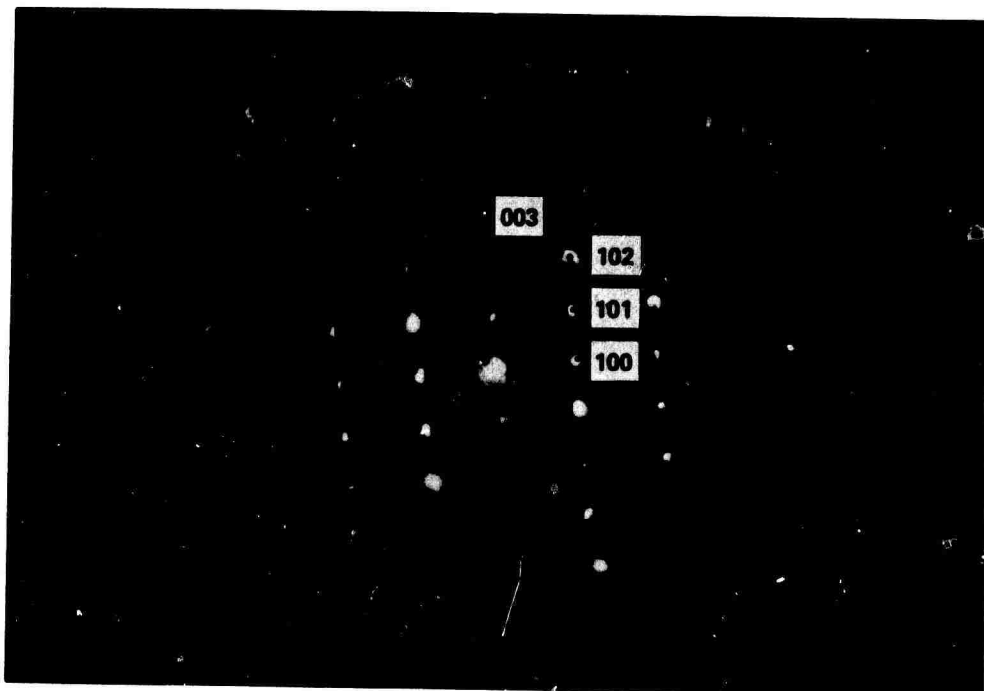


Figure 6.5 (b) Selected area diffraction from one singly oriented portion (see pointer) of dendrite arm of 6.5 (a). The orientation is (010).

In addition to the above artifacts, however, Fig. 6.6(b) shows definitely the  $\bar{1}11$  (weak) and the 200 reflection of GeTe. The former appears between the first two strong rings and the latter just at the outer edge of the second (101) ring. In other words, the simple eutectic composition  $Ge_{17}Te_{83}$  appears not only to have a much smaller Te crystallite size but also to permit the crystallization of GeTe more easily. This distinction can be seen in the micrographs of Figs. 6.3 and 6.4. The  $Ge_{15}Te_{81}Sb_2S_2$  has a higher volume fraction of interdendritic glass and no evidence at all of interdendritic crystallization. The volume of glass in  $Ge_{17}Te_{83}$  is substantially less and this can easily be attributed to interdendritic crystallization which is seen as a feathering in 6.3(b) and as both a filling in of the tiny "rivulets" in 6.4(b) and a distinct lamellar-type eutectic crystallization where the glass once was. A few of these regions are outlined with dotted circles. The lamella spacing is of the order of 100 - 200 Å which is just the GeTe crystallite size observed in the X-ray diffraction study at 275° C.

It was convenient at this stage to produce a rapid beam heating of the samples over a roughly circular area of about 20 microns in diameter. Figure 6.7 shows the

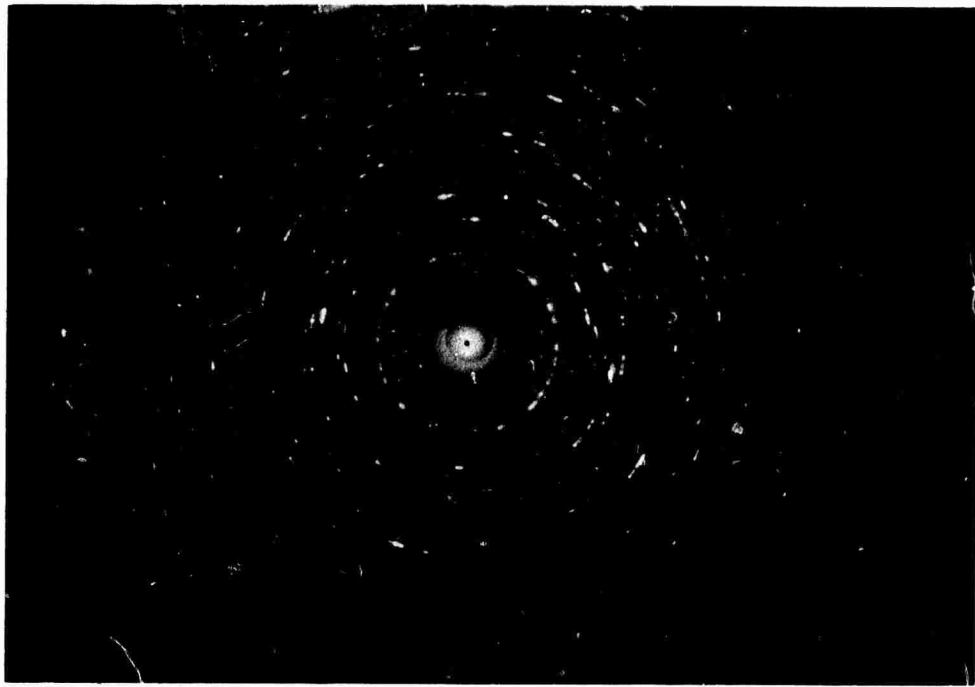


Figure 6.6 (a) SAD from Figure 6.3 (a) showing only Te pattern

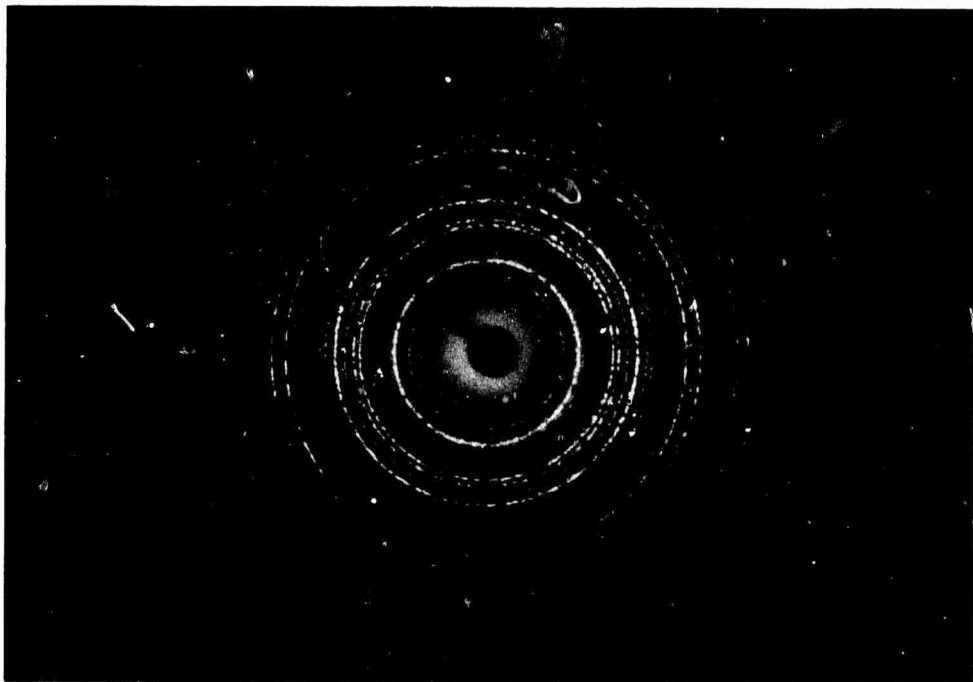


Figure 6.6 (b) SAD from Figure 6.3 (b) showing Te and GeTe

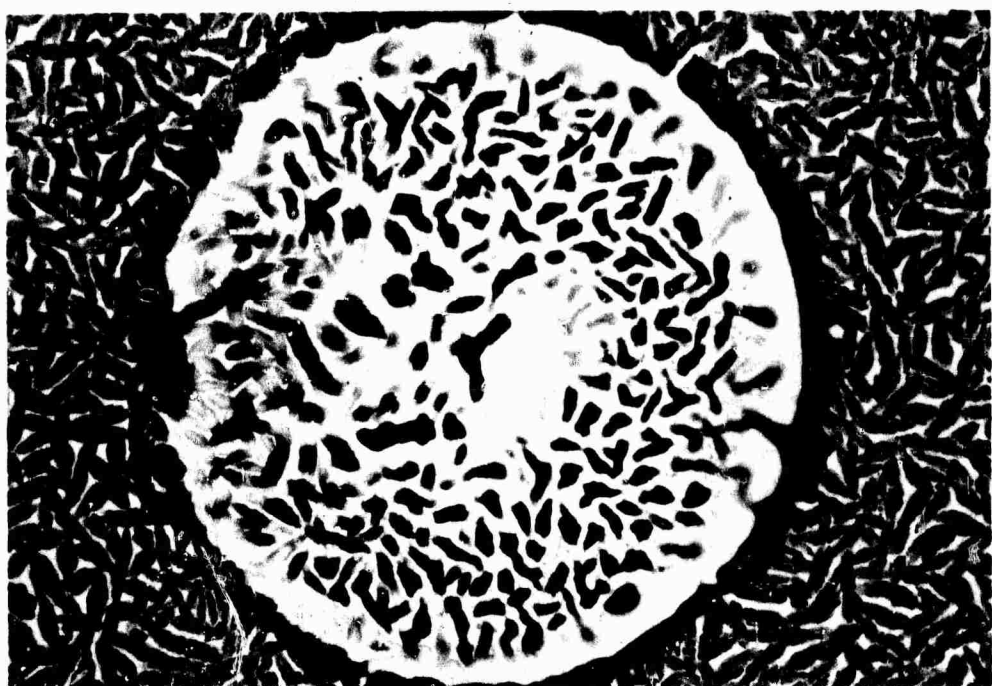


Figure 6.7 (a) Electron beam heated region of Figure 6.3 (a) mag. 5000X



Figure 6.7 (b) Same as 6.7 (a) but at 33,600X

rather dramatic results for  $Ge_{15}Te_{81}Sb_2S_2$ . Away from the electron beam pulsed area there is no change. In the center - as verified by electron diffraction - the thin film has revitrified and is amorphous again albeit severely rumpled and "balled-up" on the amorphous carbon coated surface of the microscope grid. It apparently does not wet this surface well and thus both "balls-up" in the center and forms a characteristic lip at the edge (the dark rim). Still in the irradiated region but nearer the edge, we note a weak but definite replication of the original dendrites in the amorphous material. This was verified by diffraction and is caused either by evaporation of Te to leave the much more viscous Ge rich glass as a template or by the incomplete redissolving of the dendrite and glass.

At the boundary of the circle, we can see the effects of a pulse anneal on the dendrites. There appears to be little coarsening again because of the viscous glass but the dendrites become markedly more perfect single crystals. The low angle, or mosaic, boundaries anneal out, the rivulets of glass assume a more spherical shape (circles in Fig. 6.7(b)) and extinction contours appear in the Te at the right hand side of Fig. 6.7(b).

In  $\text{Ge}_{17}\text{Te}_{83}$  where the GeTe has started to precipitate and where the grain size is much smaller, there is much more pronounced Te coarsening on electron beam heating. We can produce a very similar result merely by taking a sample of  $\text{Ge}_{15}\text{Te}_{81}\text{Sb}_2\text{S}_2$  and heating it to, say,  $340^\circ\text{C}$  after a 5 hour anneal at  $130^\circ\text{C}$ . The latter induced a morphology very similar to that of Fig. 6.2(a), but with almost no visible glass between the darker crystalline areas. After heating to  $340^\circ\text{C}$  for 20 minutes, the micro-structure in Fig. 6.8(a) was obtained showing very little, if any, glass and a coarser grain structure than in 6.2(a). In Fig. 6.8(b), this sample is electron beam heated and the enormous coarsening and melioration of the Te dendrite crystals is obvious. Again, the dark lines through the large crystals at the edge of the beam heated region are bend and extinction contours.

### 6.3.3 Electron-Beam $\mu$ -Probe Results

Because we noticed such a pronounced distinction between  $\text{Ge}_{17}\text{Te}_{83}$  and  $\text{Ge}_{15}\text{Te}_{81}\text{Sb}_2\text{S}_2$  in their crystallization behavior, it seemed profitable to explore the chemical differences in the bulk equilibrium crystallized glasses. The binary glass, of course, crystallizes finally to Te and GeTe. This quaternary certainly contains these phases into which

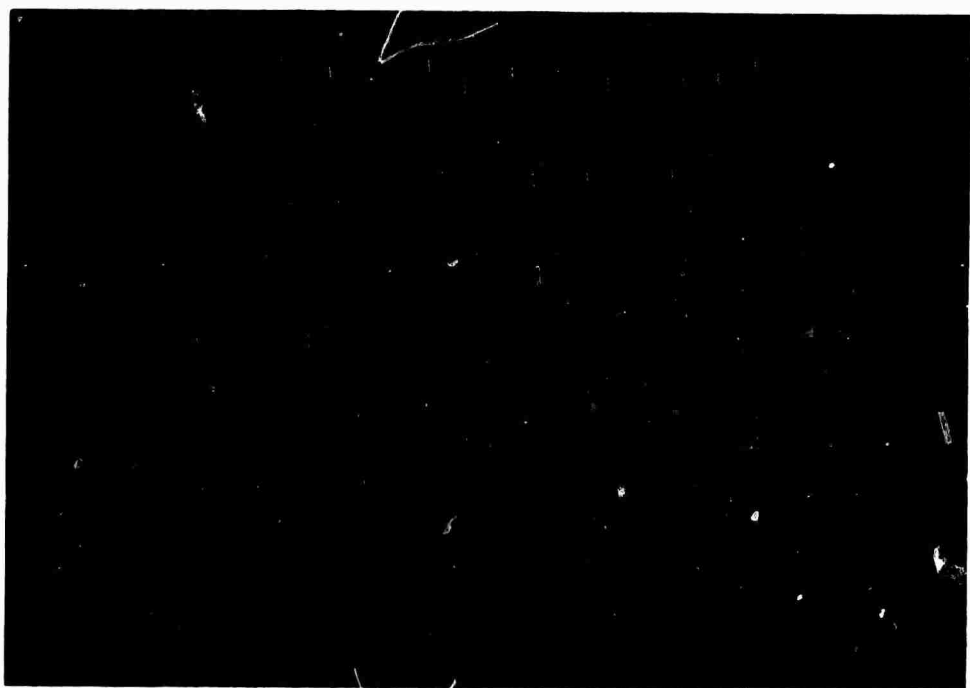


Figure 6.8 (a) 36,000 TEM photo of  $\text{Ga}_{15}\text{Ta}_8\text{Sb}_2\text{S}_2$  annealed at  $130^\circ\text{C}$  for 5 hours followed by  $340^\circ\text{C}$  for 20 minutes.

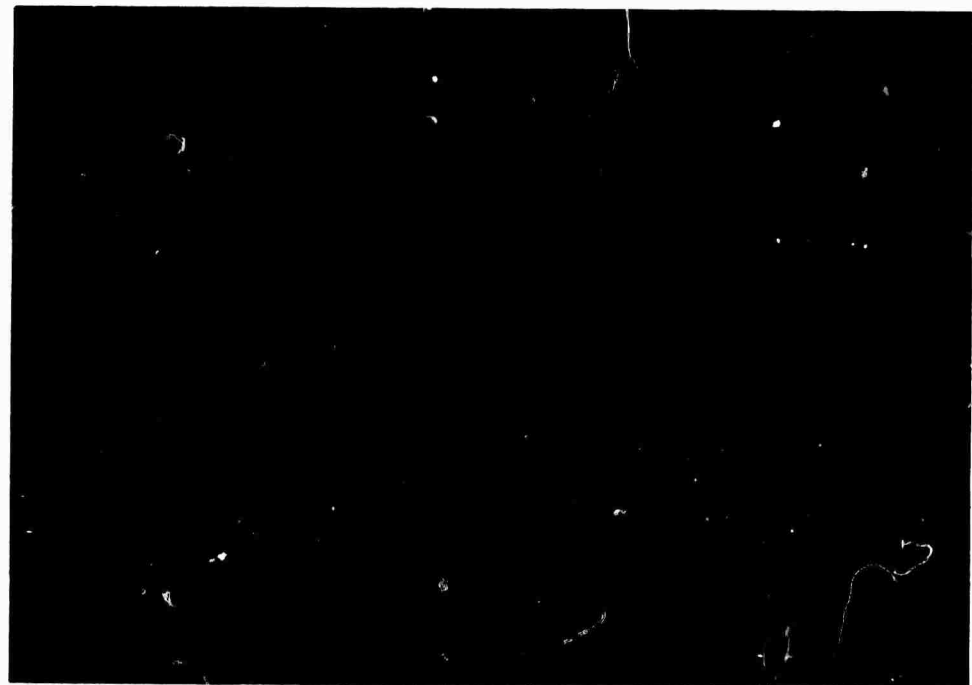


Figure 6.8 (b) 7,200X mag. of electron beam-heated area of above

are presumably dissolved either (or both) S and Sb.

In Fig. 6.9 are the results of  $\mu$ -probe traces across the face of a polished and (unfortunately) lightly etched bulk crystallized  $Ge_{15}Te_{81}Sb_2S_2$  glass. In these 1000X back-scatter electron micrographs, the dark needles are the telluride phase and the white structureless background is tellurium. These needles are seen both on edge and on the side and may actually either be platelets viewed at different angles or even perhaps two distinct crystalline phases. We are currently exploring these and related points in greater detail. Suffice it to note here that where the Ge  $\mu$ -probe X-ray intensity is strong along the scan line (indicated by the white trace cutting through the particles) the Sb is also strongest, except for the flat plate at the right where there may be etch effects or which may indeed be a different, Sb-free, telluride phase. In a sense, it is not surprising that Sb goes along with GeTe because of a similarity in crystalline-structures. It would seem, in addition, reasoning from the TEM results, that its presence in the glass might inhibit the formation of this telluride.

#### 6.3.4 Summary and Conclusions

The major conclusions of this part of our structural analysis of the crystallization of memory glasses can be

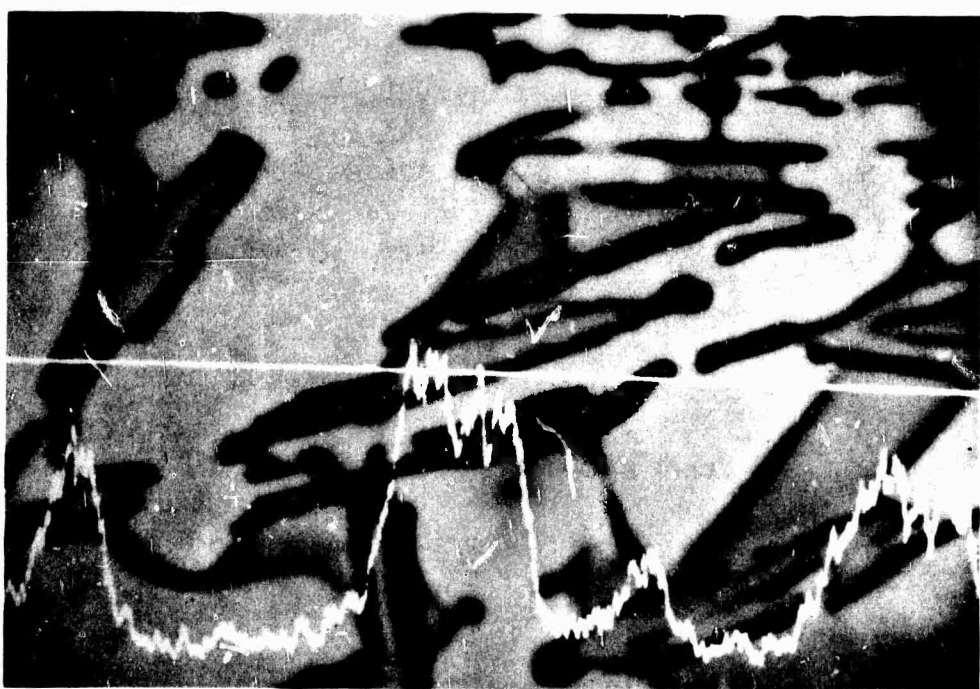


Figure 6.9 (a) Electron beam  $\mu$ -probe X-ray trace of Ge in bulk crystallized  $\text{Ge}_{15}\text{Te}_{81}\text{Sb}_2\text{S}_2$ .  
Back-scatter electron micrograph at 1000X.

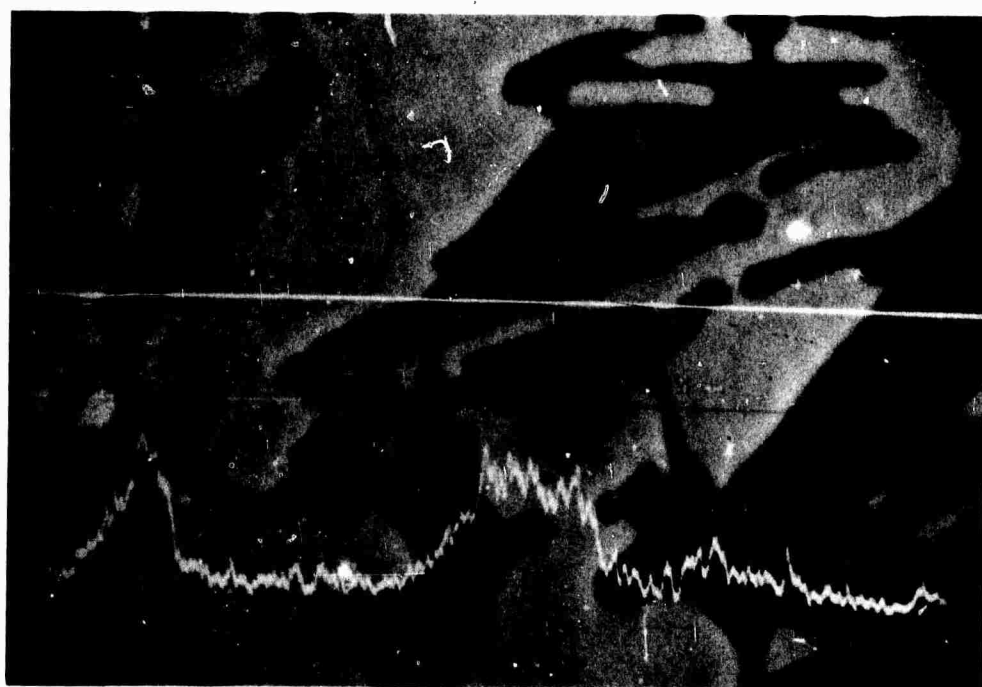


Figure 6.9 (b) As above, but Sb trace.

listed:

1. The eutectic Ge-Te glass (with or without Sb, S) does not homogeneously phase separate prior to crystallization. The very earliest detectable crystallization above  $T_g$  is invariably heterogeneous.
2. These glasses tend to yield a very large volume fraction of crystalline Te (and no GeTe) when annealed for a long time just above  $T_g$ . This is not inconsistent with the X-ray results if one again recalls that the nucleation is heterogeneous and cannot, at low temperatures, proceed well into the thickness of a  $2.0 \mu$  film. There seems to be little particle coarsening at low temperatures (see Table 6.1) but the Sb, S alloy forms larger Te crystals than the pure  $Ge_{17}Te_{83}$ . Just how this is controlled by the Sb, S has not been resolved. Perhaps it is merely a simple matter of increased nucleation rate without Sb, S.
3. At the higher temperature of  $275^\circ C$ , the Sb, S alloy again has larger crystallites of Te but after a 10 minute anneal has still shown no evidence of GeTe. Both glasses crystallize Te out dendritically but the  $Ge_{17}Te_{83}$  shows pro-

nounced GeTe formation as interdendritic eutectic lamellae of 100-200 Å.

4. The  $Ge_{15}Te_{81}Sb_2S_2$  seems to show a lower volume fraction Te at 275° C than at 140° C. (Compare 6.3(a) with 6.2(a)). At 275° C, the very rough estimate of 50% Te from Section 6.1 seems therefore not unreasonable. The conjecture of an increased tendency to develop more Te at lower temperatures is at least not violated by these results.

The Sb is associated with the telluride in the equilibrium crystallized  $Ge_{15}Te_{81}Sb_2S_2$  glass.

## 7. PROPERTIES OF CHALCOGENIDE LIQUIDS

7.1 Liquid Conductivity and Heat Capacity

We have continued the liquid state heat capacity studies reported for the  $\text{Te}_{83}\text{Ge}_{17}$  alloy in the first Semiannual Report of this contact. New alloys studied include pure Te,  $\text{Te}_{90}\text{Ge}_{10}$ ,  $\text{Te}_{78}\text{Ge}_{22}$ ,  $\text{Te}_{75}\text{Ge}_{15}\text{As}_{10}$ ,  $\text{Te}_{40}\text{As}_{60}$ ,  $\text{Te}_{60}\text{Ge}_{13}\text{As}_{20}\text{S}_2$ ,  $\text{Te}_{81}\text{Ge}_{15}\text{Sb}_2\text{S}_2$  and  $\text{Te}_{70}\text{Se}_{30}$ .

Pure Te,  $\text{Te}_{90}\text{Ge}_{10}$ ,  $\text{Te}_{60}\text{As}_{40}$  and  $\text{Te}_{70}\text{Se}_{30}$  were chosen because their electrical conductivities in the liquid state have been reported.<sup>16,17</sup> In addition, we have measured the electrical conductivity of  $\text{Te}_{81}\text{Ge}_{15}\text{S}_2\text{Sb}_2$  in the same capillary apparatus described in the electromigration studies section of this report. These electrical conductivities are plotted in Fig. 7.1. Note that above  $\sim 450^\circ\text{C}$  all these alloys display uniformly high metallic conductivities of order  $3 \times 10^3 \Omega^{-1}\text{cm}^{-1}$ , with very low apparent activation energies  $\partial(\ln \sigma)/\partial(1/T)$  ranging from  $\sim 0.3$  eV to less than 0.1 eV. However, when these liquids are cooled below  $450^\circ\text{C}$ , the electrical conductivity falls off sharply, with apparent activation energies ranging between 1.2 - 2.0 eV. The widespread occurrence of this phenomenon for liquid alloys containing between 60-100% Te suggested the hypothesis that the large anomalous heat capacity observed for liquid  $\text{Te}_{83}\text{Ge}_{17}$  between  $374 - 425^\circ\text{C}$  is associated with an electronic transition from a low temperature

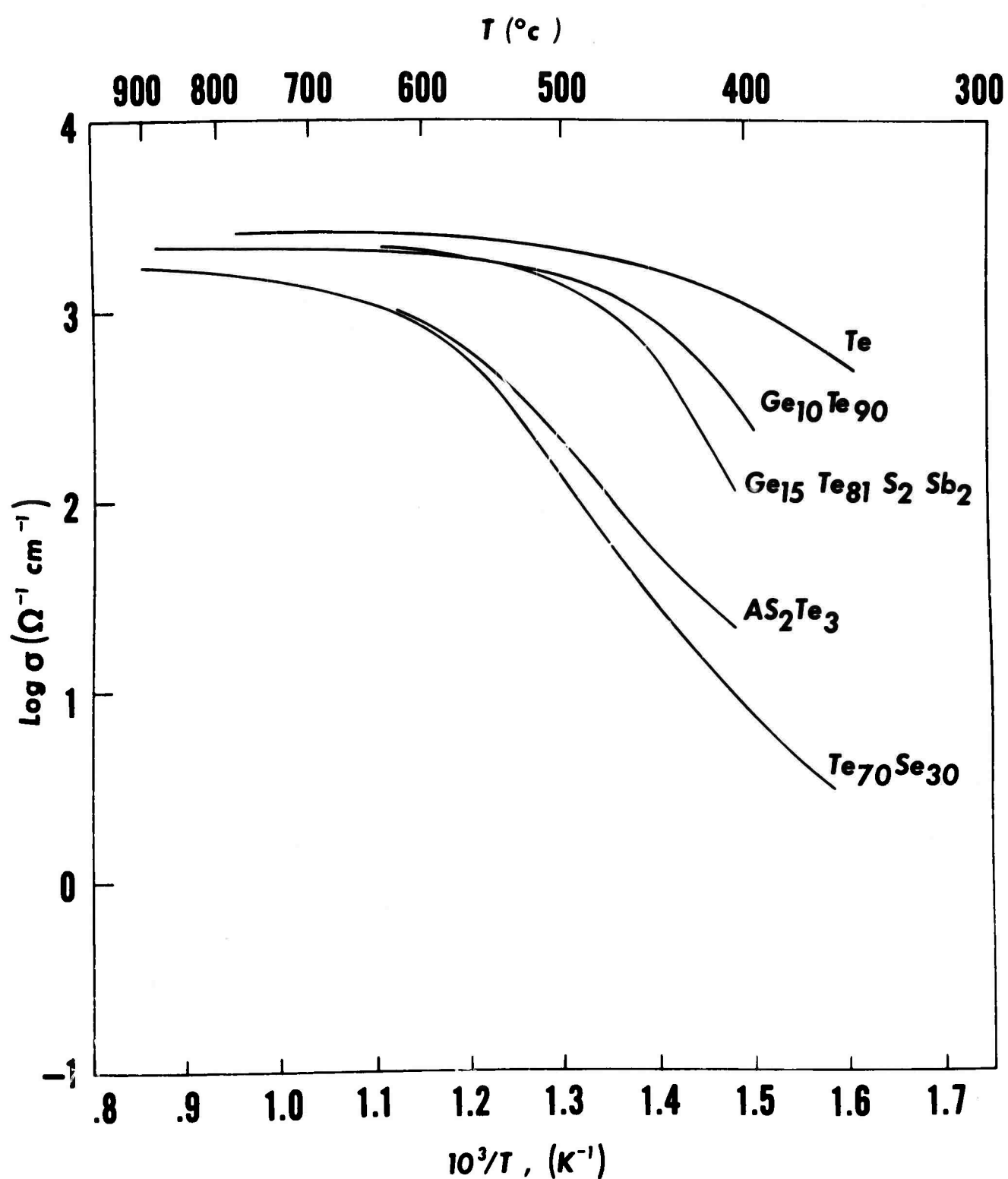


Fig. 7.1

semiconducting liquid to a high temperature metallic liquid. Such a transition might involve an increase in the average coordination number from the glass-like value of  $\sim 2-3$ <sup>18</sup> to the metal-like values of  $\sim 8$  observed for liquid Ge and Si<sup>19</sup>.

A test of this hypothesis is provided by our measurements of the heat capacities of liquid  $\text{Te}_{60}\text{As}_{40}$ , Te, and  $\text{Te}_{70}\text{Se}_{30}$  plotted in Fig. 7.2. Whereas all of these alloys display the electronic "transition" as indicated by the unusually large slope of the Arrhenius plot ( $\log \sigma$  vs  $1/T$ ) in the vicinity of  $400^\circ \text{C}$ , none of them display abnormally large heat capacities in this same temperature region. In fact, the complete absence of such an effect appears to rule out both the hypothesis that the "electronic transition" has a large concomitant thermal component, and the hypothesis that the change in the conductivity activation energy is accompanied by a change in nearest neighbor atomic configuration. A dramatic change in coordination number over a relatively narrow temperature range would invariably be accompanied by a large thermal effect analogous to the latent heat of a first order phase change.

On the other hand, the presence of the heat capacity maximum has been observed for all the germanium bearing liquid alloys we have measured as shown in Fig. 7.2. Note that the magnitude of the peak, i.e. the excess enthalpy, scales roughly with Ge content

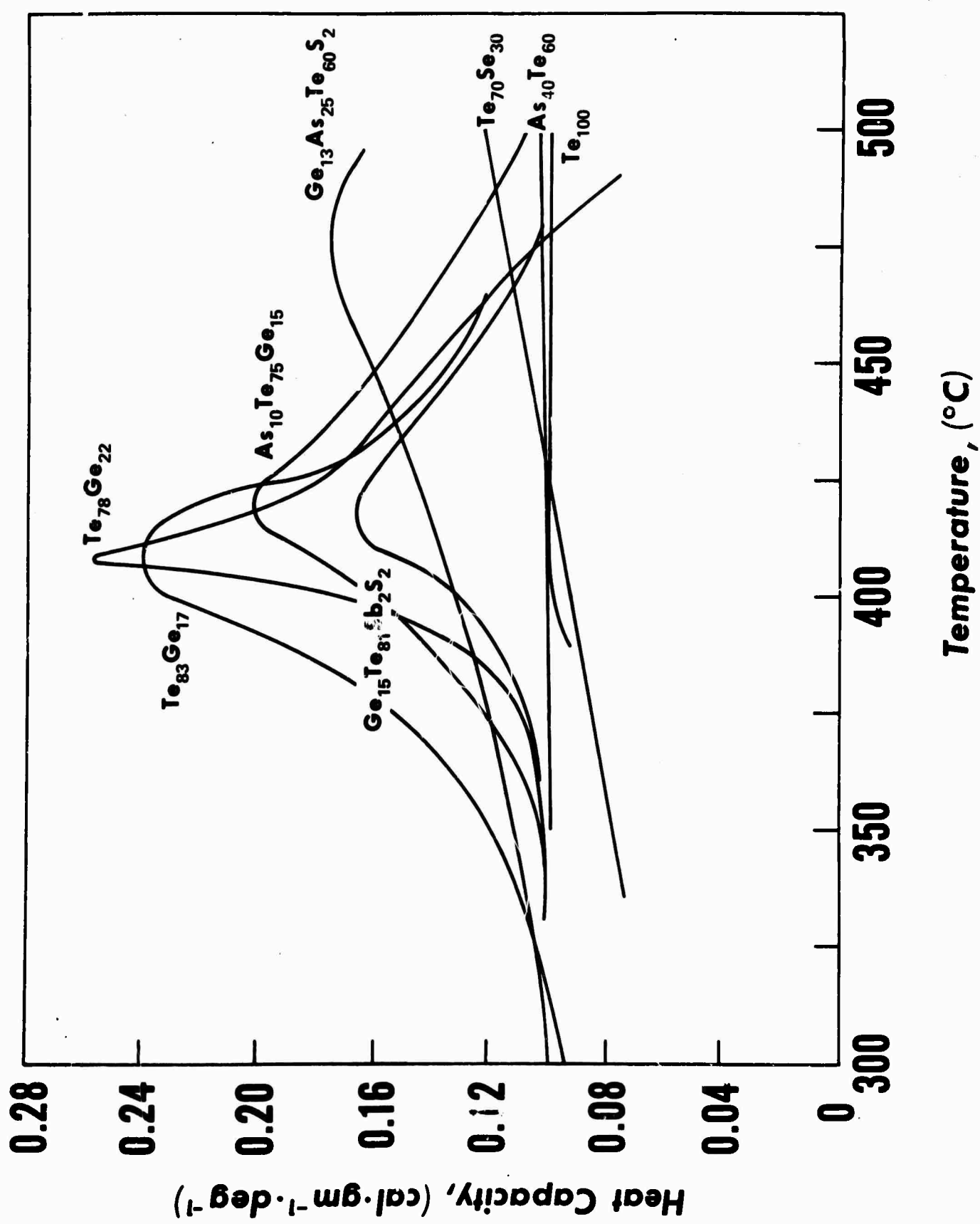


Fig. 7.2

while the temperature of the peak shifts only slightly with composition. The peak for  $Ge_{13}As_{25}Te_{60}S_2$  is exceptional in that it is far broader and occurs at a higher temperature than for the other liquids. Similar alloys<sup>17</sup> manifest a broader "electronic transition" which is also shifted to higher temperatures.

Fortunately an alternative model is available which accounts in qualitative terms for the observed association of the liquid heat capacity anomaly with the concentration of germanium rather than with the rapid changes in electrical properties. This model is based on our previously reported<sup>15</sup> observation that Ge-Te glasses display an ordering tendency as indicated by the sharp maximum in  $T_g$  at the composition  $GeTe_2$ . This maximum was taken as a strong indication that the  $GeTe_2$  glassy structure contains essentially only Ge-Te covalent bonds, while As-Te glasses show no such singularity at the  $As_2Te_3$  composition, and thus were assumed to be a more random mixture of the possible covalent bonds. Thus the smeared out thermal transition in liquid Te alloys containing Ge appears to be a disordering reaction directly related to the ordering tendency observed at lower temperatures. A confirmation of this prediction that Te-Ge liquids are disordered above  $\sim 500^\circ C$  is provided by observations of liquid state electrical conductivity<sup>20</sup> which display no singularity at the  $GeTe_2$  composition. Such a singularity would be expected if the high temperature liquid structure

contained only ordered clusters of completely cross-linked  $\text{GeTe}_4$  tetrahedra which characterize the glass and low temperature liquid structure.

The concurrence of the disordering reaction temperature and the smeared out conductivity transformation temperature for these Te-Ge alloys need not be considered as coincidental but rather follows from simplified considerations of electronic structure. In the semiconducting liquid state of Te-rich alloys, up to, say  $300^\circ \text{ C}$ , most of the valence electrons participate in covalent bonds and few exist in extended conduction band states. However, as more and more electrons populate these extended states their presence becomes a significant perturbation on the bond structure, reducing the barrier for further covalent bond dissociation, lowering the effective electrical gap, and resulting in the characteristic increase in the slope of Arrhenius plots in this temperature range. In this view the smeared out "semiconductor" - "metal" transformation is essentially a cooperative thermal dissociation of covalent bonds, promoting, at high temperatures, a large concentration of the valence electrons to extended conduction band states. Thus the high temperature liquid phase seems better described as a degenerate semiconductor than as a metal.

In the process of exciting these valence electrons to extended conduction band states many of the chemical properties of the

covalent bonds are changed. In particular the nearest neighbor coordination is no longer primarily affected by the enthalpy difference:

$$\Delta H = 2\text{Ge-Te} - (\text{Te-Te} + \text{Ge-Ge}) \quad 7.1$$

since this enthalpy difference applies to the potential energy of electrons residing in covalent bonds. Thus, as the electrons in these bonds become progressively dissociated at higher temperatures, the atoms become free to arrange themselves in configurations which maximize entropy, i.e., they disorder.

Equation 7.1 is crucial for predicting this ordering tendency in chalcogenide glasses and liquids at low temperatures. In general most binary systems, A-B, will tend to order due to ionic contributions from the A-B bonds. However, when one component forms stronger homopolar bonds than heteropolar bonds (As-As vs. As-Te bonds in As-Te system), then the ordering tendency may be negligible.

A schematic diagram which applies the order-disorder model specifically for amorphous phases in the GeTe systems is shown in Fig. 7.3. This ternary diagram expresses the concentration of all the possible covalent bonds, Te-Te, Ge-Te and Ge-Ge, as a function of composition. Each line represents a single Te-Ge ratio and thus a single composition in the Ge-Te binary system,

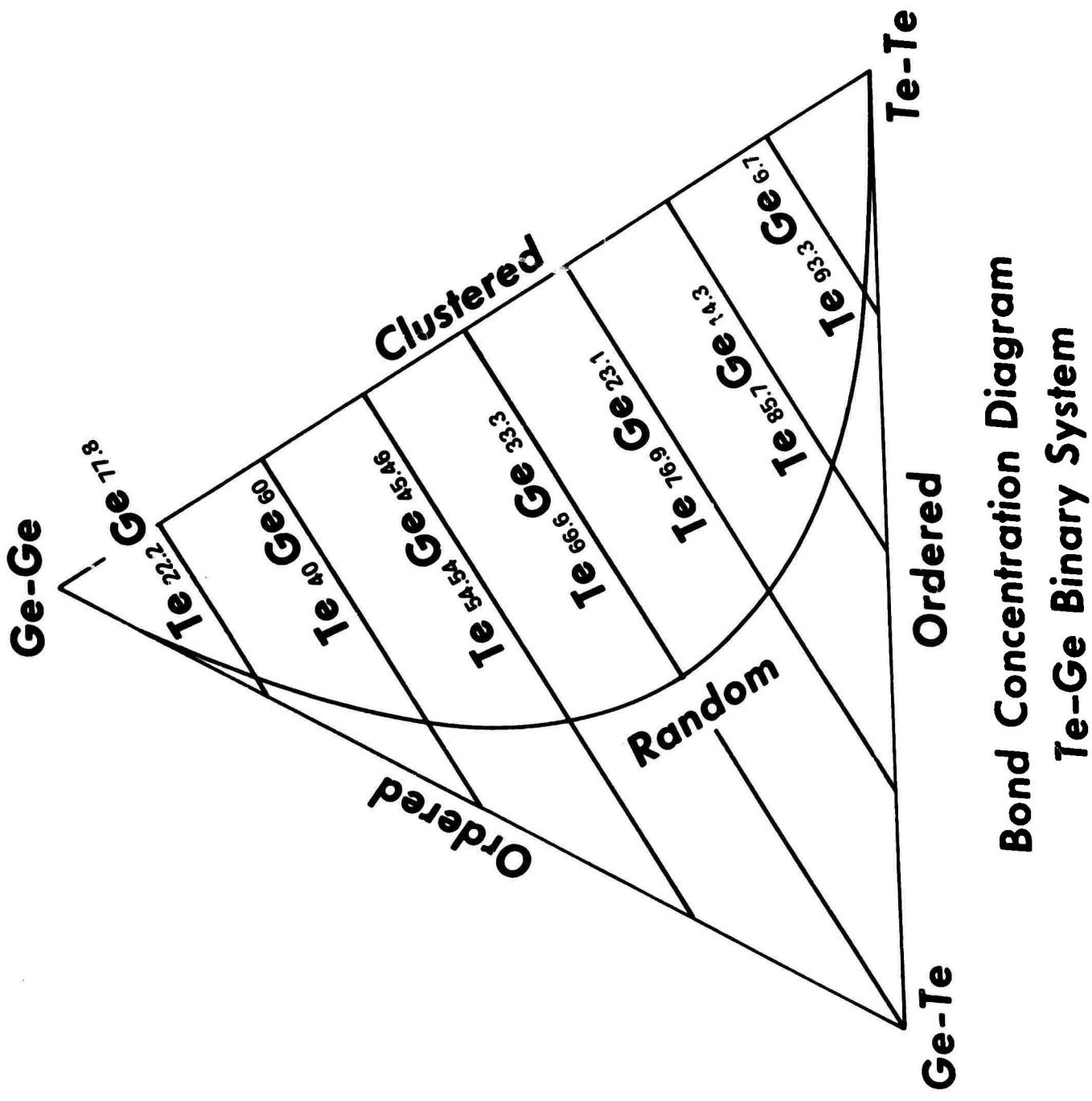


Fig. 7.3

and each point on a given line represents a possible ratio of bond concentrations. Points along the line connecting Ge-Ge and Te-Te correspond to structures which contain no Te-Ge bonds, i.e., the case of complete phase separation. Points along the lines connecting Ge-Te to Te-Te and to Ge-Ge correspond to completely ordered structures, i.e., the model proposed herein for glasses and low temperature liquids between pure Te and  $\text{GeTe}_2$ . A dotted line in the middle of the triangle running from Ge-Ge to Te-Te and intersecting every composition line corresponds schematically to random structures whose concentration of Ge-Ge, Te-Te and Ge-Te bonds is controlled entirely by entropic considerations, i.e., the model proposed herein for liquid alloys between Te and  $\text{GeTe}_2$  at high temperatures.

While the series of structures described by points along the Ge-Ge to Te-Te boundary are of necessity phase separated due to the absence of any interconnecting Ge-Te bonds, it does not follow that structures lying along the Ge-Ge to Ge-Te to Te-Te "ordered" boundary are necessarily homogeneous. In fact, a counter example exists<sup>21</sup> in the  $\text{GeO}_2$  - Ge system for which a fully ordered model (i.e., no O-O bonds) strongly suggests itself, and yet homogeneous glasses in this system phase separate just above their glass transition temperature releasing a large exothermic heat of unmixing. Note, however, that the bond fraction model does not consider

bond location or topology; it only describes the structure in terms of relative bond concentrations. For the Ge- $\text{GeO}_2$  glasses, phase separation is not accompanied by any change in the Ge-Ge/Ge-O bond concentration ratio but merely by the segregation of Ge-Ge bonds away from Ge-O bonds forming amorphous Ge and amorphous  $\text{GeO}_2$  as the separated phases.

Thus the argument for the absence of phase separation for glasses and low temperature liquids between Te and  $\text{GeTe}_2$  relies not on the occurrence of a  $T_g$  singularity at  $\text{GeTe}_2$  but rather on the smooth increase in  $T_g$  with composition as Ge is added to pure Te up to the  $\text{GeTe}_2$  composition. In fact the existence of phase separation in the range of composition between  $\text{GeTe}_2$  and Ge has not been examined experimentally or theoretically and cannot, therefore, be ruled out at present.

## 7.2 Electromigration in Liquid $\text{Te}_{85}\text{Ge}_{15}$ at $550^{\circ}\text{C}$

### 7.2.1 Introduction

Memory switching compositions based on the composition

$\text{Ge}_{15}\text{Te}_{85}$  have been reported and constitute an important class of materials for this application. Fabrication of random access two dimensional arrays of memory switches currently require diodes in series with the OMS devices to provide electrical isolation of individual bits and unipolar current for write, erase and read operations. A fundamental concern in such a high current environment as a memory filament in an OMS device is the role of electromigration in fractionating the active material. We have studied this effect in the pure binary alloy  $\text{Te}_{85}\text{Ge}_{15}$  in order to evaluate the sign and magnitude of such current induced atomic diffusion processes at high temperatures.

The existence of a strong net force on an impurity ion in a liquid metal caused by an applied electric field has been reported by Gerardin<sup>22</sup> in 1861. Manglesdorf<sup>23</sup> phenomenologically described the force as having two components; an electrostatic force exerted by an applied field on the ion, and an electron drag arising from the exchange of momentum between electrons and ions. The amount of momentum each ion species receives has been shown to depend primarily on their electron ion scattering cross sections<sup>24</sup> and, since electromigration in liquids is inherently a competitive phenomenon, the rate of separation depends on the difference in the scattering cross sections.

Quantitative study of electromigration and diffusion requires knowledge of the atomic density, C, of each species in the alloy as well as atomic composition. In this chapter, section 7.2.1 describes a method for determination of atomic density and atomic composition. Section 7.2.3 describes the experimental considerations. Section 7.2.4 contains the experimental data on the  $Ge_{15}Te_{85}$  reservoir alloy and 7.2.5 contains a discussion of the results.

#### 7.2.2. Determination of Atomic Density and Composition

Using the technique developed by Epstein<sup>25</sup>, we have studied electromigration by immersing capillaries with one open end and an electrode sealed into the other end in a large reservoir of the alloy to be studied. Current is passed from one electrode to the other depleting one atomic component from one capillary and accumulating it in the other.

The apparatus is shown in Fig. 7.4. In operation, three pyrex capillaries approximately one centimeter long with a tungsten or a molybdenum wire sealed in one end (the other end being left open), are fastened to the bottom of the sample holder. This apparatus is then inserted inside the outer tube and the system evacuated. The alloy is heated to above its melting point after being back filled with argon to prevent vapor transport under prolonged vacuum. When the alloy has become liquid,

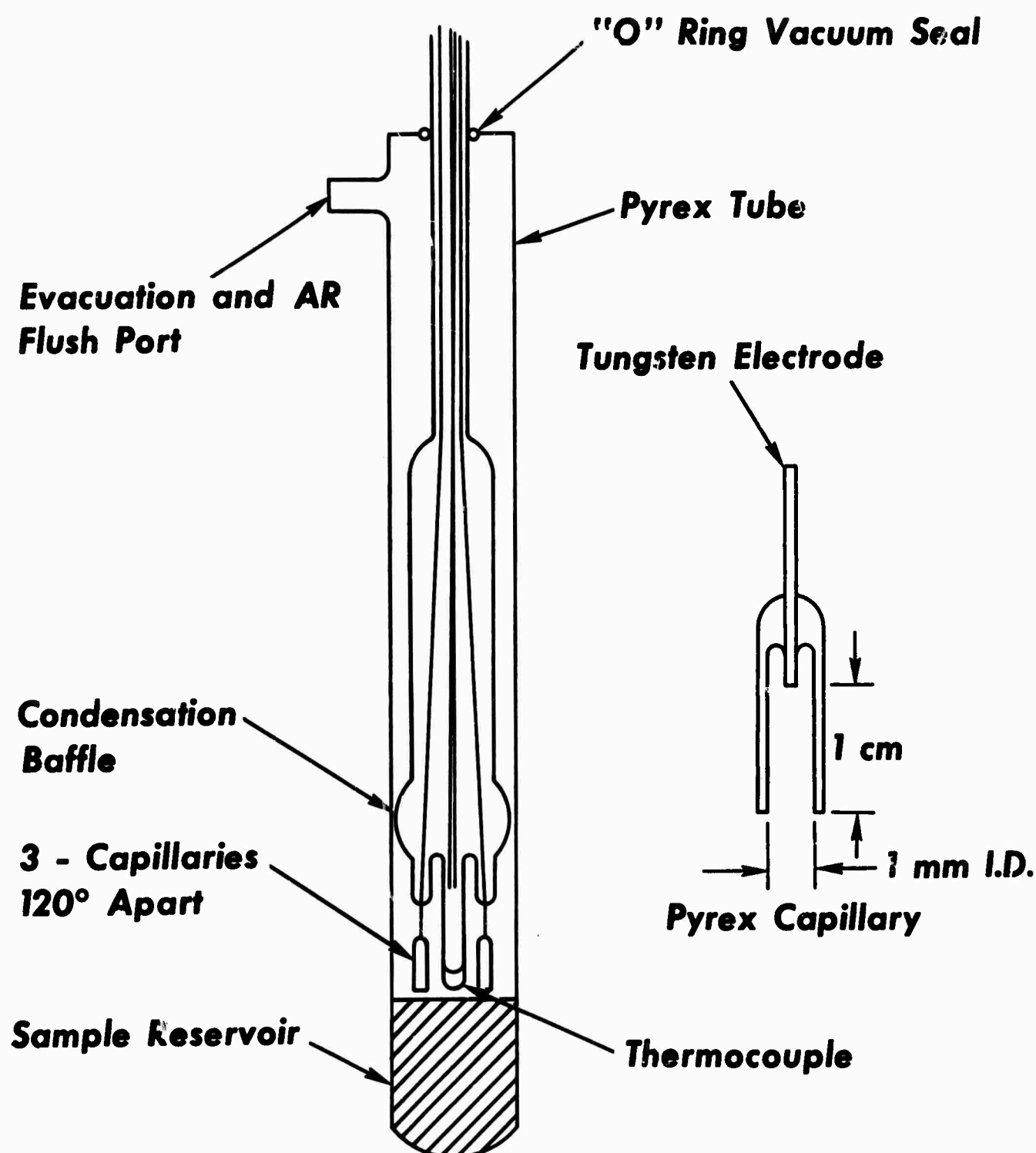


Fig. 7.4

and reached the final temperature, the system is again briefly evacuated. The capillaries are immersed into the liquid nearly one centimeter, and the sample apparatus is again back filled with argon to fill the capillaries. Appropriate currents are run through the various capillaries until they accumulate or deplete any atomic components which may be undergoing electromigration. The third, neutral, capillary is used as a comparison blank.

Neutron activation analysis performed at the University of Michigan was used to measure changes in chemical composition. The technique allows a rapid and reasonably accurate measurement of the ratio of Ge atoms to Te atoms averaged over a complete sample. Sectioning of a sample allows composition profiles to be determined.

A significant advantage of the Epstein apparatus<sup>25</sup> is that the orifice composition is held at the reservoir composition. This allows a study of each atom species in the constant composition reservoir alloy by measuring the flux of atoms through each capillary orifice. The capillary will act as an atom trap to confine the integrated atomic flux. Subsequent analysis provides evaluation of diffusion and electromigration parameters in the reservoir composition. Composition profiles obtained from capillary sections provide information about the composition dependence of these parameters.

In an equilibrium liquid alloy, density is well defined as a function of composition and temperature. Since our experiments are performed in the liquid state, the accumulation or depletion of Ge from a capillary will produce opposite transport of Te in such a way that the proper value of density is preserved in each volume element. In the  $Ge_x Te_{1-x}$  system at  $550^\circ C$ , the liquid density is  $5.65 \pm 0.10 \text{ g/cm}^3$  for  $0 \leq x \leq .35$ , and the density of crystalline GeTe is  $6.02 \pm .03 \text{ g/cm}^3$ .<sup>21</sup> To calculate the atomic densities of Ge and Te in the alloy we therefore assume to first order, that the liquid density is constant:  $\delta = 5.65 \text{ g/cm}^3$ .

The atomic density of germanium  $C_{Ge}$ , and tellurium,  $C_{Te}$  is obtained by writing the mass density of the sample equal to the mass density of the sum of the components; i.e.

$$\bar{C}_{Ge} M_{Ge} + \bar{C}_{Te} M_{Te} = \delta \quad \text{Eq. 7.2}$$

where  $\bar{C}_{Ge}$  = at/cm<sup>3</sup> average atomic concentration of Ge

$\bar{C}_{Te}$  = at/cm<sup>3</sup> average atomic concentration of Te

$M_{Ge}$  = mass of germanium atom

$M_{Te}$  = mass of tellurium atom

$\delta = 5.65 \text{ g/cm}^3$ , mass density of the alloy.

Neutron activation analysis produces a number  $\alpha$ , which is

proportional to the ratio of atoms, Ge/Te in the total sample, and therefore,

$$\alpha = \frac{\bar{C}_{Ge}}{\bar{C}_{Te}} \quad \text{Eq. 7.3}$$

Eq. 7.2 and 7.3 may now be solved to provide atomic concentrations of the species in terms of the experimental parameter  $\alpha$ , the ratio of germanium to tellurium atoms.

$$\bar{C}_{Ge} = \delta / (M_{Ge} + M_{Te}/\alpha) \quad \text{Eq. 7.4}$$

$$\bar{C}_{Te} = \delta / ( \alpha M_{Ge} + M_{Te}) \quad \text{Eq. 7.5}$$

The atomic compositions in % are:

$$\%Ge = \bar{C}_{Ge} / (\bar{C}_{Ge} + \bar{C}_{Te}) \quad \text{Eq. 7.6}$$

$$\%Te = \bar{C}_{Te} / (\bar{C}_{Te} + \bar{C}_{Ge}) \quad \text{Eq. 7.7}$$

### 7.2.3 Electromigration - Experimental Considerations

<sup>25</sup> Epstein has shown that in experiments where the field is applied for a short duration of time, atomic migration proceeds at constant velocity throughout the capillary, and the initial concentration change occurs only in the alloy in the immediate region of the electrode. For this case, the flux of germanium atoms in the  $Ge_{15}Te_{85}$  alloy is given by:

$$N_{Ge} = v_{Ge} C_{Ge}^0$$

Eq. 7.8

The zero superscript refers to the reservoir alloy and conditions at the orifice.  $v_{Ge}$  is the velocity and  $C_{Ge}^0$  is the reservoir atomic density of germanium in the 15/85 alloy.

The velocity of the germanium atoms,  $v_{Ge}$ , is related to the diffusivity D by;

$$v_{Ge} = \left(\frac{D}{kT}\right) Z^*E$$

Eq. 7.9

$Z^*E$  is the net force applied to the germanium atom. It is composed of at least two terms: the screened ionic charge of germanium in the alloy, and the electron drag resulting from electron-ion momentum transfer. The net force  $Z^*E$  is defined by the velocity of motion of the germanium atom in the alloy for an applied field E under the assumption that D is the atomic diffusivity of Ge in the alloy.

During electromigration, electrokinetic effects which give rise to stirring within the capillary have been reported.<sup>26</sup> As a result, the diffusivity for back diffusion effects may be dependent on the magnitude of the electric current. This effective diffusivity, called  $D_{eff}$  measured in the electromigration apparatus may be an order of magnitude

greater than the atomic diffusivity,  $D$ . Epstein<sup>25</sup> has also shown that if the electromigration occurs for a very long time, a concentration gradient is displaced to the orifice due to back diffusion. If the back diffusion, including the electrokinetic mixing term, is assumed to obey Ficks Law

$$N = D_{\text{eff}} \frac{dc}{dx} \quad \text{Eq. 7.10}$$

where  $N$  is the atom flux,  $D_{\text{eff}}$  is the effective back diffusivity and  $\frac{dc}{dx}$  is the concentration gradient, then the general flux equation for germanium in the 15% Ge alloy at the capillary orifice can be expressed as:

$$N_{\text{Ge}} = \left( \frac{D}{kT} \right) C_{\text{Ge}}^0 Z^* E - D_{\text{eff}} \frac{dC_{\text{Ge}}}{dx} \bigg|_{x=0} \quad \text{Eq. 7.11}$$

at the low current limit (undefined),  $D_{\text{eff}}$  equals  $D$  so that in the steady state under these conditions,

$$\frac{C_{\text{Ge}}^0}{kT} Z^* E = \frac{dC_{\text{Ge}}}{dx} \quad \text{Eq. 7.12}$$

#### Case A - Evaluation of the atomic velocity at the orifice

For short experiment times, no concentration gradient exists at the orifice. Under this condition, the atomic flux is entirely due to electromigration. The time required for the concentration gradient to reach the orifice has been

given by Kleimann<sup>27</sup> as,

$$\tau_{\text{sat}} = \frac{L^2}{\pi D_{\text{eff}}} \quad \text{Eq. 7.13}$$

where  $\tau_{\text{sat}}$  is the critical time and L is the capillary length.

For experiments run for a duration less than  $\tau_{\text{sat}}$ , the back diffusion term in Eq. 7.2 is negligible and the flux of germanium atoms at the orifice is constant;

$$N_{\text{Ge}} = v_{\text{Ge}}^0 C_{\text{Ge}}^0 \quad \text{Eq. 7.14}$$

The total number of germanium atoms in the capillary after the experiment is the number originally there, plus the number which entered or left through the orifice. Therefore:

at time  $t < \tau_{\text{sat}}$ ,

$$\# \text{ Ge atoms} = C_{\text{Ge}}^0 AL + A \int_0^t v_{\text{Ge}}^0 C_{\text{Ge}}^0 dt \quad \text{Eq. 7.15}$$

where

A is the capillary area

L is the capillary length

$v_{\text{Ge}}^0 C_{\text{Ge}}^0$  is flux of germanium atoms at the orifice

Therefore, in the absence of any back diffusion, the orifice velocity of germanium atoms is,

$$v_{Ge}^o = \frac{\bar{C}_{Ge}^o - C_{Ge}^o}{C_{Ge}^o} (L/t) \quad \text{Eq. 7.16}$$

$\frac{\bar{C}_{Ge}^o(t) - C_{Ge}^o}{C_{Ge}^o}$  is the fractional concentration change of germanium atoms averaged over the capillary. All parameters in the right side of Eq. 7.16 are measurable and used to evaluate the orifice velocity.

The atomic velocity is taken to be proportional to the applied field; Eq. 7.9. The atomic mobility in an electric field in the reservoir alloy,  $U_{Ge}^o$ , is defined by:

$$U_{Ge}^o = \frac{v_{Ge}^o}{E} = \left( \frac{L}{kT} \right) Z^* \quad \text{Eq. 7.17}$$

and is experimentally determined from  $v_{Ge}^o$  and the applied field  $E$ . Usually, it is more convenient to express  $E$  as  $J \sigma$  where  $J$  is current density and  $\sigma$  is the conductivity of the liquid alloy.

#### Case B - Evaluation of $D_{eff}$ and $Z^*$

After a sufficient length of time, a steady state should exist in the capillaries, and all concentrations become independent of time. In this case, the flux equation provides,

$$v_{Ge}(x) C_{Ge}(x) = D_{eff} \frac{dC_{Ge}(x)}{dx} \quad \text{Eq. 7.18}$$

and if  $v_{Ge}(x) = v_{Ge}(0)$ , i.e.  $v_{Ge}$  is independent of concentration, we can integrate to get:

$$D_{eff} = v_{Ge}^0 x / \ln(C_{Ge}(x)/C_{Ge}^0) \quad \text{Eq. 7.19}$$

All parameters on the right are measurable. The effective charge,  $Z^*$ , can be obtained only from Eq. 7.9 under the assumption that  $D = D_{eff}$ ,

$$Z^* = \frac{v_{Ge}^0}{E} \left( \frac{kT}{D} \right) = U_{Ge}^0 \left( \frac{kT}{D} \right) \quad \text{Eq. 7.20}$$

If Eq. 7.9 is inserted into Eq. 7.18, the concentration change from orifice to electrode at saturation is proportional to the interelectrode potential; i.e.

$$\ln \left( \frac{C(x)}{C_{Ge}^0} \right) = \frac{Z^* v(x)}{kT} \quad \text{Eq. 7.21}$$

where  $v$  is the potential at  $x$  relative to zero volts at the orifice. This assumes that  $D$  is independent of concentration.

#### 7.2.4 Experimental Results

A series of capillary electromigration experiments was performed using a reservoir temperature of  $525 \pm 25^\circ \text{C}$ . Capillary lengths were of 1 to 3 cm, experiment times varied

between 30 minutes and 96 hours at current densities of 600, to  $1800 \text{ A/cm}^2$ . At higher current densities, Joule heating of the capillaries raised the local temperature by an estimated  $25 - 50^\circ \text{ C}$ . The electric field was calculated from  $E = J/\sigma$  where  $J$  is current density and  $\sigma$  is the conductivity.  $\sigma$  was measured to be  $(1.75 \pm 0.1) \times 10^3 (\Omega\text{-cm})^{-1}$ , at  $550^\circ \text{ C}$ .

After each experiment, the positive, negative and neutral capillaries were sliced into a number of cylindrical sections. Each section was irradiated in a neutron flux and the ratio of Ge atoms to Te atoms,  $\alpha = \# \text{Ge}/\# \text{Te}$ , was determined by gamma counting on a multichannel analyzer. The atomic concentrations in each section were calculated from Eq. 7.4.

In general, the data scatter was due to compositional scatter in the sections as multiple counting of the same sections provided nearly identical results. Optical microscopy of polished sections of several capillaries after electromigration revealed a coarse crystallite grain size, suggesting that crystallization of Te and GeTe following removal of the capillaries from the reservoir may have caused local dehomogenization of the alloy trapped in the capillaries.

For short experiment times,  $\frac{\bar{C}_{Ge} - C_{Ge}^0}{C_{Ge}^0}$ , the fractional change in Ge, should be proportional to  $t/L$ , for fixed  $J$ .

Moreover, the proportionality constant is the velocity,

$v_{Ge}^0$  at the orifice, in Eq. 7.16. Data points for  $t/L \leq 1.0$  hrs/cm are plotted in Fig. 7.5 as the circles. The plus or minus in the circle indicates which capillary is represented. The squares are averages of the points at each  $t/L$  for  $J = 635 \text{ A/cm}^2$ . It can be seen that in spite of large fluctuations among the individual points, good proportionality of the average is observed. The measured orifice velocity of Ge atoms with a current density of  $635 \text{ A/cm}^2$  and a temperature of  $550^\circ \text{ C}$  is  $0.23 \text{ cm/hr.}$

The orifice velocity  $v_{Ge}^0$  has been measured for three current densities and the average values obtained are plotted in Fig. 7.6. The three values lie on a straight line which intersects the origin. Thus, the diffusivity-effective charge product is not changing with current density up to  $1800 \text{ A/cm}^2$  because  $v_{Ge}^0/J$  is proportional to  $DZ^*$ . At  $550^\circ \text{ C}$ , the atomic mobility in an electric field is calculated from  $v_{Ge}^0 \sigma/J$  to be  $U_{Ge}^0 = 2.0 \times 10^{-4} \text{ cm}^2/\text{v sec}$  taking  $\sigma$  as  $1.75 \times 10^3 (\Omega\text{-cm})^{-1}$ .

Evaluation of the diffusivity  $D$  and effective charge  $Z^*$  requires experimental data at a diffusion limited saturation.

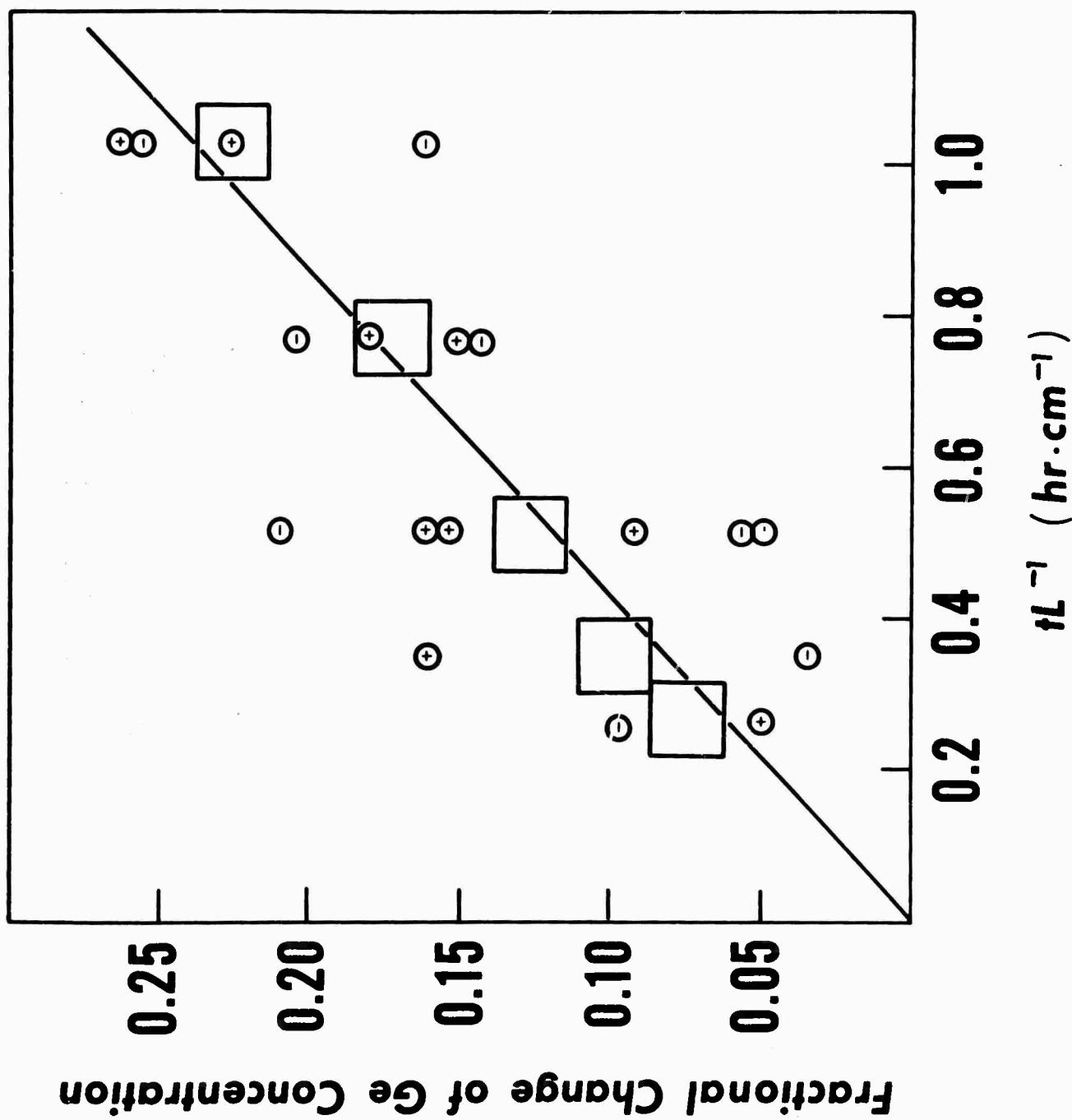


Fig. 7.5

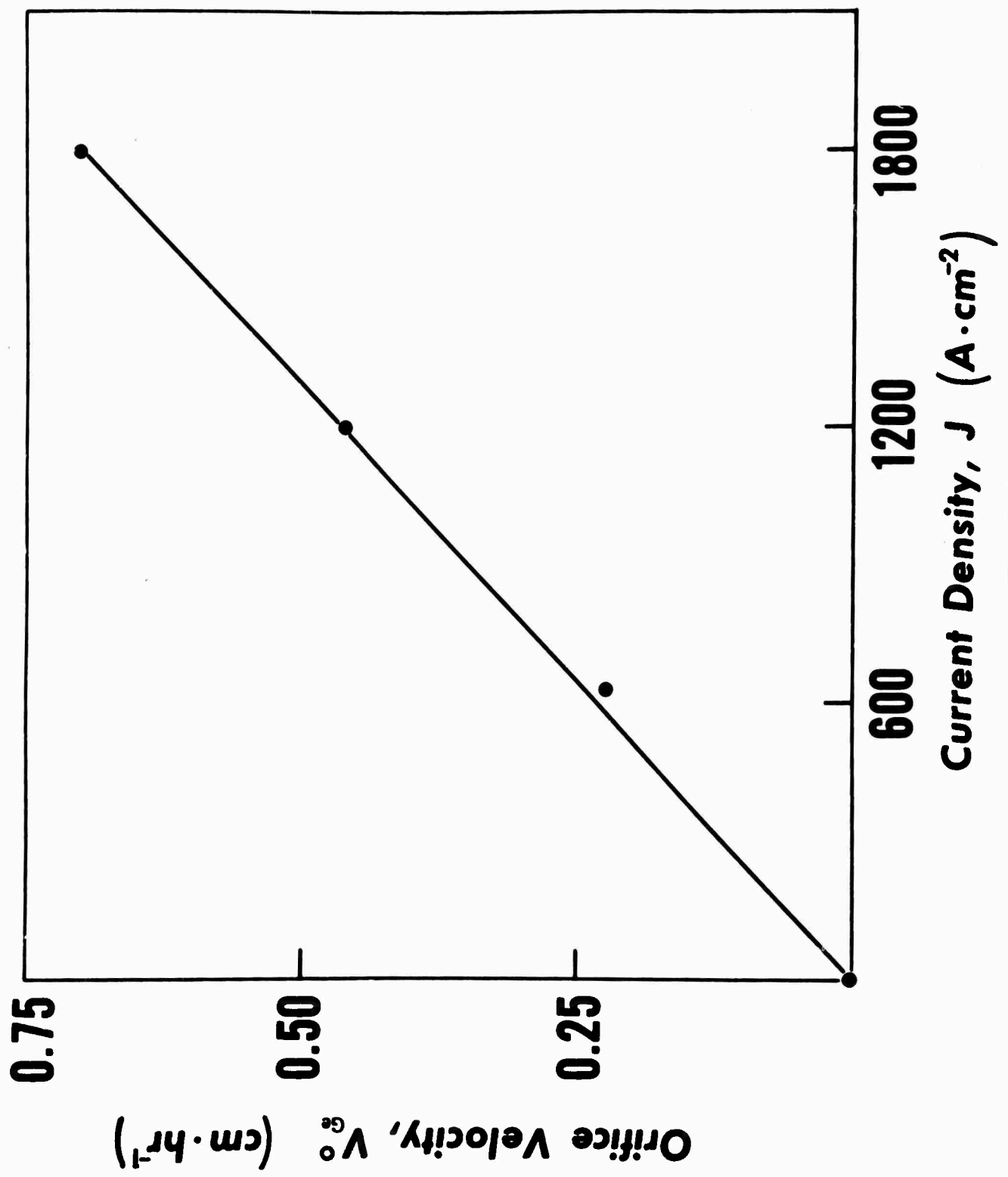


Fig. 7.6

A typical set of capillaries obtained at different experiment times were sectioned and analyzed. The data is plotted in Fig. 7.7 where the vertical axis is the atomic concentration and the horizontal axis is the position in the capillaries. Three sets of capillaries are shown; one at 48 hours duration, 2 hours, and 30 min. The temperature was  $550^{\circ}\text{C}$  and  $J$  was  $635 \text{ A/cm}^2$ .

#### A. Positive Capillary

It can be seen that the positive capillary has reached saturation in 2 hours since the profile at 2 hours is, within experimental error, the same as the profile for the 48 hour sample. Moreover, for the positive capillary  $\ln[C_{\text{Ge}}]$  plots linearly with  $x$ . Eq. 7.21 predicts linearity under the assumption of a diffusion constant and the electrical conductivity independent of concentration.

Since  $\ln C_{\text{Ge}}$  has been shown to be linear with  $x$  in the positive capillary we may calculate the diffusion constant which establishes equilibrium with the electromigration flux. From Eq. 7.19

$$D_{\text{eff}} = \frac{v_{\text{Ge}}^0 C_{\text{Ge}}^0}{d C_{\text{Ge}}^0 / dx} \quad \text{Eq. 7.22}$$

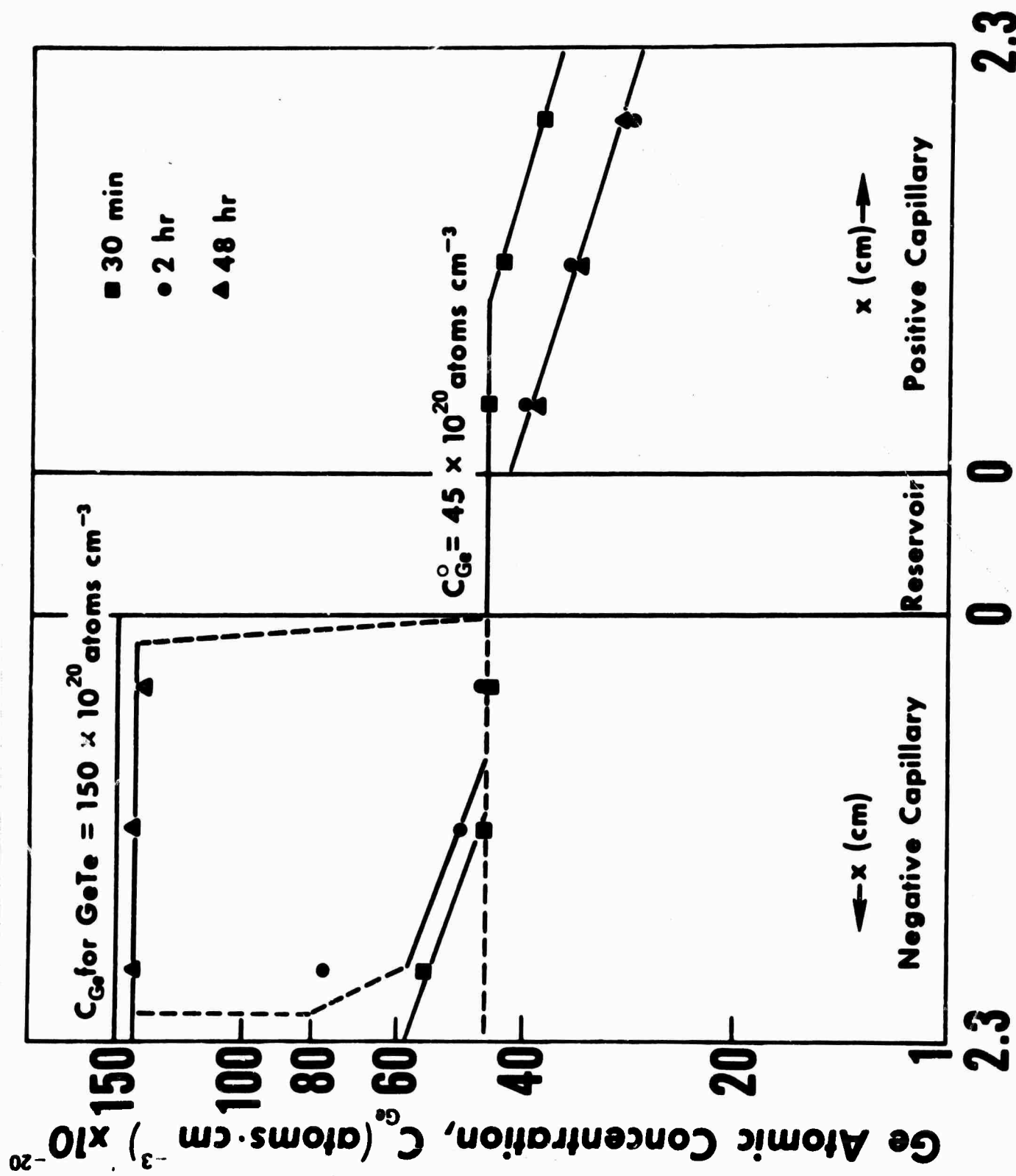


Fig. 7.7

$\frac{dC_{Ge}}{C_{Ge} dx}$  is equal to the reciprocal of the distance  $dx$  required to change  $C_{Ge}$  by a factor of 2.7.  $D_{eff}$  is calculated to be equal to  $10^{-4} \text{ cm}^2/\text{sec}$ . This effective diffusion constant is that of Ge in  $Ge_{15}Te_{85}$ , and is suggested to be only slowly varying as Ge is depleted to an alloy of  $Ge_7Te_{93}$ , since  $\ln(C_{Ge})$  vs  $x$  is linear to that composition at saturation.

The effective charge may be calculated from Eq. 7.20, if we assume that  $D_{eff} = D$ , i.e. that the eddy current mixing effects are negligible.

$$Z^* = U_{Ge}^0 \left( \frac{kT}{D} \right) \quad \text{Eq. 7.23}$$

Since  $kT \sim .052 \text{ eV}$ ,  $U_{Ge}^0 = 2 \times 10^{-4} \text{ cm}^2/\text{v sec}$  and  $D = 3.3 \times 10^{-4} \text{ cm}^2/\text{sec}$ ,  $Z^*$  is 0.03 electron charge.

However if, say,  $D_{eff} = 1. D$ , then  $Z^*$  becomes 0.3 electron charge.

Calculation of the diffusion constant  $D_{eff}$  allows an estimation of the time required for the concentration gradient to reach the orifice. Using the Klemm criterion Eq. 7.13,  $\tau_{sat} = \frac{L^2}{\pi D_{eff}}$ . Since the capillaries in Fig. 7.7 are 2.3 cm long;  $\tau_{sat} = 1.4 \text{ hours}$ .

From the data in Figure 7.7, the diffusion gradient

in the positive capillary is seen to extend approximately 1.3 cm from the electrode for a time duration of 30 minutes. Since the position of the gradient is proportional to square root time, the experimental  $\tau_{\text{sat}}$  is 1.4 hours in good agreement with the Klemm Criterion.

#### B. Negative Capillary

The negative capillaries in Fig. 7 accumulate germanium at the negative electrode to a much greater saturation level than is expected from a diffusion limit. The atomic composition of the saturated negative electrode is about 45% Ge. This high level of Ge can be accounted for by the precipitation of crystalline GeTe. At a temperature of 550° C, the GeTe liquidus boundary is reached at a composition of approximately 70% Te, 30% Ge. As the composition at the negative electrode reaches this value, the compound GeTe is formed in the alloy thus fixing the maximum concentration of Ge in the liquid at ~ 30%, i.e.  $C_{\text{Ge}}^{\text{max}} \approx 8 \times 10^{21} \text{ atoms cm}^{-3}$ . As the experiment is continued from this point, additional Ge is precipitated as GeTe grows from the negative electrode toward the orifice.

If an infinite sink for Ge exists in the negative capillary in the form of crystalline GeTe, preventing

back diffusion at the orifice, the velocity of GeTe growth may be calculated from Eq. 7.16. In this case,  $v_{Ge}^o$  is constant, and  $C_{Ge}$  will go to  $150 \times 10^{20}$  at/cm<sup>3</sup>, the germanium atomic density in crystalline GeTe.

The velocity of growth is

$$v = v_{Ge}^o \frac{C_{Ge}^o}{C_{Ge} - C_{Ge}^o} = 0.1 \text{ cm/h, for}$$

$$J = 635 \text{ A/cm}^2$$

The 2 cm capillary is calculated to be solid GeTe in 20 hours. This estimate is very close to an experimental negative capillary saturation time of 22 hours for 2 cm and 10 hours for 1 cm which consists of nearly solid GeTe. Thus, the negative capillary appears to act effectively as an infinite sink for Ge atoms until it has completely crystallized as GeTe.

#### 7.2.5 Discussion

The continued growth of GeTe approaching the orifice is not understood. Growth would be expected to terminate when the gradient of  $C_{Ge}(x)$  from the GeTe interface to the orifice reaches its steady state diffusion limited value. This would imply that for the 48 hour experiment in Fig. 7.7, the growth of GeTe should be limited at less than 1/4 of the

capillary length from the electrode. In general, however, the saturation limit of Ge in the negative capillary corresponded to nearly pure crystalline GeTe. No evidence exists to suggest that a sharp decrease in  $D$  would be expected for the high Ge alloys. If effective diffusivity,  $D_{eff}$ , were about 10 times larger than the true atomic diffusion constant in a nonturbulent alloy, then a far steeper  $C_{Ge}(x)$  gradient could exist near the GeTe liquid boundary if turbulence effects were negligible in this region. A rough interface, involving cellular or dendritic growth might be expected for the GeTe crystallization, which interface might tend to damp out turbulent flow. The dotted values of  $C_{Ge}(x)$  in the negative capillary for the two hour run in Fig. 7.7 is drawn with a break in slope near the GeTe-liquid interface to emphasize this possibility, although there are not sufficient data to resolve this issue at present.

The large values of  $D_{eff}$  for Ge in liquid  $Ge_{15}Te_{85}$  alloy seem to be about 10X reasonable values for solute diffusion in liquid metal alloys,<sup>28</sup> so that we are inclined to accept the interpretation that eddy-current turbulent mixing of the liquid in the capillaries played an important role in determining the back-diffusion gradient. However, the atomic mobility of Ge in liquid  $Te_{85}Ge_{15}$  at 550° C in an

electric field,  $U_{Ge}^0 = 2 \times 10^{-4} \text{ cm}^2 \text{ v}^{-1} \text{ sec}^{-1}$ , appears to be a reliable value which can be used to set limits on high temperature device design. At lower temperatures,  $Z^*$  and  $D$  would both be expected to shift considerably in response to increasing viscosity and covalency. Unfortunately, this alloy cannot be cooled below its liquidus temperature of  $\sim 375^\circ \text{ C}$  without encountering massive crystallization. We hope to continue these experiments on alloys which are stable against crystallization throughout their range of fluidity in order to eliminate the turbulence effects and thus to evaluate  $D$  and  $Z^*$  independently as a function of temperature.

## 6. REFERENCES

1. R. Mozzi and B. E. Warren, *J. Appl. Cryst.* 2, 164 (1969).
2. E. Lorch, *J. Phys. (C)* 2, 229 (1969).
3. E. F. Riebling, *J. Amer. Ceram. Soc.* 51, 406 (1968).
4. D. E. Polk, *J. Non-Cryst. Solids* 5, 365 (1971).
5. M. L. Theye, *Mat. Res. Bull.* 6, 103 (1971).
6. E. A. Fagen and H. Fritzsche, *J. Non-Cryst. Solids* 2, 170 (1970).
7. H. K. Rockstad, unpublished.
8. K. Weiser and M. H. Brodsky, *Phys. Rev. B1*, 791 (1970).
9. N. K. Hindley, *J. Non-Cryst. Solids* 5, 17 (1970).
10. G. Getov, B. Candilarov, P. Simidchieva, and R. Andreichin, *Phys. Stat. Solids* 13, K97 (1966).
11. E. A. Fagen, S. H. Holmberg, R. W. Seguin, and J. C. Thompson, *Proceedings of the Tenth International Conference on the Physics of Semiconductors*, Cambridge, 1970 (USAEC, Oak Ridge, 1970) p. 672.
12. H. K. Rockstad, unpublished.
13. R. Bowers, J. E. Bauerle and A. J. Cornish, *J. Appl. Phys.* 30, 1050 (1959).
14. R. H. Willens, *J. Appl. Phys.* 33, 3269 (1962).
15. J. P. deNeufville, *First Semi-Annual Technical Report on ARPA Contract No. DAHC15-70-C-0187*, December, 1970.

16. J. C. Perron, *Adv. in Phys.* 16, 657 (1967); J. T. Edmond, *Brit. J. Appl. Phys.* 17, 979 (1966).
17. H. Krebs and P. Fisher, *Trans. of the Faraday Society* (in press).
18. F. Betts, A. Bienenstock and S. R. Ovshinsky, *J. Non-Cryst. Solids* 4, 554 (1970); A. Bienenstock, F. Betts and S. R. Ovshinsky, *J. Non-Cryst. Solids* 2, 347 (1970).
19. H. Krebs, V. B. Lazarev and L. Winkler, *Z. Anerg. Allg. Chem.* 352, 277 (1967); R. A. Logan and W. L. Bond, *J. Appl. Phys.* 30, 322 (1959).
20. V. M. Glazov, S. N. Chizhevskaya, and N. N. Glagoleva, Liquid Semiconductors, Plenum Press (1969).
21. J. P. deNeufville, *Trans. of the Faraday Society* (in press).
22. M. Gerardin, *C. R. Acad. Sci. (France)* 53, 727 (1861).
23. P. C. Manglesdorf, Jr., *J. Chem. Phys.* 33, 1151-61 (1960).
24. S. G. Epstein and A. Paskin, *Phys. Lett.* 24A, 309 (1967).
25. S. G. Epstein, *Trans. Mett. Soc. AIME* 236, 1123-28 (1966).
26. J. D. Verhoeven and E. P. Hucke, *Am. Soc. Metals, Trans. Quart.* 55, 1113 (1962).
27. A. Klemm, *Z. Naturforsch* 1, 252-57 (1946).
28. N. Nachtrieb, in Liquid Metals and Solidification, Amer. Soc. for Metals, Cleveland (1958).
29. American Institute of Physics Handbook, McGraw-Hill, New York, 1957, p. 4-76.

## 9. CONTRIBUTORS TO THIS PROGRAM

Scientists

John P. deNeufville

Edgar J. Evans

Edward A. Fagen

- Julius Feinleib

\* Sato Iwasa

Simon C. Moss

Howard K. Rockstad

Robert F. Shaw

+ Om P. Sinha

Technicians

Richard Flasck

Patrick K. Flynn

+ Paul Goodwin

Robert Goss

Scott Holmberg

Donald Sarrach

Richard Seguin

Ralph Shaw

+ Wallace K. Tsuha

++ John Tyler

---

- Terminated July 7, 1971. Currently employed in the Physics Department of ITEK, Lexington, Massachusetts
- \* Terminated August 13, 1971. Currently employed in the Physics Department of ITEK, Lexington, Massachusetts.
- + Terminated April 2, 1971.
- ++ Employment became effective March 22, 1971.